

Ecole Centrale de Nantes

Warsaw University of Technology

## Master Erasmus Mundus

EMARO “EUROPEAN MASTER ON ADVANCED ROBOTICS”

2010/2011

### Final Master Thesis Report

Presented by:

CORNELIUS JOHANNES BARNARD

On 19/07/2011

TITLE

## Optimal Trajectory Generation for a High Speed Parallel Robot

### Jury

**Evaluators:** Sébastien Briot  
Stéphane Caro  
Wisama Khalil  
Ina Taralova  
Damien Chablat  
Janusz Fraczek

Researcher, IRCCyN, CNRS  
Researcher, IRCCyN, CNRS  
University Professor at ECN  
Researcher, IRCCyN, CNRS  
Researcher, IRCCyN, CNRS  
Professor, Warsaw University of Technology

Supervisor(s):

Sébastien Briot and Stéphane Caro

Laboratory: Institut de Recherche en Communications et Cybernétique de Nantes





# Contents

Title . . . . .	0
<b>List of Figures</b>	<b>iii</b>
<b>List of Tables</b>	<b>v</b>
<b>1 Introduction</b>	<b>1</b>
1.1 Parallel Robots . . . . .	3
1.2 IRSBot2 . . . . .	4
<b>2 Modeling</b>	<b>7</b>
2.1 Elastodynamic Modeling . . . . .	7
2.1.1 Lagrangian Formulation . . . . .	7
2.1.2 Elastodynamic Modeling . . . . .	8
2.1.3 Chosen Formulation: Assumed Modes . . . . .	9
2.1.4 Inertia Matrix . . . . .	11
2.1.5 Stiffness Matrix . . . . .	12
2.1.6 Equations of Motion . . . . .	13
2.1.7 Closed Form Dynamic Models . . . . .	16
2.1.8 Direct Dynamic Model . . . . .	18
2.1.9 Inverse Dynamic Model . . . . .	19
2.1.10 Five Bar Mechanism Model . . . . .	20
2.2 Geometric and Kinematic Modeling . . . . .	21
2.2.1 Rigid Inverse Geometric Model . . . . .	21
2.2.2 Elastic Inverse Geometric Model . . . . .	23
2.2.3 Rigid Kinematic Model . . . . .	26
2.2.4 Elastic Kinematic Model . . . . .	28
2.3 Model Verification . . . . .	32
2.3.1 Modified Inertia Matrix . . . . .	32
2.3.2 Frequency Analysis . . . . .	33
2.3.3 Deformation Analysis . . . . .	38
<b>3 Trajectory Design</b>	<b>40</b>
3.1 Geometric Path . . . . .	41
3.1.1 Clothoids . . . . .	41
3.1.2 Lamé Curves . . . . .	44
3.1.3 Polar Polynomials . . . . .	44
3.1.4 Geometric Path Discussion . . . . .	45
3.2 Motion Profiles . . . . .	46
3.2.1 Seventh Degree Polynomial . . . . .	46
3.2.2 Trapezoidal Profile . . . . .	47
3.2.3 Bang-bang Profile . . . . .	48



---

3.3	Trajectory Characteristics . . . . .	49
<b>4</b>	<b>Simulation</b>	<b>55</b>
4.1	Simulation Set 1 . . . . .	56
4.1.1	Vibrational Domain . . . . .	56
4.1.2	Simulation Results . . . . .	56
4.2	Simulation Set 2 . . . . .	62
4.2.1	Vibrational Domain . . . . .	62
4.2.2	Simulation Results . . . . .	63
4.3	Simulation Set 3 . . . . .	68
4.4	Simulation Set 4 . . . . .	70
<b>5</b>	<b>Conclusion</b>	<b>72</b>
	<b>Bibliography</b>	<b>74</b>

# List of Figures

1.1	Pick-and-place operation for the packaging of healthcare products . . . . .	3
1.2	Contemporary parallel robots . . . . .	4
1.3	<i>Schematic of IRSBot2 leg</i> . . . . .	5
1.4	Planar five bar mechanism . . . . .	6
2.1	Generalized coordinates for each beam, $\mathbf{q}_e = [\mathbf{q}_{e_x} \quad \mathbf{q}_{e_y}]^T$ . . . . .	8
2.2	Mode shapes in bending and tension-compression . . . . .	10
2.3	Schematic of the simulated system . . . . .	20
2.4	Rigid Geometric Model . . . . .	22
2.5	Superposition of rigid and elastic motions for clamped-free boundary conditions .	23
2.6	Elastic Geometric Model . . . . .	24
2.7	Elastic geometric model for leg $i$ . . . . .	28
2.8	Configurations for natural frequency verification . . . . .	33
2.9	The first three modes shapes as per CASTEM at position $[0.35, 0.3]$ . . . . .	33
2.10	Contour plot of first natural frequency in workspace . . . . .	35
2.11	Contour plot of second natural frequency in workspace . . . . .	35
2.12	Contour plot of third natural frequency in workspace . . . . .	36
2.13	First natural frequency in workspace as a function of tool mass . . . . .	37
2.14	Configurations for deformation verification . . . . .	38
3.1	Pick-and-place trajectory. . . . .	40
3.2	Adept half cycle using a Lamé curve . . . . .	41
3.3	Symmetric blending ray diagram . . . . .	42
3.4	Un-symmetric blending ray diagram . . . . .	43
3.5	Blending sections for the adept cycle . . . . .	45
3.6	Extended clothoid and Lamé curve generated for $e = 44.5mm$ . . . . .	46
3.7	Motion profiles generated for $t_f = 1$ . . . . .	48
3.8	Lamé curve trajectories . . . . .	50
3.9	Clothoid pair trajectories . . . . .	50
3.10	Polar polynomial trajectories . . . . .	50
3.11	Lame curve joint space trajectory and spectral content . . . . .	51
3.12	Clothoid pair joint space trajectory and spectral content . . . . .	52
3.13	Polar polynomial joint space trajectory and spectral content . . . . .	52
3.14	Spectral content for the various geometric paths . . . . .	53
3.15	Trajectory spectral content for various cycle times . . . . .	53
3.16	Trajectory spectral content for various blending lengths . . . . .	54
4.1	Position of the trajectory in the workspace (gravity is taken upwards) . . . . .	55
4.2	Frequency distribution along Adept Cycle with a 100g payload. Line styles: - Lamé, - - Clothoid, ... Polar . . . . .	56
4.3	Simulation results for a 100g payload in the task space . . . . .	57

4.4	Joint torques for a 100g payload. Line styles: - Lamé, - - Clothoid, ... Polar . . .	58
4.5	Elastic Coordinates in Bending for a 100g payload. Line styles: - Lamé, - - Clothoid, ... Polar . . . . .	58
4.6	Elastic Coordinates in Tension-Compression for a 100g payload. Line styles: - Lamé, - - Clothoid, ... Polar . . . . .	59
4.7	Spectral Distribution for a 100g payload. Line styles: - Lamé, - - Clothoid, ... Polar	59
4.8	Error norm in the task space with a 100g payload. Line styles: - Lamé, - - Clothoid, ... Polar . . . . .	61
4.9	Frequency distribution along Adept Cycle with a 6000g payload. Line styles: - Lamé, - - Clothoid, ... Polar . . . . .	62
4.10	Simulation results for a 6kg payload in the task space . . . . .	63
4.11	Joint torques for a 6000g payload. Line styles: - Lamé, - - Clothoid, ... Polar . .	64
4.12	Elastic Coordinates in Bending for with a 6kg payload. Line styles: - Lamé, - - Clothoid, ... Polar . . . . .	65
4.13	Elastic Coordinates in Tension-Compression for a 6000g payload. Line styles: - Lamé, - - Clothoid, ... Polar . . . . .	65
4.14	Spectral Distribution for a 6kg payload. Line styles: - Lamé, - - Clothoid, ... Polar	66
4.15	Error norm in the task space with a 6kg payload. Line styles: - Lamé, - - Clothoid, ... Polar . . . . .	67
4.16	Task space position for a payload of 6kg and $t_f = 0.215ms$ Line styles: - Lamé, - - Clothoid, ... Polar . . . . .	68
4.17	Task space velocity and acceleration for a payload of 6kg and $t_f = 0.215s$ Line styles: - Lamé, - - Clothoid, ... Polar . . . . .	68
4.18	Varying blending lengths for a 6000g payload. Line styles: - Lamé, - - Clothoid, ... Polar . . . . .	70

# List of Tables

2.1	Modal parameters for bending deformation . . . . .	10
2.2	Parameters of the modeled five bar mechanism . . . . .	20
2.3	Natural Frequencies at Various Robot Configurations . . . . .	34
2.4	Third natural frequency with adjusted inertia in the FEA . . . . .	34
2.5	Deformation under $F_x = 100N$ . . . . .	39
2.6	Deformation under $F_y = 100N$ . . . . .	39
3.1	Blending lengths for geometric paths . . . . .	45
3.2	Boundary conditions for the 7 <sup>th</sup> degree polynomial . . . . .	46
3.3	Tested motion profiles and geometric paths . . . . .	49
3.4	Task space velocity and acceleration comparison of generated trajectories . . . . .	49
3.5	Characteristic features of joint space trajectories . . . . .	51
4.1	Adept cycle times and payloads . . . . .	55
4.2	Terminal end-effector state at $t_f = 0.3$ for a payload of 100g . . . . .	57
4.3	Maximum task space velocity and acceleration for a payload of 100g and a cycle time of $t_f = 0.3s$ . . . . .	57
4.4	Task space velocity and acceleration comparison of generated trajectories . . . . .	60
4.5	Residual norms at end effector end points . . . . .	62
4.6	Averaged terminal end-effector state at $t_f = 0.43$ for a payload of 6000g . . . . .	63
4.7	Maximum task space velocity and acceleration for a payload of 6kg and a cycle time of $t_f = 0.43$ . . . . .	63
4.8	Task space velocity and acceleration comparison of generated trajectories . . . . .	66
4.9	Residual error norms at end effector end points for a payload of 6kg . . . . .	67
4.10	Comparison of results for a cycle time of $t_f = 0.215s$ . . . . .	69
4.11	Residual error norms at end effector end points for a payload of 6kg . . . . .	69
4.12	Comparison of short and extended cycle lengths . . . . .	71
4.13	Comparison of error norms on short and extended cycle lengths . . . . .	71

# Chapter 1

## Introduction

The advantages of parallel robots over serial robots for high speed applications is a subject which is drawing much attention of late. Currently parallel robots are finding more and more acceptance in high-speed pick-and-place operations. Parallel robots significantly improve the throughput of many robotic tasks [3, 21]. The drive for higher operational speeds and higher payload-to-weight ratios is shifting the design of manipulators to more lightweight structures [25].

In contrast to serial manipulators, parallel robots offer a lower mass-to-inertia ratio and a higher stiffness-to-mass ratio<sup>1</sup> [20]. These benefits come at the price of increased modeling and design complexity. The design of parallel robots is accompanied with several closed kinematic chains with inherent kinematic constraints.

As for all high-speed mechanisms, vibratory phenomena appear that deteriorate the robot accuracy and its dynamic performance. The performance criteria on speed and accuracy have rendered classical rigid body dynamics for the description of the dynamic behaviour of such systems inadequate [22]. Due to the inherent flexibility of these lightweight structures, inertial forces result in unwanted structural vibration [28]. These vibrations deteriorate not only the accuracy and performance of the manipulator but also cause significant wear and tear on the components [15].

---

<sup>1</sup>Structural Rigidity

## Problem Statement

The IRCCyN<sup>2</sup> robotics team has recently proposed a new high speed parallel manipulator, IRSBot2, with two degrees of freedom. Investigate the use of an optimal motion generator for the reduction of vibrations in IRSBot2 by carefully planning the displacements of the end effector. The optimality of this motion generator is concerned with the level of vibration reduction and the speed at which the pick-and-place operation is conducted. The scope of this thesis is as follows:

- Development of an elastodynamic model of the IRSBot2
- Design of a motion generator:
  - The definition of the geometric path as based on the Adept Cycle
  - The definition of the motion profile or temporal control law
- Spectral analysis of the control law and manipulator response to verify that the natural modes of vibration are not excited

This bibliographic report consolidated recent work done in vibration reduction, thereby providing a thorough foundation from which vibration in parallel manipulators can be managed in particular for pick-and-place tasks common in industry today.

In accordance with the literature studied, this bibliographic work was divided into three chapters concerning:

1. Elastodynamic Modeling
2. Trajectory Design
3. Control

The thesis work limits the scope of the material identified in the bibliographic report and in this masters dissertation, the work is divided as follows:

1. Geometric and Kinematic Modeling
2. Elastodynamic Modeling
3. Trajectory Design
4. Simulation

---

<sup>2</sup>Institut de Recherches en Communications et Cybernétique de Nantes

## 1.1 Parallel Robots

Before expanding on the above mentioned areas, a brief introduction to parallel robots is provided. Particularities relevant to this work are highlighted. The master thesis of Germain [10] provides a comprehensive overview of parallel robots used for pick-and-place tasks in industry today.

Pick-and-place operations comprise both primary handling and case packing (see figure 1.1)[18]. These operations usually require between 2 and 4 degrees of freedom (DOF) - typically two or three translational degrees of freedom and if required, one rotational degree of freedom [10, 11, 9].

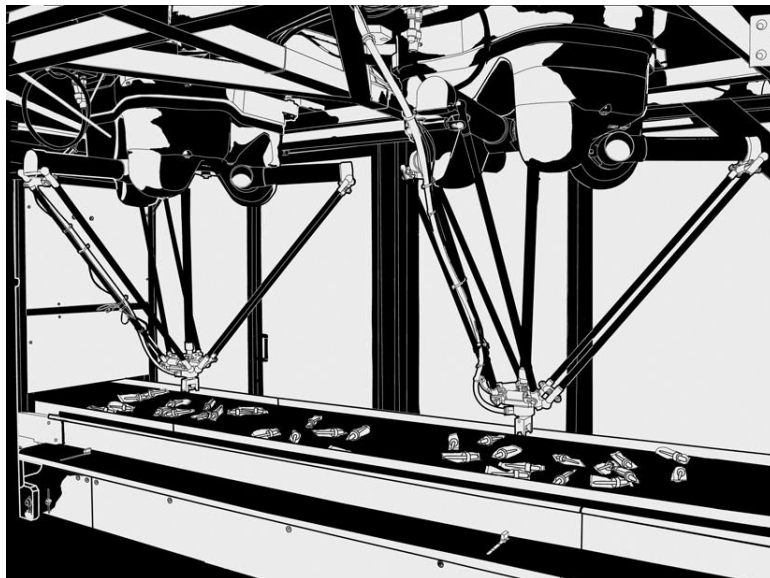


Figure 1.1: *Pick-and-place operation for the packaging of healthcare products [19].*

Several four degree of freedom parallel robots exist on the market today. Robots with 3 translational degrees of freedom and one rotational degree of freedom about the  $z$ -axis are capable of performing Schönflies motions. Adept Technology [13] currently have the fastest pick-and-place robot, the Quattro (number 1 in figure 1.2) in production. The Quattro is capable of performing up to 240 cycles per minute<sup>3</sup>. Figure 1.2 also shows the *Flex-picker* delta robot from ABB (2) and the McGill SMG robot (3).

For tasks requiring two degrees of freedom (DOF), such as the one considered for this thesis, simpler robots may be used [10]. Two degree of freedom robots are considered as planar robots and are used to position a point in the plane of operation. The Par2 (number 4 in figure 1.2) developed in the ANR<sup>4</sup> *100g Objective* project and the Elau PacDrive D2 (5) [7] are examples of 2DOF designs.

A key design requirement for these robots is to ensure structural rigidity perpendicular to the operation plane, thereby resisting forces normal to this plane. This requirement is for instance addressed by the second set of legs in the Par2 robot rendering it much stiffer than the PacDrive D2. Nonetheless, Germain [10] notes several drawbacks of the Par2:

<sup>3</sup>Standard cycle: 25mm/350mm/25mm

<sup>4</sup>Agence Nationale de la Recherche



### Parallel Robots

1. Quattro Robot
2. Delta Robot
3. McGill SMG
4. PacDrive D2
5. Par2

Figure 1.2: Contemporary parallel robots [10].

1. It has a complex architecture.
2. The inclusion of stiff metallic belts for the prevention of lateral motion introduces undesired elasticity.
3. High tolerance requirements for its manufacturing and construction due to the number of joints.
4. The identification of its dynamic behaviour is difficult to obtain.

## 1.2 IRSBot2

The newly conceived IRSBot2 (see figure 1.3) responds to the aforementioned drawbacks. The IRSBot2 structure is of spatial architecture and offers certain advantages [10]:

1. It consists of only two legs, thereby reducing the overall mass and improving the dynamic behaviour of the system.
2. The design is such that a number of the links, rather than being subjected to bending, are only subjected to tensile, compression and torsional forces, also improving the dynamic performance of the design.

In figure 1.4, the global coordinate frame  $O$ , attached to the fixed base, is shown in plane  $\mathcal{P}_0$  and the moving platform (always parallel to the base) is defined in plane  $\mathcal{P}_1$ . Each leg consists of two distinct parts. The upper part, composed of links  $0_i, 1_i, 2_i, 3_i$  forms a parallelogram. The lower part, of greater complexity, exists between links  $3_i$  and  $7_i$ . Note that the joint axes  $\mathbf{y}_{1ji}$  are always within plane  $\mathcal{P}_1$  which, in turn is always parallel to planes  $\mathcal{P}_0$  and  $\mathcal{P}_2$ . Furthermore note that the axes  $\mathbf{y}_{1ji}$  and  $\mathbf{z}_{2ji}$  are orthogonal. The assembly of the lower part of the leg gives rise to the spatial movement particular to IRSBot2. The geometric description of the robot will briefly be discussed. For more detail the reader is directed to Germain [10].



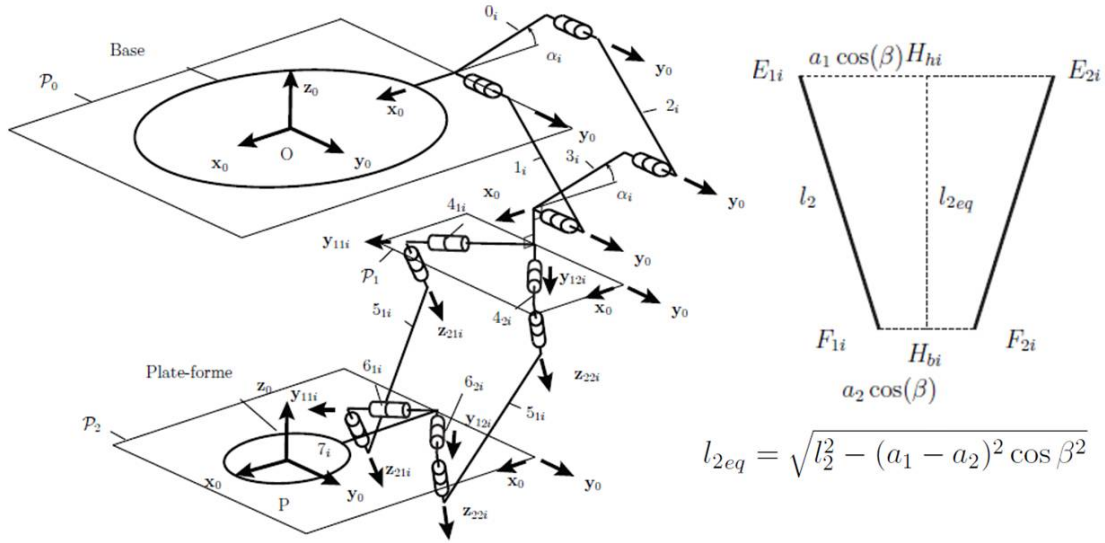


Figure 1.3: Schematic of IRSBot2 leg [10]

## Loop Closure

The loop closure equations are used to develop the inverse and geometric models. Germain [10] uses the parametrization shown in figure 1.4 with the definition of the virtual link  $l_{2eq}$  to define the loop closure equations. The  $\pm$  symbol designates + to leg 1 and - to leg 2:

$$l_{2eq}^2 = (x \pm d/2 - l_1 \cos q_i)^2 + (z + l_1 \sin q_i + e)^2$$

with  $d/2 = b - p - a_1 \sin \beta$

## Inverse Geometric Model

The inverse geometric model (IGM) gives the joint positions,  $q_1$  and  $q_2$ , as a function of the Cartesian coordinates,  $x$  and  $z$ , of the end effector. As with other parallel manipulators, the loop closure equations allow the IGM to be easily expressed. The expression of the IGM is included as is from [10]. Here  $\pm$  refers to the working modes:

$$q_1 = 2 \tan^{-1} \left( \frac{-B_1 \pm \sqrt{B_1^2 + A_1^2 - C_1^2}}{C_1 - A_1} \right) \text{ with } \begin{cases} A_1 = -2l_1(x + b - p - a_1 \sin \beta) \\ B_1 = 2l_1(z + e) \\ C_1 = (x + b - p - a_1 \sin \beta)^2 \\ \quad + (z + e)^2 + l_1^2 - l_{2eq}^2 \end{cases}$$

$\forall x, z$  such that  $B_2^2 + A_2^2 \geq C_2^2$

$$q_2 = 2 \tan^{-1} \left( \frac{-B_2 \pm \sqrt{B_2^2 + A_2^2 - C_2^2}}{C_2 - A_2} \right) \text{ with } \begin{cases} A_2 = -2l_1(x - b + p + a_1 \sin \beta) \\ B_2 = 2l_1(z + e) \\ C_2 = (x - b + p + a_1 \sin \beta)^2 \\ \quad + (z + e)^2 + l_1^2 - l_{2eq}^2 \end{cases}$$

$\forall x, z$  such that  $B_2^2 + A_2^2 \geq C_2^2$

## Direct Geometric Model

The direct geometric model (DGM) is also derived from the loop closure equations and is presented as in Germain [10]. Here  $\pm$  refers to the assembly modes of the robot:

$$x = \frac{c_2 - c_1 - 2z(a_{z1} - a_{z2})}{2(a_{x1} - a_{x2})}$$

$$z = \frac{-e \pm \sqrt{h^2 - jg}}{g} \quad \text{such that } h^2 \geq jg$$

$$\text{with } \begin{cases} j = c_1 + \frac{(c_2 - c_1)^2}{4(a_{x1} - a_{x2})^2} + \frac{a_{x1}(c_2 - c_1)}{a_{x1} - a_{x2}} \\ h = \frac{(c_2 - c_1)(a_{z1} - a_{z2})}{2(a_{x1} - a_{x2})} + \frac{a_{x1}(a_{z1} - a_{z2})}{a_{x1} - a_{x2}} \\ g = 1 + \frac{(a_{z1} - a_{z2})^2}{(a_{x1} - a_{x2})^2} \end{cases}$$

## Simplified Model

As a preliminary study, the chosen model was simplified. The simplest parallel mechanism with revolute joints resembling the IRSBot2, is a planar five bar mechanism (figure 1.4)



Figure 1.4: Planar five bar mechanism [26]

In the next chapter (Chapter 2), firstly the rigid and elastic kinematics of the planar five bar mechanism will be developed. Secondly the elastodynamic modeling is developed from first principles and lastly, the resultant model is verified.

# Chapter 2

## Modeling

### 2.1 Elastodynamic Modeling

Elastodynamic modeling can be done using either a hybrid Newton Euler approach or a Lagrangian Formulation. The Lagrangian formulation is opted for, and is developed in the next section.

#### 2.1.1 Lagrangian Formulation

The Lagrange equations are used to derive the elastodynamic model as it is readily applied to the analysis of closed loop structures. The Lagrangian formulation equates the nonconservative forces acting on the system to the change of energy in the system [1]. The Lagrangian  $L$  of a robot or manipulator is defined as the difference between the kinetic energy  $E$  and the potential energy  $U$ :

$$L = E - U \quad (2.1)$$

The formulation of the constituent terms of the Lagrangian are shown in equations 2.2 and 2.3. Development of the inertia,  $\mathbf{M}$ , and stiffness,  $\mathbf{K}$ , matrices found in the kinetic and potential energy terms vary according to the elastodynamic modeling used. For beam  $j$ :

**Kinetic Energy :**

$$E_j = \frac{1}{2} \mathbf{q}_j^T \mathbf{M}_j \mathbf{q}_j \quad (2.2)$$

where

$\mathbf{M}_j$  : is the symmetric positive definite inertia matrix of beam  $j$  <sup>1</sup>.

$\mathbf{q}_j$  : is the vector of generalized coordinates  $\mathbf{q}_j = [x_{A_j}, y_{A_j}, \theta_j, \mathbf{q}_{e_j}]^T$  (see figure 2.1).

**Potential Energy**

$$V_{e_j} = \frac{1}{2} \mathbf{q}_j^T \mathbf{K}_j \mathbf{q}_j \quad (2.3)$$

where

$\mathbf{K}_j$  : is the stiffness matrix of beam  $j$

---

<sup>1</sup>The inertia matrix is also referred to as the mass matrix

Figure 2.1: *Generalized coordinates for each beam,  $\mathbf{q}_e = [\mathbf{q}_{e_x} \quad \mathbf{q}_{e_y}]^T$*

### 2.1.2 Elastodynamic Modeling

The various elastodynamic modeling techniques used to develop the Lagrangian formulation are compared and contrasted next, with the motivation for the use of Assumed Modes is discussed in section 2.1.2.

#### Finite Element Modeling

This method represents each link as an assembly of a finite number of elements, wherein each element is a continuous member of the link [17]. Linear finite elements make use of polynomial interpolation functions (expressing nodal displacements) or assumed mode techniques to characterize a link's elastic behaviour [5, 25]. Boundary conditions, changes in geometry and physical properties can be easily accounted for with the finite element method (FEM) [25]. Greater model accuracy is used by either using more elements or by using higher order elements [21].

#### Lumped Parameter Model

Lumped parameter models or rigid finite element models [29], also referred to as the finite segment method by Shabana [24], describe manipulators as a set of interconnected rigid bodies [22]. The manipulator links are discretized into a series of rigid bodies which are then connected by linear springs thereby introducing flexible features to the model [25]. The method of lumped parameters is also referred to as the method of *Virtual Joints* or VJM [3] and is considered to be the simplest method to implement.

In its standard formulation, the method does not lend itself well to closed loop robots. Briot, Pashkevich and Chablat [3] address the problem of passive joints in closed loop robots and propose a reduced method which decreases the dimension of the problem by using assumed mode techniques. Despite its simplicity, Theodore and Ghosal [25] indicate that the method is seldom used due to the difficulty of determining the spring constants. Pashkevich, Chablat and Wenger [20] do however propose a method of determining the virtual stiffness from a finite element link stiffness evaluation.

## Assumed Modes

The assumed mode method (AMM)<sup>2</sup> describes flexible displacements by a *truncated modal series*, in terms of spatial mode eigen functions and time-varying mode amplitudes [6, 25]. The truncated modal series refers to a subgroup of trigonometric functions each depicting the physical modal behaviour of links or beams. The mode shapes can be found by solving the free vibration problem for a given set of boundary conditions.

The mode shapes are characterized by their corresponding eigen vectors and occur at a frequency given by the associated eigen values [4]. If clamped-mass boundary conditions are chosen, time-varying mode amplitudes occur as the frequency equations are time dependent<sup>3</sup>. Clamped-free boundary conditions are used for simplification purposes at the expense of overestimated natural frequencies. The AMM is modeled using the floating reference frame discussed in section 2.2.2 [28].

### 2.1.3 Chosen Formulation: Assumed Modes

Dwivedy and Eberhard [6] present an extensive review on various elastodynamic modeling approaches. The bibliographic report compared and contrasted the Assumed Modes Method, the Finite Element Method and Lumped Parameter Modeling. Based on the bibliographic survey, the Assumed Modes Method was chosen as the modeling approach. The supporting factors of this approach are [25]:

- Assumed Modes is recommended for manipulators with flexible links of uniform cross-section
- Well suited for numerical simulations

The approach calls for the superposition of elastic motions on the rigid motions in the system [22, 28]. The properties of the Assumed Modes approach are listed next:

- Flexible displacements are represented by truncated modal series [6, 25]
- Floating reference frames are introduced to superpose the flexible deformations on the rigid positions of the distal end of each link [2, 5, 21, 24]
- Beam deformations are described with appropriate shape functions

## Shape Functions

The truncated modal series used to describe the deformation of a beam are referred to as the shape functions. For the planar case, bending and tension-compression deformations are considered. The shape functions,  $\Phi$  are coupled with time varying elastic coordinates  $\mathbf{q}_e$  [6, 25]. In bending, these coordinates are perpendicular to the undeformed axial direction of the beam, whereas they are collinear with this axis in tension-compression deformation. The vector  $\Phi$  is of size  $1 \times k$ , with  $k$  being the number of modes used for modeling.

A two degree of freedom pick and place robot is typically actuated at its base. It is assumed that the actuated links are rigidly connected to these actuators, as such, these links are modeled as beams in bending [2]. For link  $j$ :

<sup>2</sup>Also called the Rayleigh-Ritz approach [3, 21]

<sup>3</sup>The clamped-mass rather than the clamped-free boundary conditions are used to include the inertial effects of other links [25]

**Clamped-free :**

$$\phi_{jk}(\xi) = \sin(\alpha_k l_j \xi) + a_k \cos(\alpha_k l_j \xi) - \sinh(\alpha_k l_j \xi) - a_k \cosh(\alpha_k l_j \xi) \quad (2.4)$$

where

$a_k$  **and**  $\alpha_k l_j$  : are modal parameters for mode  $k$  [22]

$\xi = \frac{x}{l_j}$  :  $l_j$  is length of link  $j$  and  $x$  is the position along the axial direction of the beam

The first three modal parameters are considered and are taken from Bouzgarrou et al [2]:

Mode	$a_k$	$\alpha_k l_j$
1	-1.3622	1.8751
2	-0.98186	4.6941
3	-1.0008	7.8548

Table 2.1: Modal parameters for bending deformation

The distal links are assumed to be pin-connected, and are thus only loaded in the axial direction. This loading corresponds to cases in which a beam experiences only tensile or compressive deformations:

**Pin Connected :**

$$\phi_{jk}(\xi) = \sin\left((2k-1)\frac{\pi}{2}\xi\right) \quad (2.5)$$

where

$\xi = \frac{x}{l_j}$  :  $l_j$  is length of link  $j$  and  $x$  is the position along the axial direction of the beam

The normalized shape functions are shown in figure 2.2.

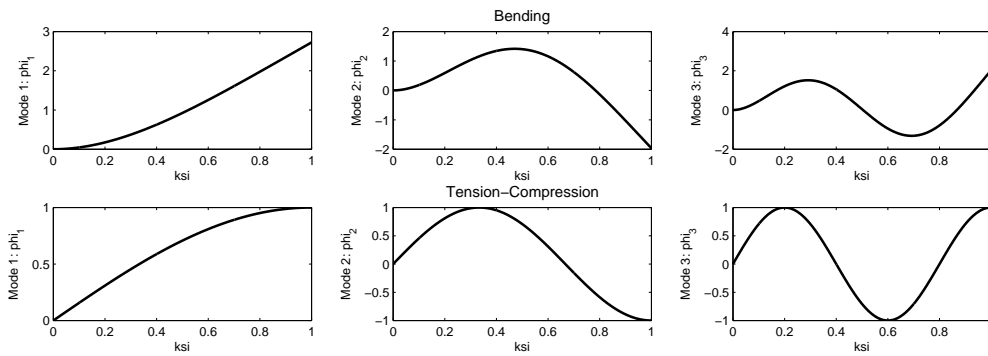


Figure 2.2: Mode shapes in bending and tension-compression

Having introduced the assumed modes method of modeling and the relevant shape functions, the inertial and stiffness matrices may now be developed.

### 2.1.4 Inertia Matrix

The inertia matrix,  $\mathbf{M}_j$ , in equation 2.2 may now be developed. The kinetic energy of a elastic beam,  $j$ , may now expressed using the shape functions [2, 22, 5]:

$$E = \frac{1}{2} \int_0^{l_j} \dot{\mathbf{r}}_{\mathbf{M}}^T \dot{\mathbf{r}}_{\mathbf{M}} dx \quad (2.6)$$

The velocity vector,  $\dot{\mathbf{r}}_{\mathbf{M}}$ , is defined according to the type of deformation modeled on the beam.  $\mathbf{r}_{\mathbf{M}}$  describes the position of a point on a deformed beam in the global reference frame as follows:

$$\mathbf{r}_{\mathbf{M}} = \begin{bmatrix} x_{A_j} \\ y_{A_j} \end{bmatrix} + \mathbf{R}(\theta_j) \begin{bmatrix} l_j \xi \\ 0 \end{bmatrix} + \mathbf{R}(\theta_j) \begin{bmatrix} u_{x_j}(\xi, t) \\ u_{y_j}(\xi, t) \end{bmatrix} \quad (2.7)$$

where

$x_{A_j}$  **and**  $y_{A_j}$  : Locate the base of link  $j$

$R(\theta_j)$  : A rotation matrix which orientates the beam at an angle  $\theta_j$

$u_{x_j}(\xi, t)$  **and**  $u_{y_j}(\xi, t)$  : Are the deformations on the beam evaluated at position  $\xi$  at time  $t$ :

$$u_{x_j}(\xi, t) = \Phi_{\mathbf{x}}(\xi) \mathbf{q}_{\mathbf{e}_{x_j}}(t)$$

$$u_{y_j}(\xi, t) = \Phi_{\mathbf{y}}(\xi) \mathbf{q}_{\mathbf{e}_{y_j}}(t)$$

Deriving expression 2.7 with respect to time, the velocity of the point  $\mathbf{r}_{\mathbf{M}}$ , for a beam in pure bending (deformation only being allowed in  $u_{y_j}(\xi, t)$ , i.e.  $u_{x_j}(\xi, t) = 0$ ) may be found:

$$\dot{\mathbf{r}}_{\mathbf{M}} = \begin{bmatrix} 1 & 0 & -\Phi_{\mathbf{y}} \mathbf{q}_{\mathbf{e}_{y_j}} & 0 \\ 0 & 1 & l_j \xi & \Phi_{\mathbf{y}} \end{bmatrix} \begin{bmatrix} \dot{x}_{A_j} \\ \dot{y}_{A_j} \\ \dot{\theta}_j \\ \dot{\mathbf{q}}_{\mathbf{e}_{y_j}} \end{bmatrix} \quad (2.8)$$

To obtain the mass matrix for a beam in pure bending, the following calculation, contained in 2.6, must be performed:

$$\mathbf{M}_j = m_j \int_0^1 \begin{bmatrix} 1 & 0 \\ -\Phi_{\mathbf{y}} \mathbf{q}_{\mathbf{e}_{y_j}} & l_j \xi \\ 0 & \Phi_{\mathbf{y}} \end{bmatrix} \begin{bmatrix} 1 & 0 & -\Phi_{\mathbf{y}} \mathbf{q}_{\mathbf{e}_{y_j}} & 0 \\ 0 & 1 & l_j \xi & \Phi_{\mathbf{y}} \end{bmatrix} d\xi \quad (2.9)$$

This results in the following mass matrix, dimensioned according to the number of generalized coordinates:

$$\mathbf{M}_j = m_j \int_0^1 \begin{bmatrix} 1 & 0 & -\Phi_{\mathbf{y}} \mathbf{q}_{\mathbf{e}_{y_j}} & \mathbf{0} \\ 0 & 1 & l_j \xi & \Phi_{\mathbf{y}} \\ -\mathbf{q}_{\mathbf{e}_{y_j}}^T \Phi_{\mathbf{y}}^T & l_j \xi & (l_j \xi)^2 & l_j \xi \Phi_{\mathbf{y}} \\ \mathbf{0} & \Phi_{\mathbf{y}}^T & l_j \xi \Phi_{\mathbf{y}}^T & \Phi_{\mathbf{y}}^T \Phi_{\mathbf{y}} \end{bmatrix} d\xi \quad (2.10)$$

Similarly the mass matrix of a beam in tension and compression may be found. Here, deformation is only allowed in  $u_{x_j}(\xi, t)$  and so  $u_{y_j}(\xi, t) = 0$ :

$$\dot{\mathbf{r}}_{\mathbf{M}} = \begin{bmatrix} 1 & 0 & 0 & \Phi_{\mathbf{x}} \\ 0 & 1 & l_j \xi + \Phi_{\mathbf{x}} \mathbf{q}_{\mathbf{e}_{x_j}} & \mathbf{0} \end{bmatrix} \begin{bmatrix} \dot{x}_{A_j} \\ \dot{y}_{A_j} \\ \dot{\theta} \\ \dot{\mathbf{q}}_{\mathbf{e}_{x_j}} \end{bmatrix} \quad (2.11)$$

This results in the following mass matrix:

$$\mathbf{M}_j = m_j \int_0^1 \begin{bmatrix} 1 & 0 & 0 & \mathbf{\Phi}_x \\ 0 & 1 & l_j \xi + \mathbf{\Phi}_x \mathbf{q}_{e_{x_j}} & \mathbf{0} \\ 0 & l_j \xi + \mathbf{q}_{e_{x_j}}^T \mathbf{\Phi}_x^T & (l_j \xi)^2 + 2l_j \xi \mathbf{\Phi}_x \mathbf{q}_{e_{x_j}} + \mathbf{q}_{e_{x_j}}^T \mathbf{\Phi}_x^T \mathbf{\Phi}_x \mathbf{q}_{e_{x_j}} & \mathbf{0} \\ \mathbf{\Phi}_x^T & \mathbf{0} & \mathbf{0} & \mathbf{\Phi}_x^T \mathbf{\Phi}_x \end{bmatrix} d\xi \quad (2.12)$$

Beams which experience both bending and tension-compression deformation (i.e. deformation is allowed in both  $u_{x_j}(\xi, t)$  and  $u_{y_j}(\xi, t)$ ), are described as follows:

$$\dot{\mathbf{r}}_M = \begin{bmatrix} 1 & 0 & -\mathbf{\Phi}_y \mathbf{q}_{e_{y_j}} & \mathbf{\Phi}_x & \mathbf{0} \\ 0 & 1 & l_j \xi + \mathbf{\Phi}_x \mathbf{q}_{e_{x_j}} & \mathbf{0} & \mathbf{\Phi}_y \end{bmatrix} \begin{bmatrix} \dot{x}_{A_j} \\ \dot{y}_{A_j} \\ \dot{\theta}_j \\ \dot{\mathbf{q}}_{e_{x_j}} \\ \dot{\mathbf{q}}_{e_{y_j}} \end{bmatrix} \quad (2.13)$$

Resulting in the rather complicated mass matrix:

$$\mathbf{M}_j = m_j \int_0^1 \begin{bmatrix} 1 & 0 & -\mathbf{\Phi}_y \mathbf{q}_{e_{y_j}} & \mathbf{\Phi}_x & \mathbf{0} \\ 0 & 1 & l_j \xi + \mathbf{\Phi}_x \mathbf{q}_{e_{x_j}} & \mathbf{0} & \mathbf{\Phi}_y \\ -\mathbf{q}_{e_{y_j}}^T \mathbf{\Phi}_y^T & l_j \xi + \mathbf{q}_{e_{x_j}}^T \mathbf{\Phi}_x^T & \Delta & -\mathbf{q}_{e_{y_j}}^T \mathbf{\Phi}_y^T \mathbf{\Phi}_x & \Upsilon \\ \mathbf{\Phi}_x^T & \mathbf{0} & -\mathbf{\Phi}_x^T \mathbf{\Phi}_y \mathbf{q}_{e_{y_j}} & \mathbf{\Phi}_x^T \mathbf{\Phi}_x & \mathbf{0} \\ 0 & \mathbf{\Phi}_y^T & \Upsilon^T & 0 & \mathbf{\Phi}_y^T \mathbf{\Phi}_y \end{bmatrix} d\xi \quad (2.14)$$

With,

$$\Delta = (l_j \xi)^2 + \mathbf{q}_{e_{x_j}}^T \mathbf{\Phi}_x^T \mathbf{\Phi}_x \mathbf{q}_{e_{x_j}} + \mathbf{q}_{e_{y_j}}^T \mathbf{\Phi}_y^T \mathbf{\Phi}_y \mathbf{q}_{e_{y_j}} + 2l_j \xi \mathbf{\Phi}_x \mathbf{q}_{e_{x_j}} - 2\mathbf{q}_{e_{y_j}}^T \mathbf{\Phi}_y^T \mathbf{\Phi}_x \mathbf{q}_{e_{x_j}} - 2l_j \xi \mathbf{\Phi}_y \mathbf{q}_{e_{y_j}}$$

$$\Upsilon = l_j \xi \mathbf{\Phi}_y + \mathbf{q}_{e_{x_j}}^T \mathbf{\Phi}_x^T \mathbf{\Phi}_y$$

### 2.1.5 Stiffness Matrix

The stiffness matrix,  $\mathbf{K}_j$ , in equation 2.2 is necessary for the evaluation of the elastic potential energy of a elastic beam. For beams in bending [25]:

$$\mathbf{K}_{y_j} = \frac{EI_j}{l_j^3} \int_0^1 \left( \frac{\partial^2 u_y(\xi, t)}{\partial \xi^2} \right)^2 d\xi \quad (2.15)$$

Considering the first 3 modes of deformation, the stiffness matrix of a beam in pure bending is expressed as the diagonal matrix  $\mathbf{K}_y$ :

$$\mathbf{K}_{y_j} = \frac{EI_j}{l_j^3} \begin{bmatrix} \int_0^1 \left( \frac{\partial^2 \phi_{y_1}(\xi)}{\partial \xi^2} \right)^2 d\xi & 0 & 0 \\ 0 & \int_0^1 \left( \frac{\partial^2 \phi_{y_2}(\xi)}{\partial \xi^2} \right)^2 d\xi & 0 \\ 0 & 0 & \int_0^1 \left( \frac{\partial^2 \phi_{y_3}(\xi)}{\partial \xi^2} \right)^2 d\xi \end{bmatrix} \quad (2.16)$$

Similarly for beams in tension and compression:

$$\mathbf{K}_{x_j} = \frac{EA_j}{l_j} \int_0^1 \left( \frac{\partial u_x(\xi, t)}{\partial \xi} \right)^2 d\xi \quad (2.17)$$



Thus, for the first three modes:

$$\mathbf{K}_{x_j} = \frac{EA_j}{l_j} \begin{bmatrix} \int_0^1 \left( \frac{\partial \phi_{x_1}(\xi)}{\partial \xi} \right)^2 d\xi & 0 & 0 \\ 0 & \int_0^1 \left( \frac{\partial \phi_{x_2}(\xi)}{\partial \xi} \right)^2 d\xi & 0 \\ 0 & 0 & \int_0^1 \left( \frac{\partial \phi_{x_3}(\xi)}{\partial \xi} \right)^2 d\xi \end{bmatrix} \quad (2.18)$$

For beams which deform in both bending and tension-compression, the stiffness matrix  $\mathbf{K}$  is augmented diagonally<sup>4</sup>:

$$\mathbf{K}_j = \begin{bmatrix} \mathbf{K}_{x_j} & \mathbf{0} \\ \mathbf{0} & \mathbf{K}_{y_j} \end{bmatrix} \quad (2.19)$$

### 2.1.6 Equations of Motion

The dynamics of the complete system may be solved by creating the total inertia and stiffness matrices,  $\mathbf{M}_{\text{tot}}$  and  $\mathbf{K}_{\text{tot}}$ . The matrices are collected in diagonal matrices as follows:

$$\mathbf{M}_{\text{tot}} = \begin{bmatrix} \mathbf{M}_1 & \mathbf{0} & \dots & \mathbf{0} \\ \mathbf{0} & \mathbf{M}_2 & \dots & \mathbf{0} \\ \vdots & \vdots & \ddots & \vdots \\ \mathbf{0} & \mathbf{0} & \dots & \mathbf{M}_n \end{bmatrix} \quad (2.20)$$

and,

$$\mathbf{K}_{\text{tot}} = \begin{bmatrix} \mathbf{K}_{\text{tot}_1} & \mathbf{0} & \dots & \mathbf{0} \\ \mathbf{0} & \mathbf{K}_{\text{tot}_2} & \dots & \mathbf{0} \\ \vdots & \vdots & \ddots & \vdots \\ \mathbf{0} & \mathbf{0} & \dots & \mathbf{K}_{\text{tot}_n} \end{bmatrix} \quad (2.21)$$

Where,

$n$  : refers to the number of elastic beams in the system

and,

$$\mathbf{K}_{\text{tot}_j} = \begin{bmatrix} \mathbf{0}_{3 \times 3} & \mathbf{0} \\ \mathbf{0} & \mathbf{K}_j \end{bmatrix} \quad (2.22)$$

The Lagrangian formulation of the elastodynamic problem is developed from the Lagrangian defined in 2.1. For closed loop robots, the loop closure constraints are reflected in the formulation [28]:

$$\mathbf{F} = \frac{d}{dt} \left[ \frac{\partial L}{\partial \dot{\mathbf{q}}} \right]^T - \left[ \frac{\partial L}{\partial \mathbf{q}} \right] + \mathbf{\Psi}_q^T \lambda \quad (2.23)$$

Where,

$\mathbf{F}$  : is the vector sum of nonconservative external forces. In the absence of external forces this is simply equal to the joint torques,  $\Gamma$

$\mathbf{\Psi} = \frac{\partial \Psi}{\partial \mathbf{q}}$  is  $c \times N$  matrix with  $c$  the number of constraints and  $N$  the number of parameters.  
 $\mathbf{\Psi} = [\mathbf{C}^T \quad \mathbf{B}^T \quad \mathbf{A}^T]^T$

$\lambda$  : is a  $c \times 1$  vector of Lagrange multipliers

$\mathbf{q} = [\mathbf{q}_1, \mathbf{q}_2, \dots, \mathbf{q}_n]^T$ , refers to the concatenation of the generalized coordinate vectors of each beam in the system

<sup>4</sup>Attention must be paid to the ordering of the elastic terms in the generalized coordinate vector

The  $\Psi$  matrix is referred to as a Jacobian matrix in robotics literature and is responsible for the loop closure equations as discussed in section 2.2.4. It should be noted that the potential energy term, in the case of flexible manipulators, refers to both the gravitational potential energy and the elastic potential energy  $U = V_g + V_e$  [2, 22, 25]. The Lagrangian formulation 2.23 is now developed in a stepwise manner:

### Kinetic Energy

First the time-velocity derivative term is analyzed. Note that a new inertia matrix,  $M_R$ , is used. This matrix is appropriately oriented within the global reference frame as shown in equation 2.25.

$$\frac{d}{dt} \left[ \frac{\partial E}{\partial \dot{\mathbf{q}}} \right]^T = \frac{d}{dt} \left[ \frac{\partial \frac{1}{2} \dot{\mathbf{q}}^T \mathbf{M}_R \dot{\mathbf{q}}}{\partial \dot{\mathbf{q}}} \right]^T \quad (2.24)$$

with,

$$\mathbf{M}_R = \mathbf{R}_{\text{tot}} \mathbf{M}_{\text{tot}} \mathbf{R}_{\text{tot}}^T$$

where,

$$\mathbf{R}_{\text{tot}} = \begin{bmatrix} \mathbf{R}_1 & \mathbf{0} & \dots & \mathbf{0} \\ \mathbf{0} & \mathbf{R}_2 & \dots & \mathbf{0} \\ \vdots & \vdots & \ddots & \vdots \\ \mathbf{0} & \mathbf{0} & \dots & \mathbf{R}_n \end{bmatrix}$$

and,

$$\mathbf{R}_j = \begin{bmatrix} \mathbf{R}(\theta_j) & \mathbf{0} \\ \mathbf{0} & \mathbf{I}_{k_j \times k_j} \end{bmatrix} \quad (2.25)$$

where,

$\theta_j$  : is the rotational term in the generalized coordinate vector  $\mathbf{q}_j$

$k_j$  : refers to the number of modes included on beam  $j$

The result of equation 2.24 may thus be expressed as follows:

$$\frac{d}{dt} \left[ \frac{\partial E}{\partial \dot{\mathbf{q}}} \right]^T = \mathbf{M}_R \ddot{\mathbf{q}} + \dot{\mathbf{M}}_R \dot{\mathbf{q}} \quad (2.26)$$

with,

$$\dot{\mathbf{M}}_R = \dot{\mathbf{R}}_{\text{tot}} \mathbf{M}_{\text{tot}} \mathbf{R}_{\text{tot}}^T + \mathbf{R}_{\text{tot}} \dot{\mathbf{M}}_{\text{tot}} \mathbf{R}_{\text{tot}}^T + \mathbf{R}_{\text{tot}} \mathbf{M}_{\text{tot}} \dot{\mathbf{R}}_{\text{tot}}^T$$

As seen earlier, the inertia matrix  $\mathbf{M}_{\text{tot}}$  is a function of the elastic coordinates  $\mathbf{q}_e$ , which, in turn are time variant, thus the time derivative leads to the  $\dot{\mathbf{M}}_{\text{tot}}$  term seen in equation 2.1.6.

Next the positional derivative term may be evaluated, this is done for each generalized coordinate  $h$ :

$$\frac{\partial E}{\partial \mathbf{q}_h} = \frac{\partial \frac{1}{2} \dot{\mathbf{q}}^T \mathbf{M}_R \dot{\mathbf{q}}}{\partial \mathbf{q}_h} = \frac{1}{2} \dot{\mathbf{q}}^T \mathbf{M}_{R_{q_h}} \dot{\mathbf{q}} \quad (2.27)$$

where,

$$\mathbf{M}_{R_{q_h}} = \mathbf{R}_{q_h} \mathbf{M}_R \mathbf{R}_{q_h}^T + \mathbf{R} \mathbf{M}_{q_h} \mathbf{R}^T + \mathbf{R} \mathbf{M}_R \mathbf{R}_{q_h}^T$$

Collectively, the position derivative of beam  $j$  may be written:

$$\frac{\partial E}{\partial \mathbf{q}_j} = \mathbf{M}_{R_{q_j}} = \begin{bmatrix} 0 \\ 0 \\ \frac{1}{2} \dot{\mathbf{q}}_j^T \left( \mathbf{R}_{\theta_j} \mathbf{M}_j \mathbf{R}_{\theta_j}^T + \mathbf{R} \mathbf{M}_j \mathbf{R}_{\theta_j}^T \right) \dot{\mathbf{q}}_j \\ \frac{1}{2} \dot{\mathbf{q}}_j^T \left( \mathbf{R} \mathbf{M}_{q_{e_j}} \mathbf{R} \right) \dot{\mathbf{q}}_j \end{bmatrix}_{(3+k_j) \times 1} \quad (2.28)$$

where

$k_j$  : refers to the number of modes modeled on beam  $j$

$$\mathbf{R}_\theta = \begin{bmatrix} -\sin \theta & -\cos \theta \\ \cos \theta & -\sin \theta \end{bmatrix}$$

### Elastic Potential Energy

The elastic potential energy is not a function of  $\dot{\mathbf{q}}$  and thus the time-velocity derivative term is zero. The position derivative term is left to be determined as follows, note that this term is in fact only related to the elastic coordinates  $\mathbf{q}_e$  due to the construction of  $\mathbf{K}_{\text{tot}}$  in equation 2.21:

$$\frac{\partial V_e}{\partial \mathbf{q}} = \frac{\partial \frac{1}{2} \mathbf{q} \mathbf{K}_{\text{tot}} \mathbf{q}}{\partial \mathbf{q}} = \mathbf{K}_{\text{tot}} \mathbf{q} \quad (2.29)$$

It can be seen that this term reduces the well known Hook's law, relating an applied force to a corresponding elastic deformation.

### Gravitational Potential Energy

Finally the gravitational potential energy may be assessed. The gravitational potential energy  $V_{g_j}$  for beam  $j$  is determined at the beam mid-point using the mass  $m_j$  of the link:

$$V_{g_j} = \int_m \mathbf{g}^T \overrightarrow{OM_j^*} dm = \mathbf{m}_j \mathbf{g}^T \int_0^1 \overrightarrow{OM_j^*} d\xi \quad (2.30)$$

with  $\overrightarrow{OM_j^*}$ :

$$\overrightarrow{OM_j^*} = \underbrace{\begin{bmatrix} x_{A_j} \\ y_{A_j} \end{bmatrix}}_{\overrightarrow{OM_j}} + \mathbf{R} \begin{bmatrix} \frac{l_j}{2} \\ 0 \end{bmatrix} + \mathbf{R} \underbrace{\begin{bmatrix} u_{x_j}(\xi, t) \\ u_{y_j}(\xi, t) \end{bmatrix}}_{\overrightarrow{MM_j^*}} \quad (2.31)$$

with  $u_{x_j} = \phi_{x_j}(\xi) \mathbf{q}_{e_{x_j}}$ ,  $u_{y_j} = \phi_{y_j}(\xi) \mathbf{q}_{e_{y_j}}$ , and  $\mathbf{g} = [0 - g]^T$ , the term for the gravitational effects can be found from:

$$\mathbf{V}_{g_j} = \mathbf{m}_j g (y_{A_j} + \frac{l}{2} \sin(\theta_j) + \alpha \mathbf{q}_{e_j}) \quad (2.32)$$

where,  $\alpha$ : is a vector depending on  $\theta_j$ . The gravitational efforts may be found from:

$$\frac{\mathbf{V}_{g_j}}{\mathbf{q}_j} = \mathbf{Q}_j^T \quad (2.33)$$

### Open Loop Lagrangian Formulation

The terms developed in the preceding subsections may now be combined to form the open loop Lagrangian formulation, that is to say, that at this point in time, the closure constraints are ignored:

$$\mathbf{F} = \mathbf{M}_R \ddot{\mathbf{q}} + \mathbf{H} \quad (2.34)$$

where the Coriolis and gravitational elements are included in the vector  $\mathbf{H}$ :

$$\mathbf{H} = \dot{\mathbf{M}}_R \dot{\mathbf{q}} - (\mathbf{M}_{R_q} - \mathbf{K}_{\text{tot}} \mathbf{q} - \mathbf{Q}) \quad (2.35)$$

### Ordering and regrouping of the Lagrangian Formulation

It is desired to collect and reorder the elements in equation 2.34 according to the *actuated*, *elastic* and *passive* coordinates. This reordering allows the elastodynamic model to conform to the modeling used during the development of the kinematic relations of the system. The process of reordering may be explained as follows:

- Identify all actuated coordinates, note their indexing and assign them to the vector  $\mathbf{q}_a$
- Identify all elastic coordinates, note their indexing and assign them to the vector  $\mathbf{q}_e$
- Identify all passive coordinates, note their indexing and assign them to the vector  $\mathbf{q}_p$ . If there are supplementary passive coordinates, such as the inclusion of lumped masses or inertias, their associated coordinates be appended to  $\mathbf{q}_p$ . The inclusion of these masses must be reflected on the diagonal of the mass matrix  $\mathbf{M}_R$  and must also be appended to the gravitational efforts  $\mathbf{Q}$ <sup>5</sup>
- Identify all coordinates which are implicitly constrained. Eliminate the corresponding rows and columns from  $\mathbf{M}_{tot}$  and eliminate the appropriate elements from the Coriolis and gravitational terms vector  $\mathbf{H}$ . Implicitly constrained coordinates are coordinates which can, under no condition, experience any form of motion. For the five bar mechanism considered, the set of implicitly constrained generalized coordinates are the  $x$  and  $y$  base positions of the actuated links.

The reordering allows the independent and dependent coordinates to be distinguished as  $\mathbf{q}_i = [\mathbf{q}_a, \mathbf{q}_e]^T$  and  $\mathbf{q}_d = \mathbf{q}_p$ . This gives rise to the generalized coordinate vector of the following form:

$$\mathbf{q} = \begin{bmatrix} \mathbf{q}_i \\ \mathbf{q}_d \end{bmatrix} = \begin{bmatrix} \mathbf{q}_a \\ \mathbf{q}_e \\ \mathbf{q}_p \end{bmatrix} \quad (2.36)$$

The open loop Lagrangian expression may thus be written with greater detail:

$$\begin{bmatrix} \Gamma_a \\ \Gamma_e \\ \Gamma_p \end{bmatrix} = \begin{bmatrix} \mathbf{M}_{aa} & \mathbf{M}_{ae} & \mathbf{M}_{ap} \\ \mathbf{M}_{ea} & \mathbf{M}_{ee} & \mathbf{M}_{ep} \\ \mathbf{M}_{pa} & \mathbf{M}_{pe} & \mathbf{M}_{pp} \end{bmatrix} \begin{bmatrix} \ddot{\mathbf{q}}_a \\ \ddot{\mathbf{q}}_e \\ \ddot{\mathbf{q}}_p \end{bmatrix} + \begin{bmatrix} \mathbf{H}_a \\ \mathbf{H}_e \\ \mathbf{H}_p \end{bmatrix} \quad (2.37)$$

#### 2.1.7 Closed Form Dynamic Models

The closure constraints may be introduced into equation 2.37. This will allow the formulation of the inverse and direct dynamic models. These models are used as follows:

- The inverse dynamic model, delivers the required actuator efforts  $\tau_a$  and the resultant elastic deformations in acceleration,  $\ddot{\mathbf{q}}_e$ , as a function of a desired trajectory in the actuated coordinates  $\mathbf{q}_a$ ,  $\dot{\mathbf{q}}_a$  and  $\ddot{\mathbf{q}}_a$
- The direct dynamic model, determines the resultant independent coordinate accelerations as a response to an applied  $\tau_a$ . This is to say that the direct dynamic model determines  $\dot{\mathbf{q}}_i = [\dot{\mathbf{q}}_a, \dot{\mathbf{q}}_e]^T$ <sup>6</sup>

The complete system of equations for a closed loop robot is written:

$$\begin{bmatrix} \mathbf{I} & \mathbf{0} & \mathbf{C}_{n_a \times n_p}^T \\ \mathbf{0} & \mathbf{I} & \mathbf{B}_{n_e \times n_p}^T \\ \mathbf{0} & \mathbf{0} & \mathbf{A}_{n_p \times n_p}^T \end{bmatrix} \begin{bmatrix} \tau_a \\ \tau_e \\ \lambda \end{bmatrix} = \begin{bmatrix} \Gamma_a \\ \Gamma_e \\ \Gamma_p \end{bmatrix} = \begin{bmatrix} \mathbf{M}_{aa} & \mathbf{M}_{ae} & \mathbf{M}_{ap} \\ \mathbf{M}_{ea} & \mathbf{M}_{ee} & \mathbf{M}_{ep} \\ \mathbf{M}_{pa} & \mathbf{M}_{pe} & \mathbf{M}_{pp} \end{bmatrix} \begin{bmatrix} \ddot{\mathbf{q}}_a \\ \ddot{\mathbf{q}}_e \\ \ddot{\mathbf{q}}_p \end{bmatrix} + \begin{bmatrix} \mathbf{H}_a \\ \mathbf{H}_e \\ \mathbf{H}_p \end{bmatrix} \quad (2.38)$$

<sup>5</sup>Additional lumped masses do not invoke Coriolis effects and are represented as zeros in the vector  $\mathbf{H}_p$

<sup>6</sup>Note that  $\mathbf{q}_a$  and  $\mathbf{q}_e$  are not dynamically independent as the elastic deformations emerge from actuation of the system

In equation 2.38, the following assumptions are made:

- $\mathbf{\Gamma}_p = \mathbf{A}^T \lambda$ , in other words, there are no efforts exerted directly on the passive coordinates. The effect of the passive coordinates are represented by  $\lambda$  and will be grouped on the independent coordinates.
- $\tau_e = 0$ , the elastic coordinates are un-actuated and all dynamic and gravitational efforts exerted on the elastic coordinates will be in equilibrium due to Hook's law,  $\mathbf{K}_{tot} \mathbf{q}$

The effect constraints will be observable on the actuated and elastic coordinates, equation 2.38 may be reduced. Firstly, the dynamic relations for the independent coordinates,  $\mathbf{q}_i = [\mathbf{q}_a \mathbf{q}_e]^T$ , are expressed as follows:

$$\begin{bmatrix} \mathbf{I} & \mathbf{0} \\ \mathbf{0} & \mathbf{I} \end{bmatrix} \begin{bmatrix} \tau_a \\ \mathbf{0} \end{bmatrix} = \begin{bmatrix} \mathbf{M}_{aa} & \mathbf{M}_{ae} & \mathbf{M}_{ap} \\ \mathbf{M}_{ea} & \mathbf{M}_{ee} & \mathbf{M}_{ep} \end{bmatrix} \begin{bmatrix} \ddot{\mathbf{q}}_a \\ \ddot{\mathbf{q}}_e \end{bmatrix} + \begin{bmatrix} \mathbf{H}_a \\ \mathbf{H}_e \end{bmatrix} + \begin{bmatrix} \mathbf{C}^T \\ \mathbf{B}^T \end{bmatrix} \lambda \quad (2.39)$$

Secondly, considering the dependent coordinates  $\mathbf{q}_d = \mathbf{q}_p$ , the expression for  $\lambda$  is developed:

$$\mathbf{A}^T \lambda = [\mathbf{M}_{pa} \quad \mathbf{M}_{pe} \quad \mathbf{M}_{pp}] \begin{bmatrix} \ddot{\mathbf{q}}_a \\ \ddot{\mathbf{q}}_e \\ \ddot{\mathbf{q}}_p \end{bmatrix} + \mathbf{H}_p \quad (2.40)$$

Solving for the vector Lagrange multipliers  $\lambda$ :

$$\lambda = \mathbf{A}^{T^{-1}} \left( [\mathbf{M}_{pa} \quad \mathbf{M}_{pe} \quad \mathbf{M}_{pp}] \begin{bmatrix} \ddot{\mathbf{q}}_a \\ \ddot{\mathbf{q}}_e \\ \ddot{\mathbf{q}}_p \end{bmatrix} + \mathbf{H}_p \right)$$

Having obtained an expression for  $\lambda$ , substitution into equation 2.39 gives:

$$\begin{bmatrix} \mathbf{I} & \mathbf{0} \\ \mathbf{0} & \mathbf{I} \end{bmatrix} \begin{bmatrix} \tau_a \\ \mathbf{0} \end{bmatrix} = \begin{bmatrix} \mathbf{M}_{aa} - \mathbf{C}^T \mathbf{A}^{T^{-1}} \mathbf{M}_{pa} & \mathbf{M}_{ae} - \mathbf{C}^T \mathbf{A}^{T^{-1}} \mathbf{M}_{pe} & \mathbf{M}_{ap} - \mathbf{C}^T \mathbf{A}^{T^{-1}} \mathbf{M}_{pp} \\ \mathbf{M}_{ea} - \mathbf{B}^T \mathbf{A}^{T^{-1}} \mathbf{M}_{pa} & \mathbf{M}_{ee} - \mathbf{B}^T \mathbf{A}^{T^{-1}} \mathbf{M}_{pe} & \mathbf{M}_{ep} - \mathbf{B}^T \mathbf{A}^{T^{-1}} \mathbf{M}_{pp} \end{bmatrix} \begin{bmatrix} \ddot{\mathbf{q}}_a \\ \ddot{\mathbf{q}}_e \\ \ddot{\mathbf{q}}_p \end{bmatrix} + \begin{bmatrix} \mathbf{H}_a - \mathbf{C}^T \mathbf{A}^{T^{-1}} \mathbf{H}_p \\ \mathbf{H}_e - \mathbf{B}^T \mathbf{A}^{T^{-1}} \mathbf{H}_p \end{bmatrix} \quad (2.41)$$

Using the kinematic relations to express the passive joint accelerations,  $\ddot{\mathbf{q}}_p$ , a method for grouping dynamic effects related to the dependent coordinates on the independent coordinates:

$$\ddot{\mathbf{q}}_p = -\mathbf{A}^{-1}(\dot{\mathbf{A}}\dot{\mathbf{q}}_p + \dot{\mathbf{B}}\dot{\mathbf{q}}_e) + \dot{\mathbf{C}}\dot{\mathbf{q}}_a + \mathbf{B}\dot{\mathbf{q}}_e + \mathbf{C}\dot{\mathbf{q}}_a$$

Such that;

$$\begin{bmatrix} \mathbf{M}_{ap} - \mathbf{C}^T \mathbf{A}^{T^{-1}} \mathbf{M}_{pp} \\ \mathbf{M}_{ep} - \mathbf{B}^T \mathbf{A}^{T^{-1}} \mathbf{M}_{pp} \end{bmatrix} \ddot{\mathbf{q}}_p \quad (2.42)$$

Adopting the notations,

$$\begin{aligned} \mathbf{J}_a &= -\mathbf{A}^{-1} \mathbf{C} \mathbf{J}_e = -\mathbf{A}^{-1} \mathbf{B} & \dot{\mathbf{J}}_a &= -\mathbf{A}^{-1} \dot{\mathbf{C}} \\ \dot{\mathbf{J}}_e &= -\mathbf{A}^{-1} \dot{\mathbf{B}} \mathbf{J}_p = -\mathbf{A}^{-1} \dot{\mathbf{A}} \end{aligned}$$

The reduced inertia matrix is derived:

$$\mathbf{M}^* = \begin{bmatrix} \mathbf{M}_{aa}^* & \mathbf{M}_{ae}^* \\ \mathbf{M}_{ea}^* & \mathbf{M}_{ee}^* \end{bmatrix} \begin{bmatrix} \ddot{\mathbf{q}}_a \\ \ddot{\mathbf{q}}_e \end{bmatrix} \quad (2.43)$$

With the constituent terms as follows:

$$\begin{aligned}
\mathbf{M}_{aa}^* &= \mathbf{M}_{aa} + \mathbf{J}_a^T \mathbf{M}_{pa} + \mathbf{M}_{ap} \mathbf{J}_a + \mathbf{J}_a^T \mathbf{M}_{pp} \mathbf{J}_a \\
\mathbf{M}_{ae}^* &= \mathbf{M}_{ae} + \mathbf{J}_a^T \mathbf{M}_{pe} + \mathbf{M}_{ap} \mathbf{J}_e + \mathbf{J}_a^T \mathbf{M}_{pp} \mathbf{J}_e \\
\mathbf{M}_{ea}^* &= \mathbf{M}_{ea} + \mathbf{J}_e^T \mathbf{M}_{pa} + \mathbf{M}_{ep} \mathbf{J}_a + \mathbf{J}_e^T \mathbf{M}_{pp} \mathbf{J}_a \\
\mathbf{M}_{ee}^* &= \mathbf{M}_{ee} + \mathbf{J}_e^T \mathbf{M}_{pe} + \mathbf{M}_{ep} \mathbf{J}_e + \mathbf{J}_e^T \mathbf{M}_{pp} \mathbf{J}_e
\end{aligned} \tag{2.44}$$

The reduced Coriolis and gravitational effect vector, for the actuated coordinates is:

$$\mathbf{H}_a^* = \mathbf{H}_a + \mathbf{J}_a^T \mathbf{H}_p + \left( \mathbf{M}_{ap} [\dot{\mathbf{J}}_a \quad \dot{\mathbf{J}}_e \quad \dot{\mathbf{J}}_p] + \mathbf{J}_a^T \mathbf{M}_{pp} [\dot{\mathbf{J}}_a \quad \dot{\mathbf{J}}_e \quad \dot{\mathbf{J}}_p] \right) \begin{bmatrix} \dot{\mathbf{q}}_a \\ \dot{\mathbf{q}}_e \\ \dot{\mathbf{q}}_p \end{bmatrix}$$

For the elastic coordinates:

$$\mathbf{H}_e^* = \mathbf{H}_e + \mathbf{J}_e^T \mathbf{H}_p + \left( \mathbf{M}_{ep} [\dot{\mathbf{J}}_a \quad \dot{\mathbf{J}}_e \quad \dot{\mathbf{J}}_p] + \mathbf{J}_e^T \mathbf{M}_{pp} [\dot{\mathbf{J}}_a \quad \dot{\mathbf{J}}_e \quad \dot{\mathbf{J}}_p] \right) \begin{bmatrix} \dot{\mathbf{q}}_a \\ \dot{\mathbf{q}}_e \\ \dot{\mathbf{q}}_p \end{bmatrix}$$

Finally we can write the closed loop dynamic model as follows:

$$\begin{bmatrix} \tau_a \\ \mathbf{0} \end{bmatrix} = \begin{bmatrix} \mathbf{M}_{aa}^* & \mathbf{M}_{ae}^* \\ \mathbf{M}_{ea}^* & \mathbf{M}_{ee}^* \end{bmatrix} \begin{bmatrix} \ddot{\mathbf{q}}_a \\ \ddot{\mathbf{q}}_e \end{bmatrix} + \begin{bmatrix} \mathbf{H}_a^* \\ \mathbf{H}_e^* \end{bmatrix} \tag{2.45}$$

### 2.1.8 Direct Dynamic Model

The preceding equations may be used to develop the direct dynamic model of the closed loop robot. In the direct dynamic model, the generalized efforts  $\tau_a$  are known and the independent coordinate accelerations  $\ddot{\mathbf{q}}_i$  are sought. Two formulations are presented here.

#### DDM: Classical Formulation

$$\begin{bmatrix} \ddot{\mathbf{q}}_a \\ \ddot{\mathbf{q}}_e \end{bmatrix} = \begin{bmatrix} \mathbf{M}_{aa}^* & \mathbf{M}_{ae}^* \\ \mathbf{M}_{ea}^* & \mathbf{M}_{ee}^* \end{bmatrix}^{-1} \left( \begin{bmatrix} \tau_a \\ \mathbf{0} \end{bmatrix} - \begin{bmatrix} \mathbf{H}_a^* \\ \mathbf{H}_e^* \end{bmatrix} - \begin{bmatrix} \mathbf{0} \\ \mathbf{K}_{qe} \end{bmatrix} \right) \tag{2.46}$$

From a simulation point of view, it was found that the classical formulation was numerically unstable due to the numerical integration needed to find the independent coordinate velocities  $\dot{\mathbf{q}}_i$  and positions  $\mathbf{q}_i$ . To overcome this problem, a recursive scheme solving rather for the actuated coordinate accelerations  $\ddot{\mathbf{q}}_a$  and the elastic coordinate positions  $\mathbf{q}_e$  was opted for. It should be noted that while the actuated coordinates,  $\mathbf{q}_a$  may be geometrically independent from the elastic coordinates  $\mathbf{q}_e$ , they are however dynamically dependent. This is due to the fact that the elastic deformations are as a result of the actuated dynamics of the system.

#### DDM: Alternate Formulation

The alternate formulation opts to solve for  $\mathbf{q}_e$  and thus  $\ddot{\mathbf{q}}_e$  may be found through derivation. Equation 2.45 may be developed as follows:

$$\mathbf{0} = \mathbf{M}_{ea}^* \ddot{\mathbf{q}}_a + \mathbf{M}_{ee} \ddot{\mathbf{q}}_e + \mathbf{H}_e^*$$

Extracting the stiffness term from  $\mathbf{H}_e^*$ ,  $\mathbf{q}_e$  may be found:

$$\mathbf{q}_e = \mathbf{K}_e^{-2} (\mathbf{M}_{ea}^* \ddot{\mathbf{q}}_a + \mathbf{M}_{ee} + \mathbf{H}_e^{**}) \tag{2.47}$$

Solving for  $\ddot{\mathbf{q}}_{\mathbf{a}}$

$$\tau_{\mathbf{a}} = \mathbf{M}_{\mathbf{aa}}^* \ddot{\mathbf{q}}_{\mathbf{a}} + \mathbf{M}_{\mathbf{ae}} + \mathbf{H}_{\mathbf{a}}^*$$

Thus,

$$\ddot{\mathbf{q}}_{\mathbf{a}} = \mathbf{M}_{\mathbf{aa}}^{*-1} (\tau_{\mathbf{a}} - \mathbf{M}_{\mathbf{ae}} - \mathbf{H}_{\mathbf{a}}^*) \quad (2.48)$$

The alternate formulation seemingly decouples the dynamic dependence of the elastic deformations from the actuated dynamics. However, if the  $\mathbf{q}_{\mathbf{e}}$  is solved for recursively, with the generalized velocities and accelerations being modified with in each recursion, equation 2.45 will converge to an admissible result. This method facilitates and ensures stability of the simulation process.

### 2.1.9 Inverse Dynamic Model

In the inverse dynamic problem,  $\ddot{\mathbf{q}}_{\mathbf{a}}$  is known and the required efforts  $\tau_{\mathbf{a}}$  and emergent  $\ddot{\mathbf{q}}_{\mathbf{e}}$  are sought. Again the classical and alternate formulations of the elastodynamic problem is presented (figure 2.3):

#### IDM: Classical Formulation

The dynamic dependence between actuated and elastic coordinates is evident from the fact that it is first necessary to solve for  $\ddot{\mathbf{q}}_{\mathbf{e}}$  before the solution for  $\tau_{\mathbf{q}}$  can be found:

$$\ddot{\mathbf{q}}_{\mathbf{e}} = -\mathbf{M}_{\mathbf{ee}}^{*-1} (\mathbf{M}_{\mathbf{ea}}^* \ddot{\mathbf{q}}_{\mathbf{a}} + \mathbf{H}_{\mathbf{e}}^* + \mathbf{K}_{\mathbf{qe}}) \quad (2.49)$$

$$\tau_{\mathbf{a}} = [\mathbf{M}_{\mathbf{aa}}^* \quad \mathbf{M}_{\mathbf{ae}}^*] \begin{bmatrix} \ddot{\mathbf{q}}_{\mathbf{a}} \\ \ddot{\mathbf{q}}_{\mathbf{e}} \end{bmatrix} + \mathbf{H}_{\mathbf{a}}^* \quad (2.50)$$

Again, for simulation purposes, the alternate formulation of the inverse dynamic problem is developed. Note that the alternate formulation of the IDM, requires significantly less manipulation of the dynamic equations<sup>7</sup>:

#### IDM: Alternate Formulation

$$\begin{bmatrix} \tau_{\mathbf{a}} \\ -\mathbf{K}_{\mathbf{qe}} \end{bmatrix} = \begin{bmatrix} \mathbf{I} & \mathbf{0} & \mathbf{J}_{\mathbf{a}}^T \\ \mathbf{0} & \mathbf{I} & \mathbf{J}_{\mathbf{e}}^T \end{bmatrix} \begin{bmatrix} \Gamma_{\mathbf{a}} \\ \Gamma_{\mathbf{e}} \Gamma_{\mathbf{p}} \end{bmatrix} \quad (2.51)$$

The expressions for  $\tau_{\mathbf{e}}$  and  $\mathbf{q}_{\mathbf{e}}$  are thus as follows:

$$\tau_{\mathbf{a}} = \Gamma_{\mathbf{a}} + \mathbf{J}_{\mathbf{a}}^T \Gamma_{\mathbf{p}} \quad (2.52)$$

$$\mathbf{q}_{\mathbf{e}} = -\mathbf{K}_{\mathbf{e}}^{-1} (\Gamma_{\mathbf{e}} + \mathbf{J}_{\mathbf{e}}^T \Gamma_{\mathbf{p}}) \quad (2.53)$$

The alternate solution of the inverse dynamic model is also solved for recursively with appropriate updating of the coordinate velocities and accelerations to ensure convergence. The simulations of the IDM and the DDM have been coupled to verify that they are indeed inverse operations.

---

<sup>7</sup>Note the the stiffness term in  $H_{\mathbf{e}}^*$  has been moved to the left hand side of equation 2.51

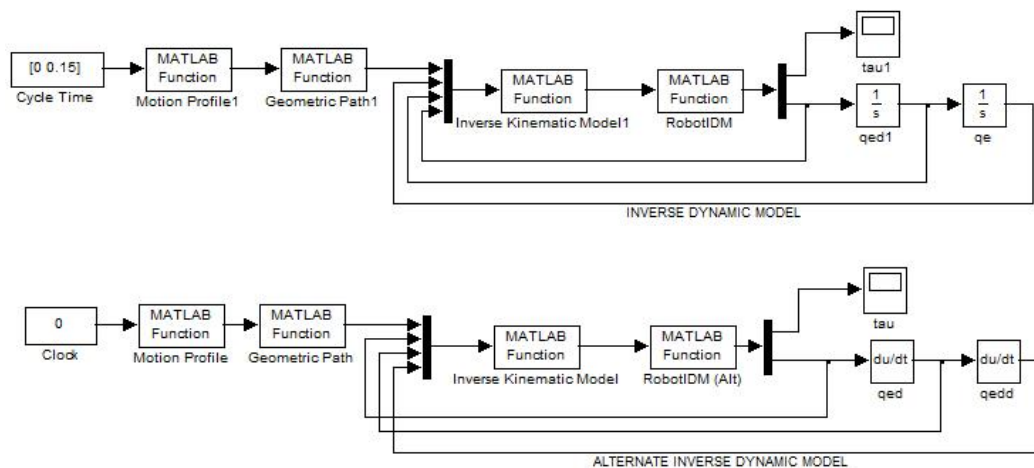


Figure 2.3: Schematic of the simulated system

### 2.1.10 Five Bar Mechanism Model

The dimensioning and parametrization of the five bar mechanism was chosen as follows:

Links	$l_i$ Length [m]	$D_i$ Diameter [d]	$m_i$ Mass [kg]
<i>link1</i>	0.24	0.035	0.6258
<i>link2</i>	0.38079	0.035	0.9928
Other Parameters			
$a$	Base offset [m]	0.1	
$\rho$	Density [ $kg/m^3$ ]	2710	
$Y$	Young's Modulus [GPa]	70	

Table 2.2: Parameters of the modeled five bar mechanism

For a link  $i$  in bending, the following mass and stiffness matrices are obtained. The mass matrix is a  $6 \times 6$  matrix, the first three columns are:

$$\mathbf{M}_i = m_i \begin{bmatrix} 1 & 0 & \delta_1 & 0 & 0 & 0 \\ 0 & 1 & 0.5l_i & 1.067 & 0.4260 & 0.2586 \\ \delta_1 & 0.5l_i & \delta_2 & 0.7748l_i & 0.08905l_i & 0.03587l_i \\ 0 & 1.067 & 0.7748l_i & 1.8564 & 0 & 0 \\ 0 & 0.4260 & 0.08905l_i & 0 & 0.9641 & 0 \\ 0 & 0.2586 & 0.03587l_i & 0 & 0 & 0 \end{bmatrix} \quad (2.54)$$

with,

$$\begin{aligned} \delta_1 &= -1.067q_{i_{e_1}} - 0.4260q_{i_{e_2}} - 0.2586q_{i_{e_3}} \\ \delta_2 &= (1.856q_{i_{e_1}}^2 + 0.9641q_{i_{e_2}}^2 + 1.006q_{i_{e_3}}^2 + 0.333l_i^2) \end{aligned}$$

The region of the bending stiffness matrix contains non zero elements for the region related to the elastic coordinates:

$$\mathbf{K}_{i:,4:6} = \frac{YI_i}{l_i^3} \begin{bmatrix} 22.93 & ,0 & 0 \\ 0 & 468.0 & ,0 \\ 0 & 0 & 3952 \end{bmatrix} \quad (2.55)$$



where  $I_i = \frac{\pi D_i^4}{64}$  is the second moment of inertia area of the beam

For a link  $i$  in tension-compression, the following form of mass matrix is obtained:

$$\mathbf{M}_i = m_i \begin{bmatrix} 1 & 0 & 0 & 0.6366 & 0.2122 & 0.1273 \\ 0 & 1 & \delta_1 & 0 & 0 & 0 \\ 0 & \delta_1 & \delta_2 & 0 & 0 & 0 \\ 0.6366 & 0 & 0 & 0.5 & 0 & 0 \\ 0.2122 & 0 & 0 & 0 & 0.5 & 0 \\ 0.1273 & 0 & 0 & 0 & 0 & 0.5 \end{bmatrix} \quad (2.56)$$

with

$$\begin{aligned} \delta_1 &= 0.5l_i + 0.6366q_{i_{e_1}} + 0.2122q_{i_{e_2}} + 0.1273q_{i_{e_3}} \\ \delta_2 &= 0.333l_i^2 + 0.8106l_iq_{i_{e_1}} - 0.09006l_iq_{i_{e_2}} + 0.03242l_iq_{i_{e_3}} + 0.5q_{i_{e_1}}^2 \\ &\quad + 0.5q_{i_{e_2}}^2 + 0.5q_{i_{e_3}}^2 \end{aligned}$$

The region of the tension compression stiffness matrix:

$$\mathbf{K}_{i:,4:6} = \frac{YA_i}{l_i} \begin{bmatrix} 1.23370 & 0 & 0 \\ 0 & 11.1033 & 0 \\ 0 & 0 & 30.8425 \end{bmatrix} \quad (2.57)$$

where  $A_i = \frac{\pi D_i^2}{4}$  is the cross-sectional area of the beam

The mass and stiffness matrices are used in equations 2.20 and 2.21 to construct the total mass and stiffness matrices. In the next section, these matrices, and the model which they represent are compared and verified against a finite element model.

## 2.2 Geometric and Kinematic Modeling

### 2.2.1 Rigid Inverse Geometric Model

The parallel robot is controlled with a desired trajectory in the task space, for this the inverse geometric model is needed. First the rigid inverse geometric model is developed. This model allows the active joint trajectories to be computed<sup>8</sup>. As the number of degrees of freedom of the end effector are the same as the number of degrees of freedom for a single leg, each leg may be treated separately. The parallel robot may be seen as the combination of two kinematic chains, each being a SCARA type robot meeting at the end effector position from the right and the left.

The rigid case assumes that the end effector position  $\mathbf{X}$  is known, with it, the joint variables for each leg may be found. The position of the end effector as seen in the left leg may be expressed as follows:

$$\begin{bmatrix} x \\ y \end{bmatrix} = \begin{bmatrix} -a \\ 0 \end{bmatrix} + l_1 \begin{bmatrix} \cos q_{11} \\ \sin q_{11} \end{bmatrix} + l_2 \begin{bmatrix} \cos q_{12} \\ \sin q_{12} \end{bmatrix} \quad (2.58)$$

Similarly, we can express the position of the end effector in terms of the joint variables associated with the right leg:

$$\begin{bmatrix} x \\ y \end{bmatrix} = \begin{bmatrix} a \\ 0 \end{bmatrix} + l_1 \begin{bmatrix} \cos q_{21} \\ \sin q_{21} \end{bmatrix} + l_2 \begin{bmatrix} \cos q_{22} \\ \sin q_{22} \end{bmatrix} \quad (2.59)$$

<sup>8</sup>The active joints are also referred to as the actuated coordinates in the context of the set of generalized coordinates

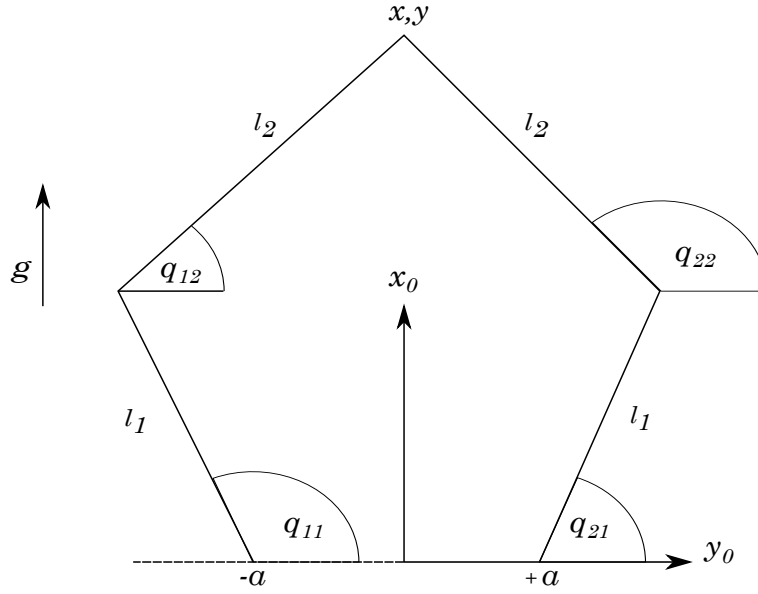


Figure 2.4: Rigid Geometric Model

### Active Joint Variables

The rigid inverse geometric model is computed by expressing the length,  $l_2$  in terms of the active joint variable,  $q_{11}$  and  $q_{21}$ . For the left leg:

$$\begin{aligned}
 l_2^2 &= [x - (-a + l_1 \cos q_{11})]^2 + [y - (l_1 \sin q_{11})]^2 \\
 &\Leftrightarrow -2l_1(x + a) \cos q_{11} - 2l_1 \sin q_{11} + [(x + a)^2 + y^2 + l_1^2 - l_2^2] \\
 &\Leftrightarrow A_1 \cos q_{11} + B_1 \sin q_{11} + C_1
 \end{aligned} \tag{2.60}$$

Following the development in [10], assign:

$$t_1 = \tan \frac{q_{11}}{2}$$

thus,

$$\cos q_{11} = \frac{1 - t_1^2}{1 + t_1^2} \quad \sin q_{11} = \frac{2t_1}{1 + t_1^2}$$

Solving for  $q_{11}$ ,

$$q_{11} = 2 \tan^{-1} \left( \frac{-B_1 + \varepsilon \sqrt{B_1^2 + A_1^2 - C_1^2}}{C_1 - A_1} \right) \quad \text{for } B_1^2 + A_1^2 \geq C_1^2 \tag{2.61}$$

with  $\varepsilon = \pm 1$

Similarly for the right leg, the following is obtained:

$$\begin{aligned}
 l_2^2 &= [(a + l_1 \cos q_{21}) - x]^2 + [(l_1 \sin q_{21}) - y]^2 \\
 &\Leftrightarrow A_2 \cos q_{21} + B_2 \sin q_{21} + C_2
 \end{aligned} \tag{2.62}$$

thus,

$$q_{21} = 2 \tan^{-1} \left( \frac{-B_2 + \varepsilon \sqrt{B_2^2 + A_2^2 - C_2^2}}{C_2 - A_2} \right) \quad \text{for } B_2^2 + A_2^2 \geq C_2^2 \tag{2.63}$$

with  $\varepsilon = \pm 1$

### Passive Joint Variables

The passive joint variables,  $q_{12}$  and  $q_{22}$ , may now be computed. For the left leg,

$$\begin{aligned}\cos q_{12} &= \frac{x - (-a + l_1 \cos q_{11})}{l_2} \\ \sin q_{12} &= \frac{y - (-l_1 \sin q_{11})}{l_2}\end{aligned}$$

Giving,

$$q_{12} = \text{atan2}(\sin q_{12}, \cos q_{12}) \quad (2.64)$$

For the right leg,

$$\begin{aligned}\cos q_{22} &= \frac{x - (a + l_1 \cos q_{21})}{l_2} \\ \sin q_{22} &= \frac{y - (l_1 \sin q_{21})}{l_2}\end{aligned}$$

Finally,

$$q_{22} = \text{atan2}(\sin q_{22}, \cos q_{22}) \quad (2.65)$$

In the next section the geometry of robot is developed from the elastic perspective, thereby introducing deformation of the robot linkages.

### 2.2.2 Elastic Inverse Geometric Model

The inverse geometric model for the elastic behaviour of the system is more complex. In this model, the actuated coordinates are maintained as calculated from the rigid IGM. The elastic coordinates now come into effect and cause a displacement between the distal end of the rigid link to the deformed position of the distal end of the elastic link.

#### Floating Reference Frames

Before the elastic model can be developed, the method of floating reference frames<sup>9</sup> must be introduced. This method is readily used for the assumed mode method of elastodynamic modeling. Small deformations are assumed and the overall body motion is considered to be the superposition of a nonlinear rigid body displacement and a linear elastic displacement [22, 28] (see figure 2.5). Two sets of coordinates are used to describe the location of the distal end of the link<sup>10</sup> [2, 5, 21, 24]; the first describes the position and orientation of the rigid component of motion and the second describes the elastic deformation of the link with respect to the frame at the link base.

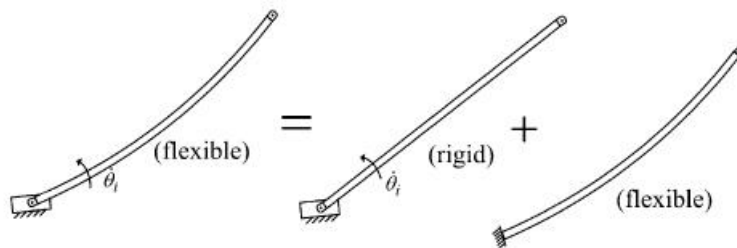


Figure 2.5: Superposition of rigid and elastic motions for clamped-free boundary conditions [28]

<sup>9</sup>Also referred to as a moving reference frame

<sup>10</sup>Furthest from the base

The transformation may be expressed as follows [2, 22]:

$${}^k\mathbf{p}_{i,j} = {}^k\mathbf{r}_{i,j} + {}^k\mathbf{u}_{i,j} \quad (2.66)$$

where

${}^k\mathbf{p}_{i,j}$  : is the  $4 \times 1$  vector coordinate of point  $i, j$  expressed in frame  $R_k$ .

${}^k\mathbf{r}_{i,j}$  : is the rigid component of  ${}^k\mathbf{p}_{i,j}$ .

${}^k\mathbf{u}_{i,j}$  : is the component of elastic displacements determined as a function of the mode shapes or eigen vectors.

The development of the inverse geometric model is done for each leg of the robot, leading to the relationships shown in 2.67. For the elastic model, the unknowns correspond to the passive joints (i.e. the dependent coordinates). For links which are not implicitly constrained the positions of each link base is included among the dependent coordinates. In figure 2.6, the deformations in  $u_{y_{ij}}$  denote deflections in bending<sup>11</sup> and deformations in  $u_{x_{ij}}$  denote deflections in tension-compression in link  $j$  of leg  $i$ .

$$\mathbf{q}_p = \left[ x_{12} \ y_{12} \ q_{12} \ x_{22} \ y_{22} \ q_{22} \ x \ y \right]^T$$

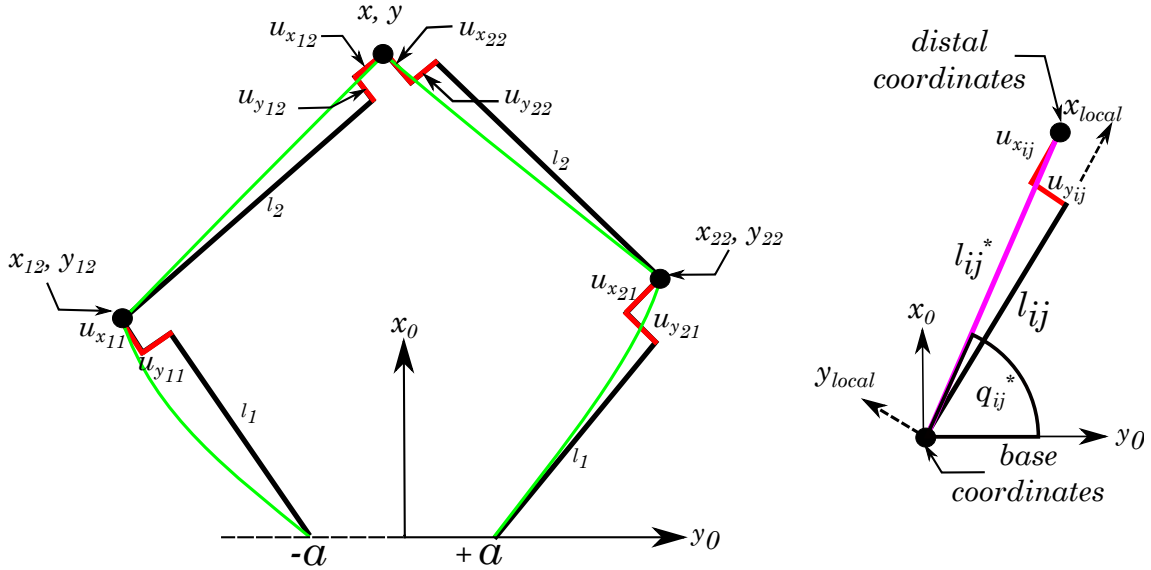


Figure 2.6: Elastic Geometric Model

The active joint variables  $q_{11}$  and  $q_{21}$  (i.e.  $\mathbf{q}_a$ ) are assumed to be perfectly rigid and are taken directly from the rigid geometric model. The elastic coordinates  $\mathbf{q}_e$  are geometrically independent from both the active and passive joints and forms part of the set of independent generalized coordinates  $\mathbf{q}_i = [\mathbf{q}_a \ \mathbf{q}_e]$ :

$$\begin{bmatrix} x \\ y \end{bmatrix} = \begin{bmatrix} x_{12} \\ y_{12} \end{bmatrix} + l_{12}^* \begin{bmatrix} \cos q_{12}^* \\ \sin q_{12}^* \end{bmatrix} = \begin{bmatrix} x_{22} \\ y_{22} \end{bmatrix} + l_{22}^* \begin{bmatrix} \cos q_{22}^* \\ \sin q_{22}^* \end{bmatrix} \quad (2.67)$$

For a general link  $l_{ij}$ , the deformed link length  $l_{ij}^*$  is expressed as follows:

$$l_{ij}^* = \sqrt{(l_i + u_{x_{ij}})^2 + u_{y_{ij}}^2}$$

$$q_{ij}^* = q_{ij} + \tan^{-1} \left( \frac{u_{y_{ij}}}{l_{ij}^*} \right)$$

<sup>11</sup>perpendicular to the beam axis

The Cartesian positions of the two passive joints are expressed as a function of the deformed link lengths and the resultant joint positions. These Cartesian positions are define the location of the base of links  $l_{12}$  and  $l_{22}$ , these positions are needed to express the state of each beam in terms of its set of generalized coordinates. For the left leg, Cartesian position of the point  $X_{12}$  is defined:

$$\boxed{\begin{bmatrix} x_{12} \\ y_{12} \end{bmatrix} = \begin{bmatrix} -a \\ 0 \end{bmatrix} + l_{11}^* \begin{bmatrix} \cos q_{11}^* \\ \sin q_{11}^* \end{bmatrix}} \quad (2.68)$$

Similarly for the right leg, the Cartesian position point  $X_{22}$  is defined:

$$\boxed{\begin{bmatrix} x_{22} \\ y_{22} \end{bmatrix} = \begin{bmatrix} a \\ 0 \end{bmatrix} + l_{21}^* \begin{bmatrix} \cos q_{21}^* \\ \sin q_{21}^* \end{bmatrix}} \quad (2.69)$$

Having obtained four of the set of 8 dependent coordinates, the angular positions of  $\mathbf{q}_{12}$  and  $\mathbf{q}_{22}$  are obtained by subtracting equation 2.68 from 2.69 as follows,

$$l_{22}^* \begin{bmatrix} \cos q_{22}^* \\ \sin q_{22}^* \end{bmatrix} = \begin{bmatrix} x_{12} - x_{22} \\ y_{12} - y_{22} \end{bmatrix} + l_{12}^* \begin{bmatrix} \cos q_{12}^* \\ \sin q_{12}^* \end{bmatrix} \quad (2.70)$$

Squaring and adding the terms in  $x$  and  $y$ :

$$l_{22}^{*2} = [(x_{12} - x_{22}) + l_{12}^* \cos q_{12}^*]^2 + [(y_{12} - y_{22}) + l_{12}^* \sin q_{12}^*]^2 \quad (2.71)$$

Replacing  $(x_{12} - x_{22})$  with  $dx$  and  $(y_{12} - y_{22})$  with  $dy$ , allows the terms to be collected and rewritten in the form:

$$dx \cos q_{12}^* + dy \sin q_{12}^* = \frac{l_{22}^* - (dx^2 + dy^2 + l_{12}^{*2})}{2l_{12}^*} \quad (2.72)$$

The above trigonometric relation is in the form  $A_e \sin \theta + B_e \cos \theta = C_e$  and is resolved as follows [15]:

$$\cos q_{12}^* = \frac{A_e C_e + \varepsilon B_e \sqrt{A_e^2 + B_e^2 - C_e^2}}{A_e^2 + B_e^2}$$

$$\sin q_{12}^* = \frac{A_e C_e - \varepsilon B_e \sqrt{A_e^2 + B_e^2 - C_e^2}}{A_e^2 + B_e^2}$$

Taking  $\varepsilon = 1$ , the solution of  $q_{12}^*$  may be found:

$$q_{12}^* = \text{atan2}(\sin q_{12}^*, \cos q_{12}^*) \quad (2.73)$$

And finally, for  $q_{12}$

$$\boxed{q_{12} = q_{12}^* - \tan^{-1} \left( \frac{u_{y12}}{l_{12}^*} \right)} \quad (2.74)$$

with

$$A_e = dx = x_{12} - x_{22} \quad (2.75)$$

$$B_e = dy = y_{12} - y_{22} \quad (2.76)$$

$$C_e = \frac{l_{22}^{*2} - (dx^2 + dy^2 - l_{12}^{*2})}{2l_{12}^*} \quad (2.77)$$

$q_{22}$  is computed next:

$$\cos q_{22}^* = \frac{A_e + l_{12}^* \cos q_{12}^*}{l_{22}^*}$$

$$\sin q_{22}^* = \frac{B_e + l_{22}^* \sin q_{12}^*}{l_{22}^*}$$

Thus,

$$q_{22}^* = \text{atan2}(\sin q_{22}^*, \cos q_{22}^*)$$

And finally for  $q_{22}$ ,

$$q_{22} = q_{22}^* - \tan^{-1} \left( \frac{u_{y22}}{l_{22}^*} \right) \quad (2.78)$$

Having found  $q_{12}$  and  $q_{22}$ , the remainder of the set of dependent coordinates, the Cartesian position of the end effector, is found:

$$\begin{bmatrix} x \\ y \end{bmatrix} = \begin{bmatrix} x_{12} \\ y_{12} \end{bmatrix} + l_{12}^* \begin{bmatrix} \cos q_{12}^* \\ \sin q_{12}^* \end{bmatrix} \quad (2.79)$$

In the next subsection, the kinematic relations relating the dependent coordinate velocities and accelerations to the independent coordinates are developed for the rigid and elastic models.

### 2.2.3 Rigid Kinematic Model

The rigid kinematic model related the end effector velocities and accelerations,  $\dot{\mathbf{X}}$  and  $\ddot{\mathbf{X}}$ , to the velocities and acceleration of the joint variables  $\dot{q}_{L_i}$  and  $\ddot{q}_{L_i}$  in each leg  $i$ .

#### Rigid Velocities

The kinematic relations are found by differentiating the geometric relations with respect to time. Deriving equation 2.58:

$$\begin{bmatrix} \dot{x} \\ \dot{y} \end{bmatrix} = \dot{q}_{11} \begin{bmatrix} -l_1 \sin q_{11} \\ l_1 \cos q_{11} \end{bmatrix} + \dot{q}_{12} \begin{bmatrix} -l_2 \sin q_{12} \\ l_2 \cos q_{12} \end{bmatrix} \quad (2.80)$$

A similar expression for the right leg is found, by differentiating equation 2.2.1. The general kinematic expression for leg  $i$  may be written as follows:

$$\underbrace{\begin{bmatrix} \dot{x} \\ \dot{y} \end{bmatrix}}_{\dot{\mathbf{x}}} = \underbrace{\begin{bmatrix} -l_1 \sin q_{i1} & -l_2 \sin q_{i2} \\ l_1 \cos q_{i1} & l_2 \cos q_{i2} \end{bmatrix}}_{\mathbf{B}_{L_i}} \underbrace{\begin{bmatrix} \dot{q}_{i1} \\ \dot{q}_{i2} \end{bmatrix}}_{\dot{\mathbf{q}}_{L_i}} \quad (2.81)$$

For the left leg,  $i = 1$ ,

$$\dot{\mathbf{q}}_{L1} = \mathbf{B}_{L1}^{-1} \dot{\mathbf{X}} \quad (2.82)$$

And for the right leg  $i = 2$ ,

$$\dot{\mathbf{q}}_{L2} = \mathbf{B}_{L2}^{-1} \dot{\mathbf{X}} \quad (2.83)$$

#### Rigid Accelerations

For the left leg the acceleration terms may be expressed as follows

$$\begin{aligned} \begin{bmatrix} \ddot{x} \\ \ddot{y} \end{bmatrix} &= \ddot{q}_{11} \begin{bmatrix} -l_1 \sin q_{11} \\ l_1 \cos q_{11} \end{bmatrix} + \dot{q}_{11}^2 \begin{bmatrix} -l_1 \cos q_{11} \\ -l_1 \sin q_{11} \end{bmatrix} \\ &+ \ddot{q}_{12} \begin{bmatrix} -l_2 \sin q_{12} \\ l_2 \cos q_{12} \end{bmatrix} + \dot{q}_{12}^2 \begin{bmatrix} -l_2 \cos q_{12} \\ -l_2 \sin q_{12} \end{bmatrix} \end{aligned} \quad (2.84)$$

Similar expressions for the left and right legs may be developed and the joint accelerations of leg  $i$ , may be written in the general form:

$$\boxed{\ddot{\mathbf{q}}_{\mathbf{L}i} = \mathbf{B}_{\mathbf{L}i}^{-1}(\mathbf{I}_{2 \times 2} \ddot{\mathbf{X}} - \dot{\mathbf{B}}_{\mathbf{L}i} \dot{\mathbf{q}}_{\mathbf{L}2})} \quad (2.85)$$

with  $\dot{\mathbf{B}}_{\mathbf{L}i}$ , being the time derivative of rigid Jacobian matrix  $\mathbf{B}_{\mathbf{L}i}$  expressed as follows:

$$\dot{\mathbf{B}}_{\mathbf{L}i} = \begin{bmatrix} -\dot{q}_{i1} l_1 \cos q_{i1} & -\dot{q}_{i2} l_2 \cos q_{i2} \\ -\dot{q}_{i1} l_1 \sin q_{i1} & -\dot{q}_{i2} l_2 \sin q_{i2} \end{bmatrix}$$

### 2.2.4 Elastic Kinematic Model

The elastic kinematic model expresses the dependent coordinate velocities and accelerations  $\dot{\mathbf{q}}_{\mathbf{d}}$  and  $\ddot{\mathbf{q}}_{\mathbf{d}}$ , in terms of the independent coordinate velocities and accelerations  $\dot{\mathbf{q}}_{\mathbf{i}}$  and  $\ddot{\mathbf{q}}_{\mathbf{i}}$ . The principle followed is similar to that of the rigid kinematics, however the floating reference frames come into effect as shown in figure 2.7.

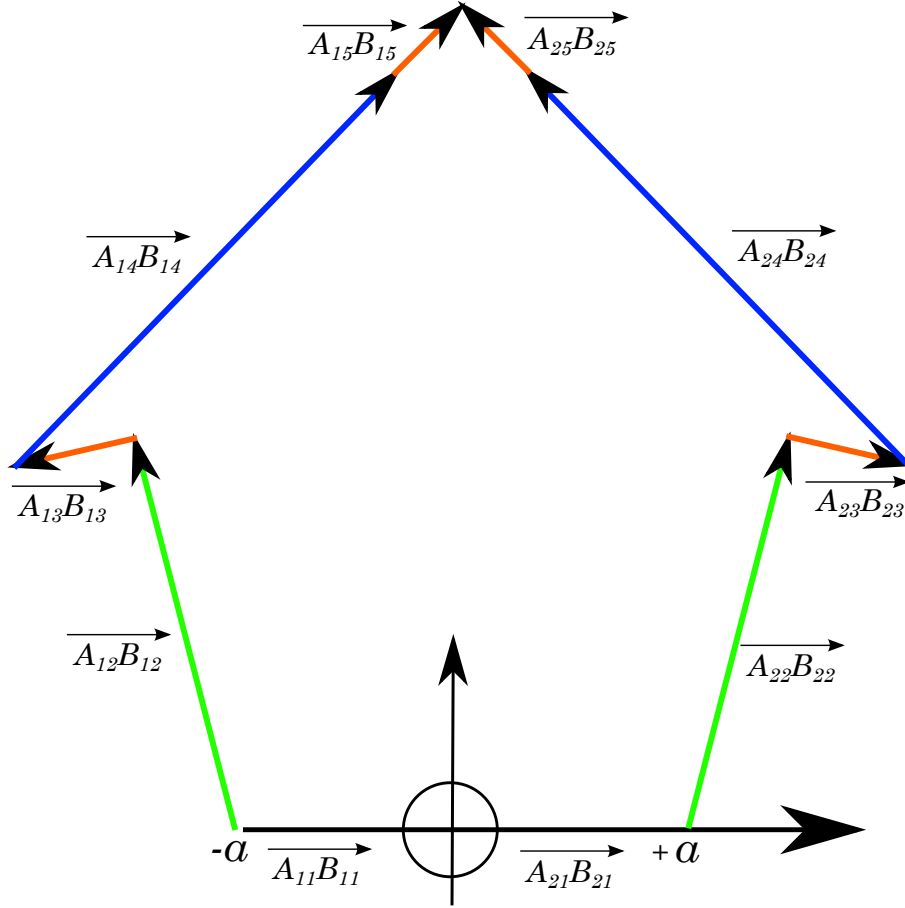


Figure 2.7: Elastic geometric model for leg  $i$

Using the vector notation shown in 2.7, the position of the passive joint located at  $\mathbf{X}_{12}$  can be developed:

$$\begin{aligned} \mathbf{X}_{12} &= \begin{bmatrix} x_{12} \\ y_{12} \end{bmatrix} = \overrightarrow{A_{11}B_{11}} + \overrightarrow{A_{12}B_{12}} + \overrightarrow{A_{13}B_{13}} \\ &= \begin{bmatrix} -a \\ 0 \end{bmatrix} + l_1 \begin{bmatrix} \cos q_{11} \\ \sin q_{11} \end{bmatrix} + \mathbf{R}(q_{11}) \begin{bmatrix} u_{x_{11}} \\ u_{y_{11}} \end{bmatrix} \end{aligned} \quad (2.86)$$

The position of the end effector  $\mathbf{X}$  may be expressed for the left leg as follows:

$$\begin{aligned} \mathbf{X} &= \begin{bmatrix} x \\ y \end{bmatrix} = \mathbf{X}_{12} + \overrightarrow{A_{14}B_{14}} + \overrightarrow{A_{15}B_{15}} \\ &= \begin{bmatrix} x_{12} \\ y_{12} \end{bmatrix} + l_2 \begin{bmatrix} \cos q_{12} \\ \sin q_{12} \end{bmatrix} + \mathbf{R}(q_{12}) \begin{bmatrix} u_{x_{12}} \\ u_{y_{12}} \end{bmatrix} \end{aligned} \quad (2.87)$$



Similarly for the right leg of the robot, the position of  $\mathbf{X}_{22}$  may be found:

$$\begin{aligned}\mathbf{X}_{22} &= \begin{bmatrix} x_{22} \\ y_{22} \end{bmatrix} = \overrightarrow{A_{21}B_{21}} + \overrightarrow{A_{22}B_{22}} + \overrightarrow{A_{23}B_{23}} \\ &= \begin{bmatrix} a \\ 0 \end{bmatrix} + l_1 \begin{bmatrix} \cos q_{21} \\ \sin q_{21} \end{bmatrix} + \mathbf{R}(q_{21}) \begin{bmatrix} u_{x_{21}} \\ u_{y_{21}} \end{bmatrix}\end{aligned}\quad (2.88)$$

Once again the position of the end effector,  $\mathbf{X}$  may be expressed in terms of the generalized coordinates associated with the right leg:

$$\begin{aligned}\mathbf{X} &= \begin{bmatrix} x \\ y \end{bmatrix} = \mathbf{X}_{22} + \overrightarrow{A_{24}B_{24}} + \overrightarrow{A_{25}B_{25}} \\ &= \begin{bmatrix} x_{22} \\ y_{22} \end{bmatrix} + l_2 \begin{bmatrix} \cos q_{22} \\ \sin q_{22} \end{bmatrix} + \mathbf{R}(q_{22}) \begin{bmatrix} u_{x_{22}} \\ u_{y_{22}} \end{bmatrix}\end{aligned}\quad (2.89)$$

### Elastic Velocities

For each leg  $i$ ; differentiation leads to the velocities of the passive joints  $\mathbf{X}_{i2}$ :

$$\dot{\mathbf{X}}_{i2} = \begin{bmatrix} \dot{x}_{i2} \\ \dot{y}_{i2} \end{bmatrix} + q_{i1} l_2 \begin{bmatrix} -\sin q_{i1} \\ \cos q_{i1} \end{bmatrix} + q_{i1} \dot{\mathbf{R}}(q_{i1}) \begin{bmatrix} u_{x_{i1}} \\ u_{y_{i1}} \end{bmatrix} + \mathbf{R}(q_{i1}) \begin{bmatrix} \dot{u}_{x_{i1}} \\ \dot{u}_{y_{i1}} \end{bmatrix}\quad (2.90)$$

The velocity of the end effector  $\dot{\mathbf{X}}$ , can be expressed in terms of the generalized coordinates of each leg  $i$ :

$$\dot{\mathbf{X}} = \begin{bmatrix} \dot{x} \\ \dot{y} \end{bmatrix} = \begin{bmatrix} \dot{x}_{i2} \\ \dot{y}_{i2} \end{bmatrix} + q_{i2} l_2 \begin{bmatrix} -\sin q_{i2} \\ \cos q_{i2} \end{bmatrix} + q_{i2} \dot{\mathbf{R}}(q_{i2}) \begin{bmatrix} u_{x_{i2}} \\ u_{y_{i2}} \end{bmatrix} + \mathbf{R}(q_{i2}) \begin{bmatrix} \dot{u}_{x_{i2}} \\ \dot{u}_{y_{i2}} \end{bmatrix}\quad (2.91)$$

With the rotation matrices defined as follows:

$$\mathbf{R}(\theta) = \begin{bmatrix} \cos \theta & -\sin \theta \\ \sin \theta & \cos \theta \end{bmatrix} \quad \dot{\mathbf{R}}(\theta) = \frac{\partial \mathbf{R}}{\partial \theta} = \begin{bmatrix} -\sin \theta & -\cos \theta \\ \cos \theta & -\sin \theta \end{bmatrix}$$

In the case of assumed modes (to be introduced in section 2.1.2), the deformation  $u_x$  and  $u_y$  are expressed in terms of the shape functions and elastic deformations:

$$u_x = \Phi_x(\xi) \mathbf{q}_{\text{ex}}(t) \quad u_y = \Phi_y(\xi) \mathbf{q}_{\text{ey}}(t)$$

And thus, in terms of velocity,

$$\dot{u}_x = \Phi_x(\xi) \dot{\mathbf{q}}_{\text{ex}}(t) \quad \dot{u}_y = \Phi_y(\xi) \dot{\mathbf{q}}_{\text{ey}}(t)$$

Setting  $\mathbf{q}_e = [\mathbf{q}_{\text{ex}}, \mathbf{q}_{\text{ey}}]^T$ , the coefficients corresponding to  $\mathbf{q}_a$ ,  $\mathbf{q}_e$  and  $\mathbf{q}_p$  may be collected in equation 2.90:

$$\begin{aligned}\begin{bmatrix} \mathbf{I} & \mathbf{0} \\ \mathbf{0} & \mathbf{I} \end{bmatrix} \begin{bmatrix} \dot{x}_{11} \\ \dot{y}_{11} \end{bmatrix} &= \begin{bmatrix} \sin q_{11} & \Phi_{y11} \\ \cos q_{11} & \Phi_{x11} \end{bmatrix} \dot{\mathbf{q}}_{\text{ey}11} \\ &+ \begin{bmatrix} -l_1 \sin q_{11} - \cos q_{11} u_{y11} \\ l_1 \cos q_{11} - \sin q_{11} u_{x11} \end{bmatrix} \dot{q}_{11}\end{aligned}$$

Also in equation 2.91:

$$\begin{aligned} \begin{bmatrix} \mathbf{I} & \mathbf{0} \\ \mathbf{0} & \mathbf{I} \end{bmatrix} \begin{bmatrix} \dot{x} \\ \dot{y} \end{bmatrix} &= \begin{bmatrix} \mathbf{I} & \mathbf{0} \\ \mathbf{0} & \mathbf{I} \end{bmatrix} \begin{bmatrix} \dot{x}_{11} \\ \dot{y}_{11} \end{bmatrix} + \begin{bmatrix} \cos q_{12} & \Phi_{x_{12}} \\ -\sin q_{12} & \Phi_{y_{12}} \end{bmatrix} \dot{q}_{\text{ex}12} \\ &+ \begin{bmatrix} -l_2 \sin q_{12} - \sin q_{12} u_{x_{11}} \\ l_2 \cos q_{12} + \cos q_{12} u_{x_{11}} \end{bmatrix} \dot{q}_{12} \end{aligned}$$

The same process may be followed for leg two. In all, 8 equations will be generated. Two corresponding to  $\dot{\mathbf{X}}_{12}$ , another two related to  $\dot{\mathbf{X}}_{22}$  and four equations (two for each leg) related to the velocity of the end effector,  $\dot{\mathbf{X}}$ . The terms may be reordered and grouped in the following form:

$$\mathbf{0} = \mathbf{A}\dot{\mathbf{q}}_p + \mathbf{B}\dot{\mathbf{q}}_e + \mathbf{C}\dot{\mathbf{q}}_a \quad (2.92)$$

The coefficient matrix associated of the passive coordinates:

$$\mathbf{A} = \begin{bmatrix} 1 & 0 & 0 & 0 & 0 & 0 & 0 & 0 & 0 \\ 0 & 1 & 0 & 0 & 0 & 0 & 0 & 0 & 0 \\ -1 & 0 & \sin q_{12} \Phi_{y_{11}} \mathbf{q}_{\text{ex}12} & 0 & 0 & 0 & 0 & 1 & 0 \\ 0 & -1 & -\cos q_{12} \Phi_{y_{11}} \mathbf{q}_{\text{ex}12} & 0 & 0 & 0 & 0 & 0 & 1 \\ 0 & 0 & 0 & 1 & 0 & 0 & 0 & 0 & 0 \\ 0 & 0 & 0 & 0 & 1 & 0 & 0 & 0 & 0 \\ 0 & 0 & 0 & -1 & 0 & \sin q_{22} \Phi_{y_{22}} \mathbf{q}_{\text{ex}22} & 1 & 0 & 0 \\ 0 & 0 & 0 & 0 & -1 & -\cos q_{22} \Phi_{y_{22}} \mathbf{q}_{\text{ex}22} & 0 & 1 & 0 \end{bmatrix} \quad (2.93)$$

The advantage of this formulation is that  $\mathbf{A}$  is square and is thus invertible. The coefficient matrix for the elastic coordinates is given by:

$$\mathbf{B} = \begin{bmatrix} -\sin q_{11} \Phi_{y_{11}} & \mathbf{0} & \mathbf{0} & \mathbf{0} \\ -\cos q_{11} \Phi_{y_{11}} & \mathbf{0} & \mathbf{0} & \mathbf{0} \\ \mathbf{0} & -\cos q_{12} \Phi_{y_{12}} & \mathbf{0} & \mathbf{0} \\ \mathbf{0} & \sin q_{12} \Phi_{y_{12}} & \mathbf{0} & \mathbf{0} \\ \mathbf{0} & \mathbf{0} & -\sin q_{21} \Phi_{y_{21}} & \mathbf{0} \\ \mathbf{0} & \mathbf{0} & -\cos q_{21} \Phi_{y_{21}} & \mathbf{0} \\ \mathbf{0} & \mathbf{0} & \mathbf{0} & -\cos q_{22} \Phi_{y_{22}} \\ \mathbf{0} & \mathbf{0} & \mathbf{0} & \sin q_{22} \Phi_{y_{22}} \end{bmatrix} \quad (2.94)$$

And finally the coefficient matrix of the actuated coordinates is expressed as follows:

$$\mathbf{C} = \begin{bmatrix} l_1 \sin q_{11} + \cos q_{11} \Phi_{y_{11}} \mathbf{q}_{\text{ey}11} & 0 \\ -l_1 \cos q_{11} + \sin q_{11} \Phi_{y_{11}} \mathbf{q}_{\text{ey}11} & 0 \\ 0 & 0 \\ 0 & 0 \\ 0 & l_1 \sin q_{21} + \cos q_{21} \Phi_{y_{21}} \mathbf{q}_{\text{ey}21} \\ 0 & -l_1 \cos q_{21} + \sin q_{21} \Phi_{y_{21}} \mathbf{q}_{\text{ey}21} \\ 0 & 0 \\ 0 & 0 \end{bmatrix} \quad (2.95)$$

The passive coordinate velocities are obtained from:

$$\dot{\mathbf{q}}_{\mathbf{p}} = -\mathbf{A}^{-1} (\mathbf{B}\dot{\mathbf{q}}_{\mathbf{e}} + \mathbf{C}\dot{\mathbf{q}}_{\mathbf{a}}) \quad (2.96)$$

### Elastic Accelerations

The accelerations are found by differentiating equation 2.92 with respect to time:

$$\mathbf{0} = \mathbf{A}\ddot{\mathbf{q}}_{\mathbf{p}} + \mathbf{B}\ddot{\mathbf{q}}_{\mathbf{e}} + \mathbf{C}\ddot{\mathbf{q}}_{\mathbf{a}} + \dot{\mathbf{A}}\dot{\mathbf{q}}_{\mathbf{p}}^2 + \dot{\mathbf{B}}\dot{\mathbf{q}}_{\mathbf{e}}^2 + \dot{\mathbf{C}}\dot{\mathbf{q}}_{\mathbf{a}}^2$$

The passive coordinate accelerations are calculated:

$$\ddot{\mathbf{q}}_{\mathbf{p}} = -\mathbf{A}^{-1} (\mathbf{B}\ddot{\mathbf{q}}_{\mathbf{e}} + \mathbf{C}\ddot{\mathbf{q}}_{\mathbf{a}} + \dot{\mathbf{A}}\dot{\mathbf{q}}_{\mathbf{p}}^2 + \dot{\mathbf{B}}\dot{\mathbf{q}}_{\mathbf{e}}^2 + \dot{\mathbf{C}}\dot{\mathbf{q}}_{\mathbf{a}}^2) \quad (2.97)$$

with

$$\dot{\mathbf{A}} = \frac{\partial \mathbf{A}}{\partial \mathbf{q}} \quad \dot{\mathbf{B}} = \frac{\partial \mathbf{B}}{\partial \mathbf{q}} \quad \dot{\mathbf{C}} = \frac{\partial \mathbf{C}}{\partial \mathbf{q}}$$

In the next section, the dynamics of the system are derived from first principles. The dynamic models involve the development of the inertial matrices, stiffness matrices, Coriolis and gravity vectors for each link. These elements are synthesized in such a way that the closed loop dynamics of the system may be modeled.

## 2.3 Model Verification

Understanding the behaviour of a robot with respect to its vibratory characteristics is essential to the verification of its theoretical elastodynamic model, also serving to the development of appropriate controllers. The frequency analysis of a robot modeled with floating reference frames entails a reordering and reworking of the robot mass matrix.

The natural frequencies and mode shapes of the robot in a given configuration can be found by solving for the eigenvalues,  $\omega_n^2$ , and eigenvectors  $\mathbf{u}$  in [12, 21]:

$$\left(\mathbf{K} - \omega_n^2 \mathbf{M}_{\text{freq}}\right) \mathbf{u} = 0 \quad (2.98)$$

where

$\mathbf{K}$  : Is the  $n_e \times n_e$ <sup>12</sup> stiffness matrix of the system

$\mathbf{M}_{\text{freq}}$  : Is the  $n_e \times n_e$  modified inertia matrix of the system

### 2.3.1 Modified Inertia Matrix

The unmodified inertia matrix,  $\mathbf{M}$ , based on the set of generalized coordinates, may be reordered according to the independent  $\mathbf{q}_i = [\mathbf{q}_a, \mathbf{q}_e]$ , and dependent coordinates  $\mathbf{q}_d = \mathbf{q}_p$ , as seen earlier:

$$\mathbf{M} = \begin{bmatrix} \mathbf{M}_{aa} & \mathbf{M}_{ae} & \mathbf{M}_{ap} \\ \mathbf{M}_{ea} & \mathbf{M}_{ee} & \mathbf{M}_{ep} \\ \mathbf{M}_{pa} & \mathbf{M}_{pe} & \mathbf{M}_{pp} \end{bmatrix} \quad (2.99)$$

In the above matrix, the following principle dimensioning applies:

- $\mathbf{M}_{aa}$  is a  $n_a \times n_a$ <sup>13</sup> matrix
- $\mathbf{M}_{ee}$  is a  $n_e \times n_e$  matrix
- $\mathbf{M}_{pp}$  is a  $n_p \times n_p$ <sup>14</sup> matrix

The modification of the inertia matrix  $\mathbf{M}$ , leads to the reduced matrix,  $\mathbf{M}_{\text{freq}}$ , required in equation 2.3. Two sets of equations are required to modify the inertia matrix. Firstly, the expression of the system's kinetic energy 2.2, is evaluated assuming  $\dot{\mathbf{q}}_a = \mathbf{0}$ . Secondly, the kinematic relations of the system are used to express the passive coordinate velocities  $\dot{\mathbf{q}}_p$  in terms of the elastic coordinate velocities  $\dot{\mathbf{q}}_e$ .

As the resonance frequency of the robot is to be determined in a fixed position, the kinetic energy of the system may be developed to obtain the corresponding reduced inertia matrix. Taking  $\dot{\mathbf{q}}_a = \mathbf{0}$ , the kinetic energy is expressed as follows:

$$E = \frac{1}{2} \begin{bmatrix} \mathbf{0}^T & \dot{\mathbf{q}}_e^T & \dot{\mathbf{q}}_p^T \end{bmatrix} \begin{bmatrix} \mathbf{M}_{aa} & \mathbf{M}_{ae} & \mathbf{M}_{ap} \\ \mathbf{M}_{ea} & \mathbf{M}_{ee} & \mathbf{M}_{ep} \\ \mathbf{M}_{pa} & \mathbf{M}_{pe} & \mathbf{M}_{pp} \end{bmatrix} \begin{bmatrix} \mathbf{0} \\ \dot{\mathbf{q}}_e \\ \dot{\mathbf{q}}_p \end{bmatrix} \quad (2.100)$$

Using the kinematic relations,

$$\mathbf{A}\dot{\mathbf{q}}_p + \mathbf{B}\dot{\mathbf{q}}_e + \mathbf{C}\dot{\mathbf{q}}_a = 0 \quad (2.101)$$

<sup>12</sup> $n_e$  is the number of elastic coordinates in the system

<sup>13</sup> $n_a$  is the number of actuated coordinates in the system

<sup>14</sup> $n_p$  is the number of passive coordinates in the system

Substitution of  $\dot{\mathbf{q}}_a = \mathbf{0}$ , allows  $\dot{\mathbf{q}}_p$  to be defined in terms of  $\dot{\mathbf{q}}_e$ :

$$\dot{\mathbf{q}}_p = -\mathbf{A}^{-1}\mathbf{B}\dot{\mathbf{q}}_e = \mathbf{J}_e\dot{\mathbf{q}}_e \quad (2.102)$$

Substituting 2.102 into 2.100, the kinetic energy of the system may be rewritten in the form:

$$E = \frac{1}{2}\dot{\mathbf{q}}_e^T \mathbf{M}_{\text{freq}} \dot{\mathbf{q}}_e \quad (2.103)$$

Where,

$$\mathbf{M}_{\text{freq}} = \mathbf{M}_{ee} + \mathbf{J}_e^T \mathbf{M}_{pe} + \mathbf{M}_{ep} \mathbf{J}_e + \mathbf{J}_e^T \mathbf{M}_{pp} \mathbf{J}_e \quad (2.104)$$

### 2.3.2 Frequency Analysis

The natural frequencies were investigated at several robot configurations (figure 2.8). To compare the results, a finite element model was built in CASTEM. The results obtained from the theoretical Assumed Modes Model (AMM) and the Finite Element Analysis (FEA) are compared in table 2.3.

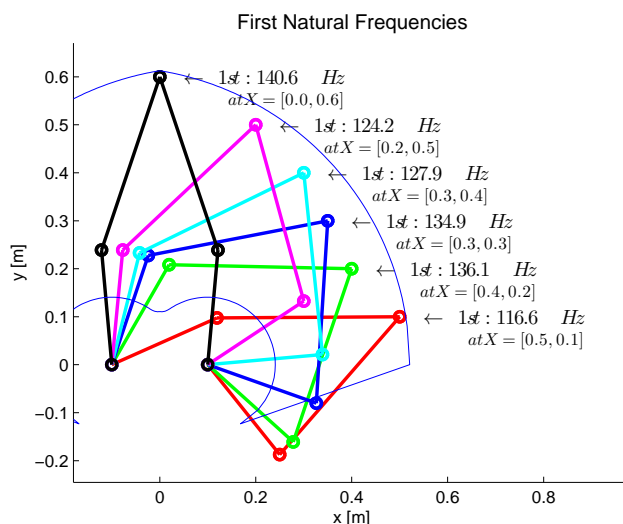


Figure 2.8: Configurations for natural frequency verification

The CASTEM model uses simple beam elements to model the five bar mechanism. Each link is modeled with 8 elements. The actuated coordinates are considered to be fixed and are treated as cantilevered beams. The nodes corresponding to the passive coordinates are free, and establish pinned connections for two un-actuated links. The first three modes of the actuated beams can be seen in figure 2.9.

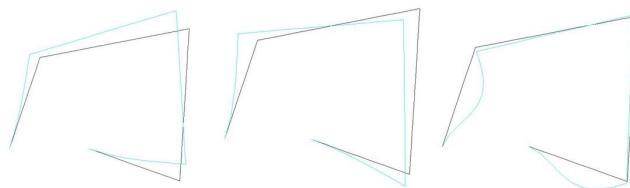


Figure 2.9: The first three modes shapes as per CASTEM at position [0.35, 0.3]

As the modeling techniques are inherently different [6], it was found that the third natural frequency in the AMM, corresponds to the 5<sup>th</sup> or 6<sup>th</sup> mode in the FEA. This discrepancy is due to the fact that the FEA model allows the bending of the two distal links, whereas the AMM assigns a traction-compression modal series to these two links. This property is both the advantage and disadvantage of the assumed modes method. Unless the structure is well understood, important structural behaviours may be overlooked. Nevertheless, it can be seen that the results are satisfactory, with the first and second natural frequencies being accurate within, at worst, a 3.126% accuracy. As expected, the third natural frequency shows some deviation, with an error of up to 8.563% at the [0.2, 0.5] end effector position.

Effector Position	1 <sup>st</sup> Natural Frequency [Hz]			2 <sup>nd</sup> Natural Frequency [Hz]			3 <sup>rd</sup> Natural Frequency [Hz]		
	AMM	FEA	%Error	AMM	FEA	%Error	AMM	FEA <sub>15</sub>	%Error
[0.5, 0.1]	116.61	115.32	1.119	210.68	206.51	2.019	1877.3	1879.5	0.117
[0.4, 0.2]	136.13	134.59	1.144	157.27	156.19	0.691	1921.1	1833.4	4.783
[0.35, 0.3]	134.85	133.42	1.072	156.07	153.03	1.987	1923.2	1833.7	4.881
[0.3, 0.4]	127.86	126.42	1.139	168.02	166.93	0.653	1917.2	1806.2	6.145
[0.2, 0.5]	124.2	122.51	1.379	183.25	182.06	0.654	1908.1	1757.6	8.563
[0.0, 0.6]	140.64	136.41	3.101	226.67	219.80	3.126	1775.4	1890.2	6.073

Table 2.3: Natural Frequencies at Various Robot Configurations

In the case of a planar five bar mechanism, the links are pin connected and the bending modes are not excited as they are only exposed to tensile and compressive forces, giving support to the approach taken in the AMM. To incorporate this assumption in the FEA, the second moment of inertia of the distal links were increased by a factor of 5. This increase in inertia, effectively allows the third natural frequency of the FEA to coincide with the AMM (table 2.4), and drastically reduces the percentage error.

Effector Position	3 <sup>rd</sup> Natural Frequency [Hz]		
	AMM	FEA	%Error
[0.5, 0.1]	1877.3	1874.3	0.160
[0.4, 0.2]	1921.1	1916.8	0.224
[0.35, 0.3]	1923.2	1917.9	0.276
[0.3, 0.4]	1917.2	1914.9	0.120
[0.2, 0.5]	1908.1	1906.1	0.105
[0.0, 0.6]	1775.4	1710.3	3.806

Table 2.4: Third natural frequency with adjusted inertia in the FEA

In their study on the vibrational performance of parallel robots, Piras et al [21], perform a frequency analysis of a region in the workspace of a 3-PRR robot, a similar study is performed here, the frequency distribution for the first three natural frequencies are shown in figures 2.10, 2.11 and 2.12. The workspace boundaries correspond to the type I (serial singularities) present in this robotic structure. The relative sizing of the links do not allow a type II (parallel singularity) to be obtained in the workspace.

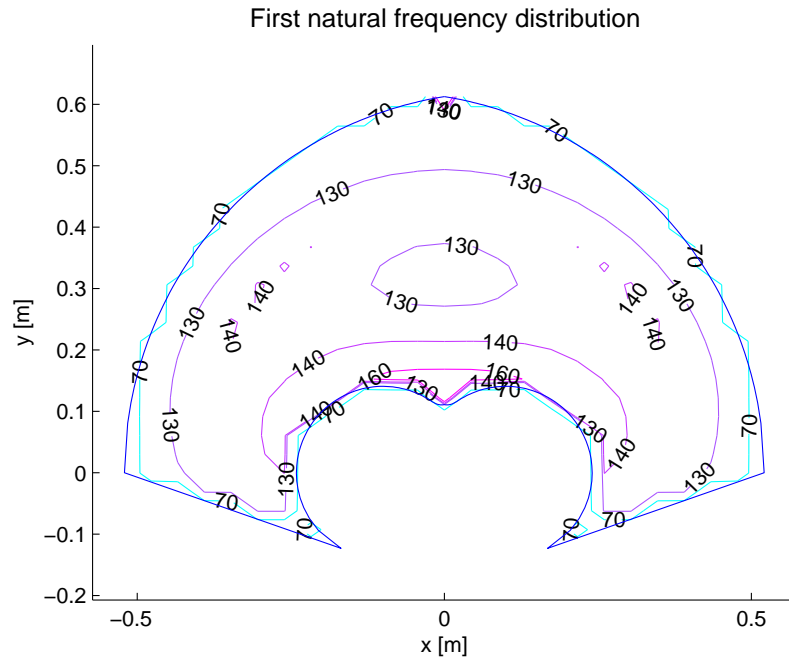


Figure 2.10: Contour plot of first natural frequency in workspace

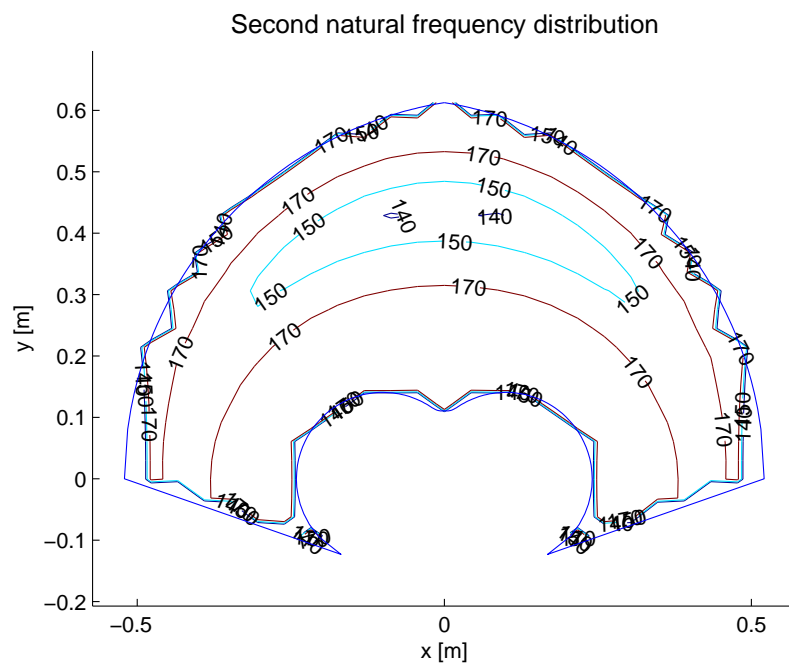


Figure 2.11: Contour plot of second natural frequency in workspace





### Tool Mass Effects

The previous studies did not incorporate the mass of the effector tool or payload. This mass greatly affects the structural resonances of the robot by altering the natural frequencies. This is to say that the structural resonance of the robot is a function of its configuration *and* its loading condition. The effect of the tool mass  $m_{tool}$ , is investigated for the following cases:  $0kg$ ,  $1kg$ ,  $10kg$  and  $100kg$ , see figure 2.13:

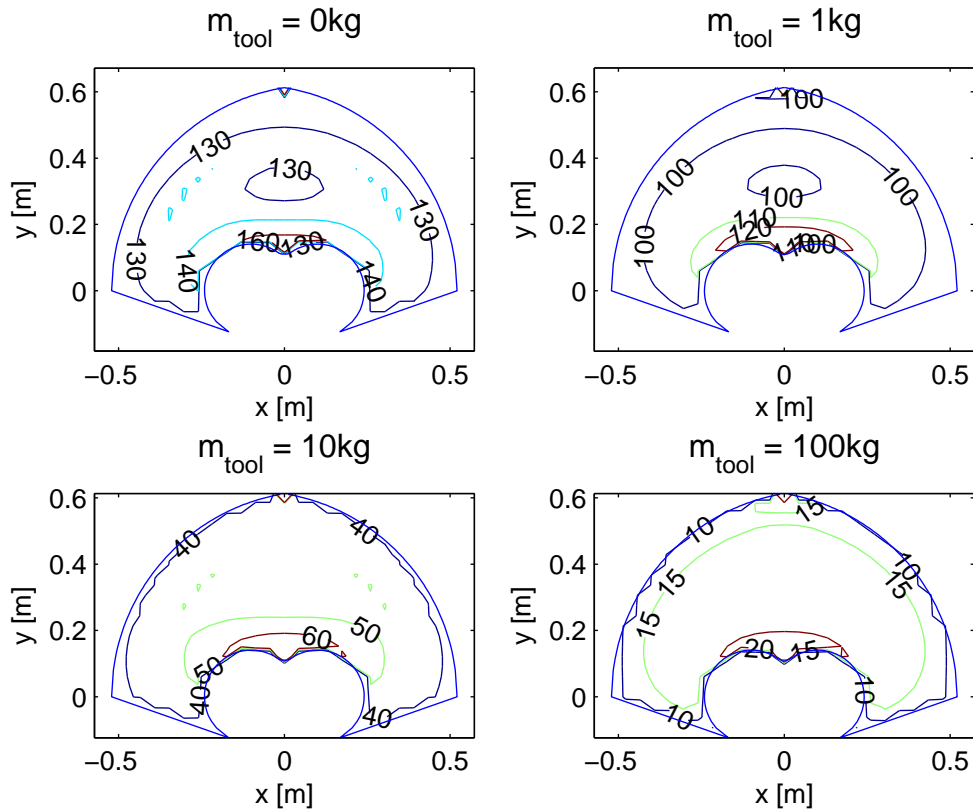


Figure 2.13: *First natural frequency in workspace as a function of tool mass*

It can be seen that increasing the mass of the tool decreases the resonance frequencies. The major frequencies in the workspace are  $130Hz$ ,  $100Hz$ ,  $40Hz$  and  $15Hz$  respectively. The effect of payload on the robot would be similar, it may at this point be anticipated that the control strategies for the robot should be adapted to instances with and without payload.

### 2.3.3 Deformation Analysis

To verify the accuracy of the stiffness matrix, the deformation of the robotic structure is investigated under certain loading conditions. The end effector is placed at the positions shown in figure 2.14. A comparison between the deformations predicted in the AMM and the FEA are presented in tables 2.5 and 2.6.

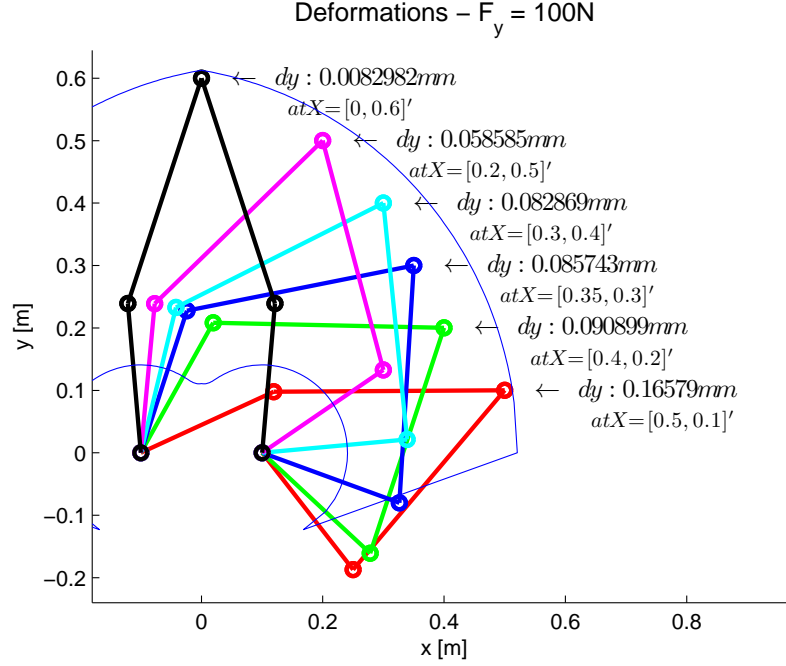


Figure 2.14: Configurations for deformation verification

Static deformations on the structure may be calculated from evaluating the static equilibrium of the robot. As the robot is assumed to be at rest,  $\dot{\mathbf{q}}$  and  $\ddot{\mathbf{q}}$  are taken as  $\mathbf{0}$ :

$$\begin{bmatrix} \mathbf{I} & \mathbf{0} & \mathbf{C}_{n_a \times n_p}^T \\ \mathbf{0} & \mathbf{I} & \mathbf{B}_{n_e \times n_p}^T \\ \mathbf{0} & \mathbf{0} & \mathbf{A}_{n_p \times n_p}^T \end{bmatrix} \begin{bmatrix} \tau_a \\ \tau_e \\ \lambda \end{bmatrix} + \begin{bmatrix} \mathbf{0}_{n_a \times 1} \\ \mathbf{0}_{n_e \times 1} \\ \mathbf{F}_{\text{load}_{n_p \times 1}} \end{bmatrix} = \mathbf{0} \quad (2.105)$$

Gravitational effects owing to the mass of the links and the tool are ignored and the observed deformations are only due to the applied load. Solving for  $\lambda$ :

$$\lambda = -\mathbf{A}^{T^{-1}} \mathbf{F}_{\text{load}} \quad (2.106)$$

Solving for  $\tau_e$ :

$$\tau_e + \mathbf{B}^T \lambda = 0 \quad (2.107)$$

$$\tau_e = \mathbf{B}^T \mathbf{A}^{T^{-1}} \mathbf{F}_{\text{load}} = -\mathbf{J}_e \mathbf{F}_{\text{load}}$$

Based on Hooks Law, the following applies  $\tau_e = \mathbf{K} \mathbf{q}_e$ , therefore:

$$\mathbf{q}_e = \mathbf{K}^{-1} \tau_e \quad (2.108)$$

The results in tables 2.5 and 2.6 show very good accuracy. Poorer accuracy is however observed at positions [0.5, 0.1] and [0.0, 0.6]. These two configurations are closer to the singular positions, giving rise to poorer conditioning of the Jacobian matrices. It is notable that the structure becomes less stiff at these positions.

Effector Position	$F_x = 100N$				
$[X, Y]$	$x - y$ AMM [ $\mu m$ ]		$x - y$ FEA [ $\mu m$ ]		%Error
[0.5, 0.1]	15.082	-14.053	15.441	-14.366	2.323
[0.4, 0.2]	68.452	-21.306	68.6531	-21.362	0.293
[0.35, 0.3]	75.714	-21.099	75.935	-21.130	0.291
[0.3, 0.4]	79.073	-34.036	79.374	-34.061	0.379
[0.2, 0.5]	95.935	-39.097	96.3735	-39.112	0.455
[0.0, 0.6]	73.49	0.00277	75.236	7E-12	2.321

Table 2.5: Deformation under  $F_x = 100N$ 

Effector Position	$F_y = 100N$				
$[X, Y]$	$x - y$ AMM [ $\mu m$ ]		$x - y$ FEA [ $\mu m$ ]		%Error
[0.5, 0.1]	-14.077	165.79	-14.366	166.347	0.347
[0.4, 0.2]	-21.283	90.899	-21.362	91.15	0.280
[0.35, 0.3]	-21.077	85.745	-21.130	85.924	0.211
[0.3, 0.4]	-34.028	82.869	-34.061	83.012	0.161
[0.2, 0.5]	-39.1	58.585	-39.112	58.736	0.187
[0.0, 0.6]	0.00039	8.2982	0.0653	8.4985	2.360

Table 2.6: Deformation under  $F_y = 100N$ 

In the next chapter various pick and place trajectories are developed and discussed. The trajectories are compared and contrasted, and the frequency content is presented.

## Chapter 3

# Trajectory Design

Pick-and-place tasks are commonly performed by industrial robots responsible for packing and assembly operations [8, 10]. The procedure transfers an object from one workplace to another [10]. The scope of this report is limited to the study of pick-and-place paths followed in a two dimensional, planar space. The movement shown in figure 3.1 may nominally be achieved with a 2DOF robot. This standardized geometric path is referred to as the Adept cycle and has dimensions of  $h = 25mm$  and  $l = 350mm$  [13].

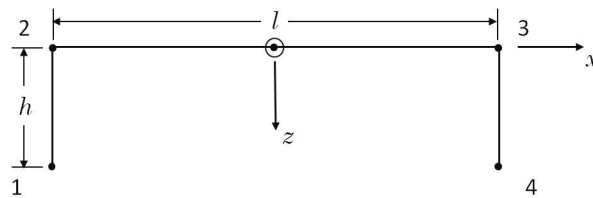


Figure 3.1: *Pick-and-place trajectory.*

The standard adept cycle, shown in 3.1 has square corners, and introduce discontinuity in acceleration when traversed. To overcome these discontinuities extremely high torques must be generated at the actuators, this, coupled with the inertial effect of the moving system, give rise to unwanted vibrations. To avoid these discontinuities the adept cycle is made smooth by introducing blends at the corners [8].

The rate at which the geometric path is followed is also a source of vibration. The motion profile, governing the traversal of the path, must be well chosen and designed to minimize excitation of resonances in the structure. The sampling of the geometric path as determined by the motion profile gives rise to the trajectory. This chapter first introduces some geometric paths, followed by the presentation of typical motion profiles. Finally, the resultant trajectories will be compared and discussed.

### 3.1 Geometric Path

In this section various geometric curves will be introduced for blending purposes. The following curves will be seen:

- Clothoid Curves
- Lamé Curves
- Polar Polynomials

Gauthier et al.[8] propose the blending dimensions shown in figure 3.2 to optimize the energy consumed by a SCARA robot performing pick and place tasks. In the image,  $d$  corresponds to the vertical blending length, and  $e$  to the horizontal blending length of a corner.

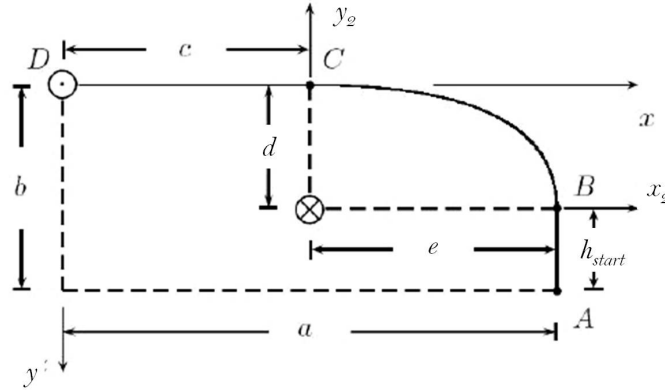


Figure 3.2: Adept half cycle using a Lamé curve [8]

#### 3.1.1 Clothoids

Clothoids curves are discussed in great detail in path planning for autonomous vehicle literature. These curves are the time optimal solution for given constraints in jerk[14]. Clothoid curves are defined within the Cartesian frame as follows:

$$x(\theta) = aC(\theta) \qquad y(\theta) = aS(\theta) \qquad (3.1)$$

Where  $a$  is the clothoid sharpness and  $C(\theta)$  and  $S(\theta)$  are the Fresnel Integrals:

$$C(\theta) = \frac{1}{\sqrt{2\pi}} \int_0^\theta \frac{\cos u}{\sqrt{u}} du \qquad S(\theta) = \frac{1}{\sqrt{2\pi}} \int_0^\theta \frac{\sin u}{\sqrt{u}} du \qquad (3.2)$$

A clothoid curve is characterized by the curvature function [27]:

$$\kappa(\theta) = \frac{d\theta(s)}{ds} = \frac{\sqrt{2\pi\theta}}{a}$$

Kanayama and Miyake, [14] show that the Cartesian coordinates of a curve may be derived from its curvature function as follows:

$$\begin{aligned} x(s) &= \int_0^s \cos \left[ \theta_0 + \int_0^t \kappa(\theta) d\theta \right] dt \\ y(s) &= \int_0^s \sin \left[ \theta_0 + \int_0^t \kappa(\theta) d\theta \right] dt \end{aligned} \qquad (3.3)$$

Skeleton ray diagrams are used to constrain the blending of two consecutive straight line segments. Clothoids are used in pairs and may be used to perform symmetric or un-symmetric blending. Each clothoid segment,  $i$ , is integrated from 0 to  $\theta_i$  to find the resultant curve in Cartesian coordinates.

### Symmetric Blending

In symmetric blending the rays forming the skeleton diagram have equal lengths and the generated blend consists of two clothoids with equal sharpness,  $a$ . The relative angle between the two rays  $\alpha$  is known as well as the length of each ray  $d$ . The two clothoids meet at  $\mathbf{P}$ . From inspection one can see that the blending occurs between  $0$  and  $\frac{\alpha}{2}$  (figure 3.3).

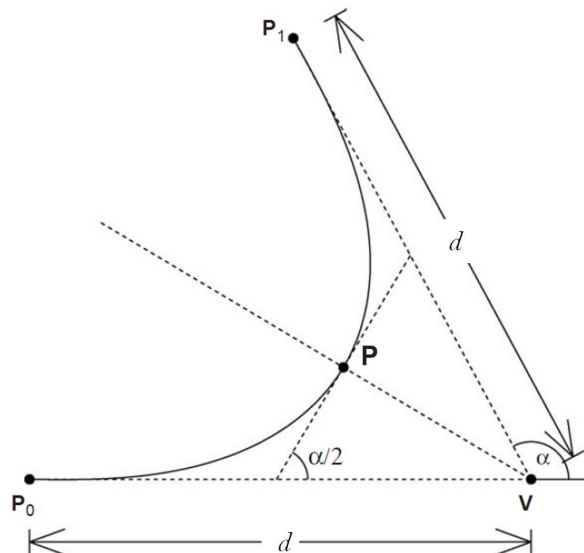


Figure 3.3: *Symmetric blending ray diagram* [27]

The relative angle  $\alpha$  and the length of each ray are related by:

$$\underbrace{aC\left(\frac{\alpha}{2}\right)}_x + \underbrace{aS\left(\frac{\alpha}{2}\right)}_y \tan \frac{\alpha}{2} = d$$

The clothoid sharpness,  $a$ , can thus be found:

$$a = \frac{d}{C\left(\frac{\alpha}{2}\right) + S\left(\frac{\alpha}{2}\right) \tan \frac{\alpha}{2}} \quad (3.4)$$

### Un-symmetric Blending

In un-symmetric blending, the ray lengths  $d$  and  $e$  are not equal (see figure 3.4). The blending curve is generated by two clothoids  $A_0$  and  $A_1$  with associated parameters  $a_0$ ,  $\theta_0$  and  $a_1$  and  $\theta_1$  respectively. As clothoid curvature is linear with respect to the inverse sharpness  $\frac{1}{a}$ , certain restrictions to blending apply [27].

Defining,

$$k = \frac{d}{e} > 1$$

$$\text{First Condition: } \frac{k + \cos \alpha}{\sin \alpha} < \frac{C(\alpha)}{S(\alpha)} \quad (3.5)$$

Satisfying 3.5 allows the blending of clothoids  $A_0$  and  $A_1$  generated from  $\mathbf{P}_0$  to  $\mathbf{P}$ , and from  $\mathbf{P}_1$  to  $\mathbf{P}$  respectively. The two clothoids meet at point  $\mathbf{P}$  with the same unsigned curvature<sup>1</sup>.

A second condition is necessary to ensure that the normal vectors of  $A_0$  and  $A_1$  coincide with the normal vectors at  $\mathbf{P}_0$  and  $\mathbf{P}_1$ :

<sup>1</sup>This means that the tangent vectors  $\mathbf{T}_0$  and  $\mathbf{T}_1$  are equal but in opposite direction

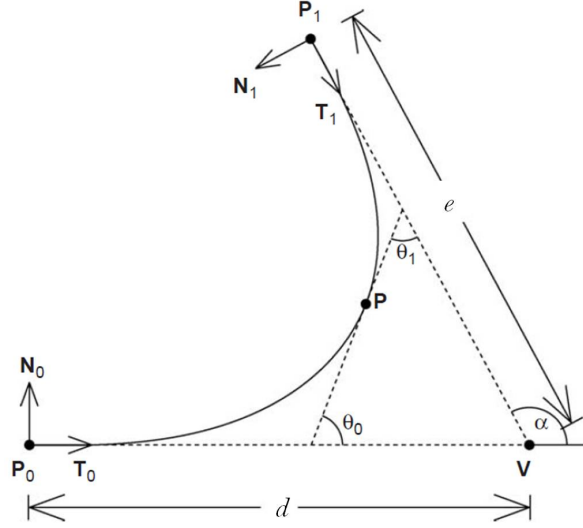


Figure 3.4: Un-symmetric blending ray diagram [27]

$$\text{Second Condition: } \frac{k + \cos \alpha}{k \sin \alpha} < \frac{C(\alpha)}{S(\alpha)} \quad (3.6)$$

Having met both conditions, it is possible to find the two clothoids  $A_0$  and  $A_1$  which generate two curve segments satisfying:

$$\mathbf{P} = \mathbf{P}_0 + a_0 C(\theta_0) \mathbf{T}_0 + a_0 S(\theta_0) \mathbf{N}_0 \quad (3.7)$$

$$\mathbf{P} = \mathbf{P}_1 + a_1 C(\theta_1) \mathbf{T}_1 + a_1 S(\theta_1) \mathbf{N}_1 \quad (3.8)$$

For a given set of  $g$ ,  $h$  and  $\alpha$ , and using the relations,

$$a_1 = a_0 \sqrt{\frac{\theta_1}{\theta_0}} \quad \theta_1 = \alpha - \theta_0$$

The clothoid sharpnesses,  $a_0$  and  $a_1$ , can be found by expressing the projection of  $\mathbf{P}$  onto each of the rays:

$$\begin{aligned} d + e \cos \alpha &= a_0 C(\theta_0) - a_1 C(\theta_1) \sin\left(\frac{\pi}{2} - \alpha\right) + a_1 S(\theta_1) \sin \alpha \\ &= a_0 C(\theta_0) + a_0 \sqrt{\frac{\alpha - \theta_0}{\theta_0}} C(\alpha - \theta_0) \cos \alpha + a_0 \sqrt{\frac{\alpha - \theta_0}{\theta_0}} S(\alpha - \theta_0) \sin \alpha \end{aligned} \quad (3.9)$$

Similarly:

$$e \sin \alpha = a_0 S(\theta_0) + a_0 \sqrt{\frac{\alpha - \theta_0}{\theta_0}} C(\alpha - \theta_0) \sin \alpha + a_0 \sqrt{\frac{\alpha - \theta_0}{\theta_0}} S(\alpha - \theta_0) \sin \alpha \quad (3.10)$$

Solving for  $a_0$  in equations 3.9 and 3.10, and after some algebraic manipulation:

$$f(\theta) = \sqrt{\theta} [C(\theta) \sin \alpha - S(\theta)(k + \cos \alpha)] + \sqrt{\alpha - \theta} [S(\alpha - \theta)(1 + k \cos \alpha) - kC(\alpha - \theta) \sin \alpha] \quad (3.11)$$

The zeros of  $f$  must be found to obtain the solution for  $\theta_0$ . Walton and Meek, [27], propose a numerical technique such bisection or Newton's method once the derivative of  $f$  is obtained. In the computational environment the *fmincon* Matlab function was used, a non-linear equality constraint was used to set  $f(\theta) = 0$ . One notes that with the constraints in equations 3.5 and 3.6, for a given  $\alpha$ , there exists a limit to the ray length ratio  $k$ .

### Ray length ratio limits

The ray length ratio limits are obtained by changing the inequalities of equations 3.5 and 3.6 to equalities. For the first condition:

$$\frac{k^* + \cos \alpha}{\sin \alpha} = \frac{C(\alpha)}{S(\alpha)}$$

thus,

$$\boxed{k^* = \frac{C(\alpha)}{S(\alpha)} \sin(\alpha) - \cos(\alpha)} \quad (3.12)$$

For the second,

$$\frac{k^* + \cos \alpha}{k^* \sin \alpha} = \frac{C(\alpha)}{S(\alpha)}$$

thus,

$$\boxed{k^* = \frac{\cos(\alpha)}{\frac{C(\alpha)}{S(\alpha)} \sin(\alpha) - 1}} \quad (3.13)$$

The clothoid pairs are to be introduced at the corners of the adept cycle, this means that  $\alpha = \frac{\pi}{2}$ . The first condition is invoked if the ray along the vertical axis is longer than the one along the horizontal, while the opposite is true for the second condition. The aspect ratio of the adept cycle is such that the second condition would provide the maximum length  $e$ . If the vertical ray is chosen as  $d = h = 25\text{mm}$ , we can find  $e = 44.5$ , the resultant clothoid pair is compared to the Lamé curve with the same dimensions in figure 3.6.

### 3.1.2 Lamé Curves

Gauthier, Angeles and Nokleby [8] choose Lamé curves to define the transitional section of curve  $BC$  (figure 3.2) because it allows a parametrization in Cartesian coordinates and is analytic throughout the required path as it is limited to the first quadrant. With respect to figure 3.2, the normalized Lamé curve may be defined as:

$$|u|^m + |v|^m = 1 \quad (3.14)$$

The normalizing relationships are,  $u = \frac{x_2}{d}$  and  $v = \frac{z_2}{e}$ , where  $d$  and  $e$  refer to the half lengths of the curve axes. The indice  $m$  is the degree of the curve. For  $m = 2$  the Lamé curve represents a circle, as  $m \rightarrow \infty$  the curve approaches a square shape.

It was chosen to design the corner blend with the lowest order Lamé curve with a differentiable curvature. For this  $m = 3$  is needed, generating a cubic Lamé curve. Transforming to polar coordinates with  $\phi \in [0, \pi/2]$ , the Cartesian coordinates,  $x$  and  $y$ , may be defined as a functions:

$$x(\phi) = \frac{d}{(1 + \tan^3 \phi)^{1/3}} \quad (3.15)$$

$$y(\phi) = \frac{e \tan \phi}{(1 + \tan^3 \phi)^{1/3}} \quad (3.16)$$

Note that the ray lengths given by  $d$  and  $e$  can be scaled independently, allowing a greater degree of blending with the Lamé curve than with a clothoid pair.

### 3.1.3 Polar Polynomials

Polar polynomials are expressed with closed form equations and represent the simplest blending approach. By defining the junction points  $d$  and  $e$ , specifying a turning angle  $\sigma$  and identifying appropriate boundary conditions, polar polynomials in the form given in 3.17 may be found.

$$\rho(\phi) = a_0 + a_1\phi + a_2\phi^2 + a_3\phi^3 + a_4\phi^4 \dots \quad (3.17)$$



Segovia et al [23] define the following simple curve for  $\alpha = \pi/2$  and  $\theta \in [0, \pi/2]$  with  $\rho$  the radius length. The polar polynomial in 3.18 is symmetric and can thus only be used for instances in which  $d = e$ .

$$\rho(\phi) = R \left[ 1 + \frac{\phi^2}{2} - \frac{\phi^3}{\pi/2} + \frac{\phi^4}{\pi^2/2} \right] \quad (3.18)$$

The transformation of the polar polynomial into the Cartesian reference frame is done as follows:

$$x(\phi) = \rho(\phi)\cos(\phi) \quad y(\phi) = \rho(\phi)\sin(\phi) \quad (3.19)$$

### 3.1.4 Geometric Path Discussion

An overlay of the three geometric paths is shown in figure 3.5, table 3.1 shows the lengths of the generated curves. The extended lengths refer to the curves shown in figure 3.6.

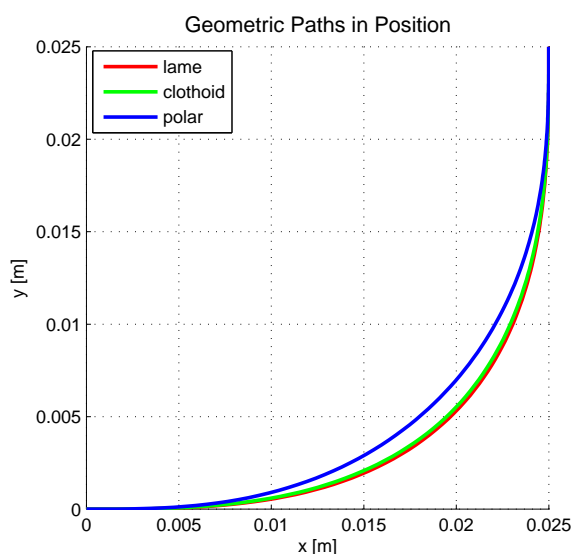


Figure 3.5: Blending sections for the adept cycle

Curve Type	Length [mm]	Curve Type	Length [mm]
Lamé	42.156	Extended Lamé	59.307
Clothoid	41.333	Extended Clothoid	57.015
Polar	41.106		

Table 3.1: Blending lengths for geometric paths

Using the blending restrictions discussed in subsection 3.1.1, the following plot may be generated. From table 3.1, it can be seen that the Lamé curve generates the longest blending length while the polar polynomial generates the shortest. In the next section the various motion profiles will be introduced.

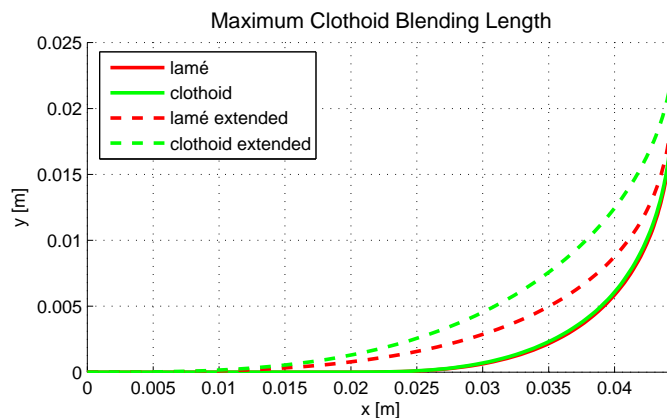


Figure 3.6: *Extended clothoid and Lamé curve generated for  $e = 44.5\text{mm}$*

## 3.2 Motion Profiles

A motion profile is a monotonic function in  $s$  describing the movement of the end effector along the geometric path. It is of interest to define a trajectory so that it is continuous in acceleration. This is to say that it is defined without discontinuities [16]. Pragmatism in industry however adopts profiles with discontinuities as they allow for faster cycle times.

The motion profiles are designed to vary between  $s = 0$  and  $s = 1$ , as a function of the normalized time  $\eta = \frac{t}{t_f}$  ( $t_f$  represents the cycle time). The motion profiles are designed with respect to this cycle time  $t_f$ , the basis from which the necessary velocities and accelerations of the particular motion profile are found. In upcoming subsections, the motion profiles discussed in the bibliographic report are presented.

### 3.2.1 Seventh Degree Polynomial

This motion profile is continuous in velocity, acceleration and jerk. Among the profiles investigated, it provides for the smoothest motion along a given geometric path. The smoothness comes at the cost of higher accelerations as shown in figure 3.7. The motion profile is determined from the following polynomial:

$$s(\eta) = a_7\eta^7 + a_6\eta^6 + a_5\eta^5 + a_4\eta^4 + a_3\eta^3 + a_2\eta^2 + a_1\eta + a_0$$

The boundary conditions used to determine the coefficients are given in table 3.2:

Boundary Condition	Value	Boundary Condition	Value
$s(0)$	0	$s(1)$	1
$\dot{s}(0)$	0	$\dot{s}(1)$	0
$\ddot{s}(0)$	0	$\ddot{s}(1)$	0
$\overset{\cdot}{\ddot{s}}(0)$	0	$\overset{\cdot}{\ddot{s}}(1)$	0

Table 3.2: *Boundary conditions for the 7<sup>th</sup> degree polynomial*

The normalized seventh degree motion profile is defined in position  $s$ , velocity  $\dot{s}$  and acceleration  $\ddot{s}$  in equations 3.20, 3.21 and 3.22:

$$s(\eta) = -20\eta^7 + 70\eta^6 - 84\eta^5 + 35\eta^4 \quad (3.20)$$

$$\dot{s}(\eta) = \frac{1}{t_f} (-140\eta^6 + 420\eta^5 - 420\eta^4 + 140\eta^3) \quad (3.21)$$

$$\ddot{s}(\eta) = \frac{1}{t_f^2} (-840\eta^5 + 2100\eta^4 - 1680\eta^3 + 420\eta^2) \quad (3.22)$$

### 3.2.2 Trapezoidal Profile

The trapezoidal motion profile has jump discontinuities in acceleration occurring at  $\eta = 0$ ,  $\eta = \tau$ ,  $\eta = 1 - \tau$  and  $\eta = 1$ .  $\tau$  is the normalized acceleration time period. The trapezoidal profile is a piecewise function, consisting of a constant acceleration phase followed by a constant velocity phase. By decreasing the acceleration period  $\tau$ , for a given  $t_f$ , the higher the required acceleration (figure 3.7).

$$s(\eta) = \begin{cases} \frac{1}{2}\eta^2 k_a & \text{for } \eta \leq \tau \\ (\eta - \frac{\tau}{2})k_v & \text{for } \tau < \eta \leq 1 - \tau \\ 1 - \frac{1}{2}(1 - \eta)^2 k_a & \text{for } 1 - \tau < \eta \leq 1 \end{cases} \quad (3.23)$$

$$\dot{s}(\eta) = \begin{cases} \frac{1}{t_f}\eta k_a & \text{for } \eta \leq \tau \\ \frac{1}{t_f}k_v & \text{for } \tau < \eta \leq 1 - \tau \\ \frac{1}{t_f}(1 - \eta)k_a & \text{for } 1 - \tau < \eta \leq 1 \end{cases} \quad (3.24)$$

$$\ddot{s}(\eta) = \begin{cases} \frac{1}{t_f^2}k_a & \text{for } \eta \leq \tau \\ 0 & \text{for } \tau < \eta \leq 1 - \tau \\ -\frac{1}{t_f^2}k_a & \text{for } 1 - \tau < \eta \leq 1 \end{cases} \quad (3.25)$$

For a fixed cycle time, and a desired acceleration period, the maximum normalized acceleration  $k_a$  and velocity  $k_v$  are calculated as follows:

$$k_v = \frac{1}{1 - \tau} \quad k_a = \frac{k_v}{\tau}$$

### 3.2.3 Bang-bang Profile

The bang-bang profile is only continuous in position and velocity, but lacks smoothness. Jump discontinuities are present at  $\eta = 0$ ,  $\eta = 0.5$  and  $\eta = 1$ . The bang-bang profile provides the fastest cycle time possible. Of the three profiles investigated, the bang-bang profile generates the lowest acceleration values for a fixed cycle time  $t_f$  (see figure 3.7).

$$s(\eta) = \begin{cases} 2\eta^2 & \text{for } \eta \leq \frac{1}{2} \\ -2(\eta - 1)^2 & \text{for } \eta > \frac{1}{2} \end{cases} \quad (3.26)$$

$$\dot{s}(\eta) = \begin{cases} \frac{4}{t_f}\eta & \text{for } \eta \leq \frac{1}{2} \\ -\frac{4}{t_f}(\eta - 1) & \text{for } \eta > \frac{1}{2} \end{cases} \quad (3.27)$$

$$\ddot{s}(\eta) = \begin{cases} \frac{4}{t_f^2} & \text{for } \eta \leq \frac{1}{2} \\ -\frac{4}{t_f^2} & \text{for } \eta > \frac{1}{2} \end{cases} \quad (3.28)$$

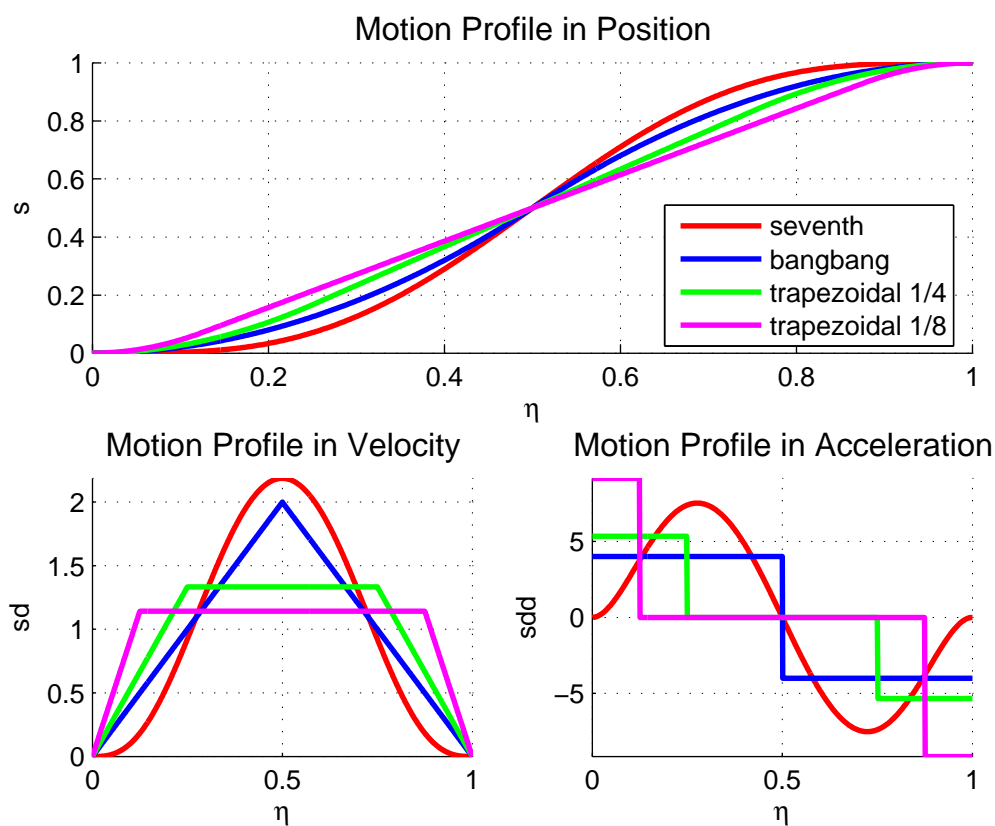


Figure 3.7: Motion profiles generated for  $t_f = 1$

### 3.3 Trajectory Characteristics

In this section, the effect of transversing a particular geometric path with a given motion profile is studied. Essentially, the motion profile dictates the rate at which the Cartesian coordinates are sampled from the geometric path.

Motion Profiles	Geometric Paths
$7^{th}$ order polynomial	Lamé curve
Bang-bang	Clothoid pair
$\frac{1}{4}$ Trapezoidal	Polar polynomial
$\frac{1}{8}$ Trapezoidal	

Table 3.3: *Tested motion profiles and geometric paths*

The profiles and paths listed in table 3.3 allow 12 different path-profile combinations to be analyzed. At this point, the motion profiles are generated for a cycle time of 1 second, various characteristics of the generated trajectories may then be investigated. The  $\frac{1}{4}$  and  $\frac{1}{8}$  trapezoidal profiles refer to acceleration durations of  $\frac{t_f}{4}$  and  $\frac{t_f}{8}$  respectively<sup>2</sup>. As the cycle time is fixed at  $t_f = 1$ , it can be seen, as in figure 3.7 that the trapezoidal trajectories require higher accelerations than the bang-bang trajectories.

#### Task Space

Table 3.4 shows a comparison of the velocity and acceleration characteristics of each trajectory. In the table red indicates the highest value in either velocity or acceleration performance, while blue indicates the lowest value. A trend that can be observed is that the Lamé curve requires higher velocities and accelerations, due to the fact the it has the longest curve length (table 3.1).

Motion Profiles	Velocity [ $m/s$ ]			Acceleration [ $m/s^2$ ]		
	Lamé	Clothoid	Polar	Lamé	Clothoid	Polar
$7^{th}$ order polynomial	<b>0.84068</b>	0.83347	0.83608	7.7818	7.3686	7.0384
Bang-bang	0.76753	0.76095	0.76333	5.1687	4.7268	<b>4.4662</b>
$\frac{1}{4}$ Trapezoidal	0.51242	0.50802	0.50962	6.8895	6.2916	5.9544
$\frac{1}{8}$ Trapezoidal	0.43921	<b>0.43545</b>	0.43681	<b>11.8115</b>	10.7638	10.0453

Table 3.4: *Task space velocity and acceleration comparison of generated trajectories*

<sup>2</sup>Where  $t_f$  is the cycle time

The generated trajectories are presented in figures 3.8, 3.9 and 3.10.

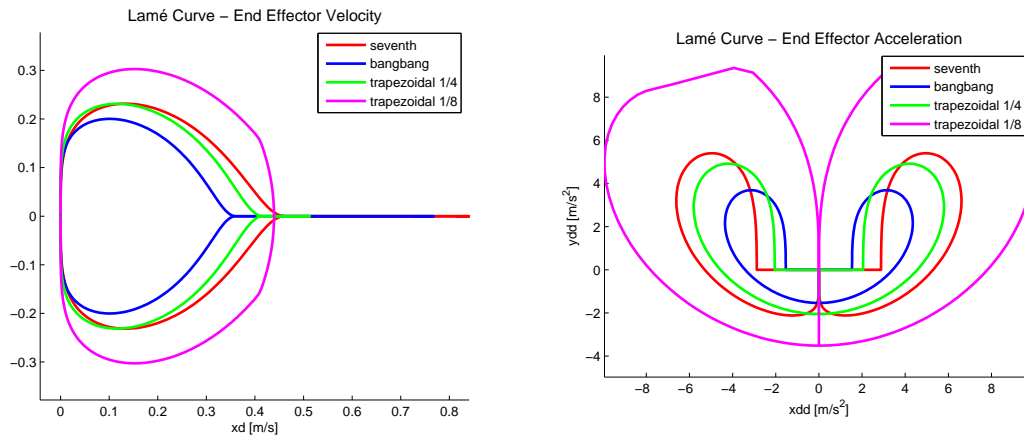


Figure 3.8: *Lamé curve trajectories*

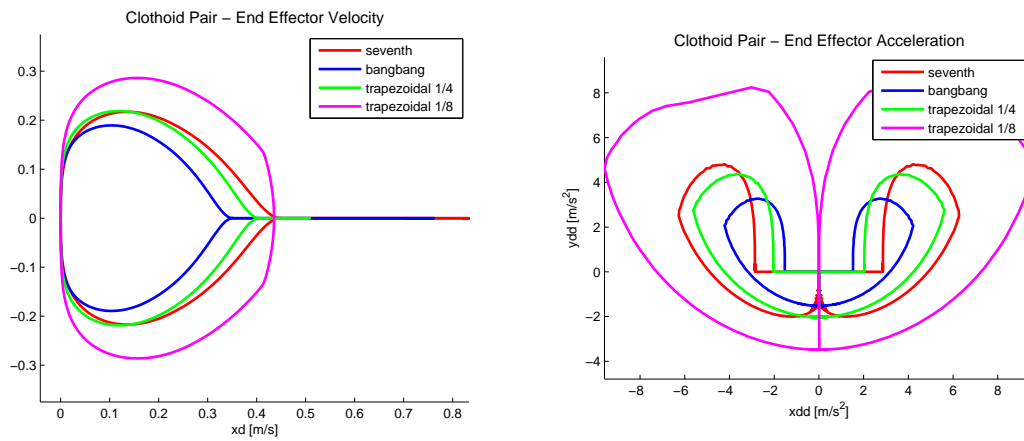


Figure 3.9: *Clothoid pair trajectories*

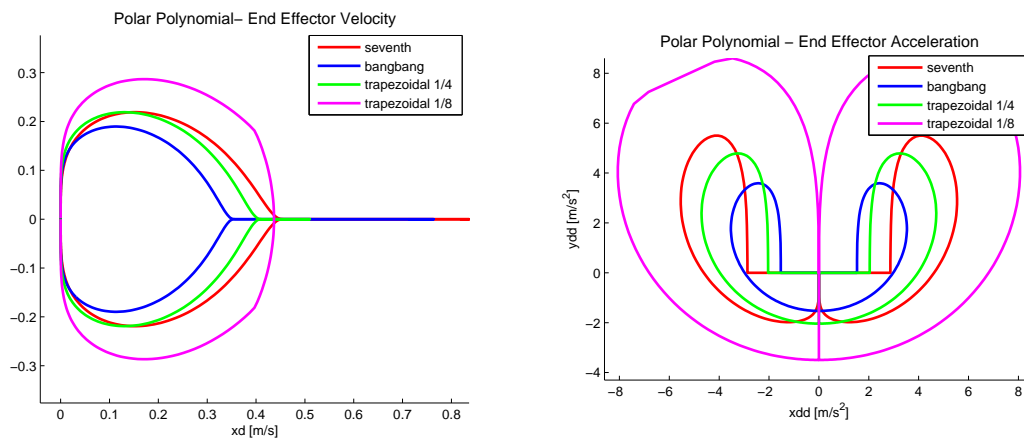


Figure 3.10: *Polar polynomial trajectories*

## Joint Space

The next study investigates the effect of trajectory following on the five bar mechanism. The inverse geometric and kinematic models for the rigid case (sections 2.2.1 and 2.2.3) are used to compute the actuated joint trajectories. The generated joint trajectories are assessed with respect to:

- motion profile - geometric path combinations
- cycle times
- blending lengths

Figures 3.11, 3.12 and 3.13 show the trajectories in the joint space for  $t_f = 1$ . The spectral content of each signal in acceleration is determined. Each figure shows the Power Spectral Density function of each signal, relating distribution of energy in the signal to frequency. This distribution of energy is important as it gives an indication to the extent whereby the resonance frequencies of the structure will be excited by each trajectory. It can be observed that the spectral content of the 7<sup>th</sup> degree polynomial is much more forgiving than those of the trapezoidal and bang-bang profiles.

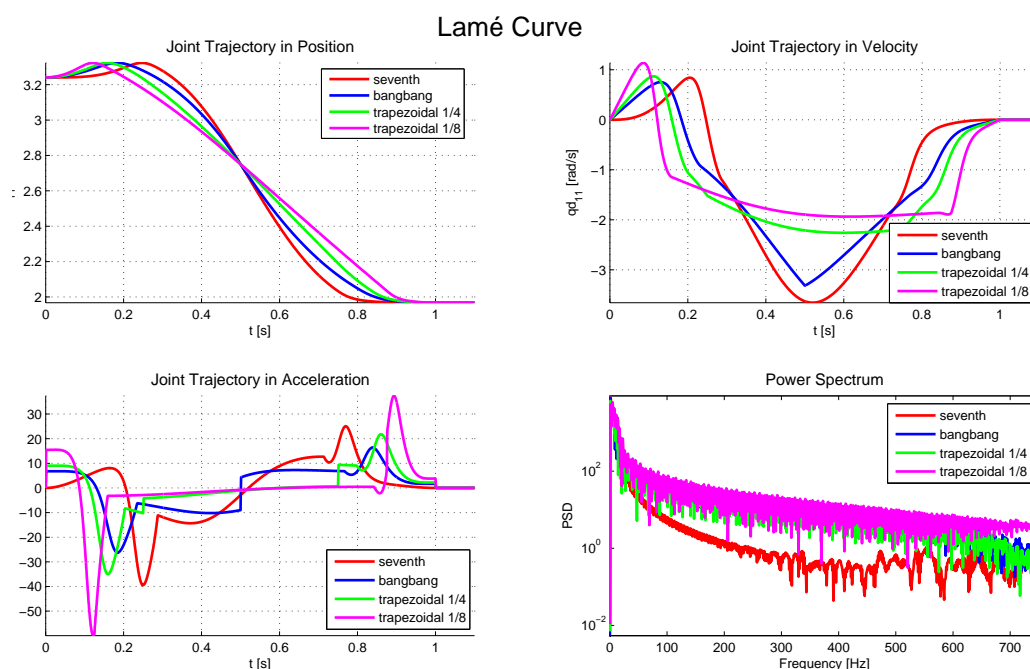


Figure 3.11: *Lamé curve joint space trajectory and spectral content*

The characteristic features of each plot are shown in table 3.5:

Motion Profiles	Velocity [ $rad/s$ ]			Acceleration [ $rad/s^2$ ]		
	Lamé	Clothoid	Polar	Lamé	Clothoid	Polar
7 <sup>th</sup> order polynomial	0.84045	0.8157	0.75216	25.0858	25.3279	21.2023
Bang-bang	0.75156	0.73162	<b>0.68131</b>	16.4343	16.4834	<b>13.7179</b>
$\frac{1}{4}$ Trapezoidal	0.86783	0.8448	0.78669	21.8879	21.9759	18.1215
$\frac{1}{8}$ Trapezoidal	<b>1.1363</b>	1.1061	1.0300	37.432	<b>37.6681</b>	30.9457

Table 3.5: *Characteristic features of joint space trajectories*

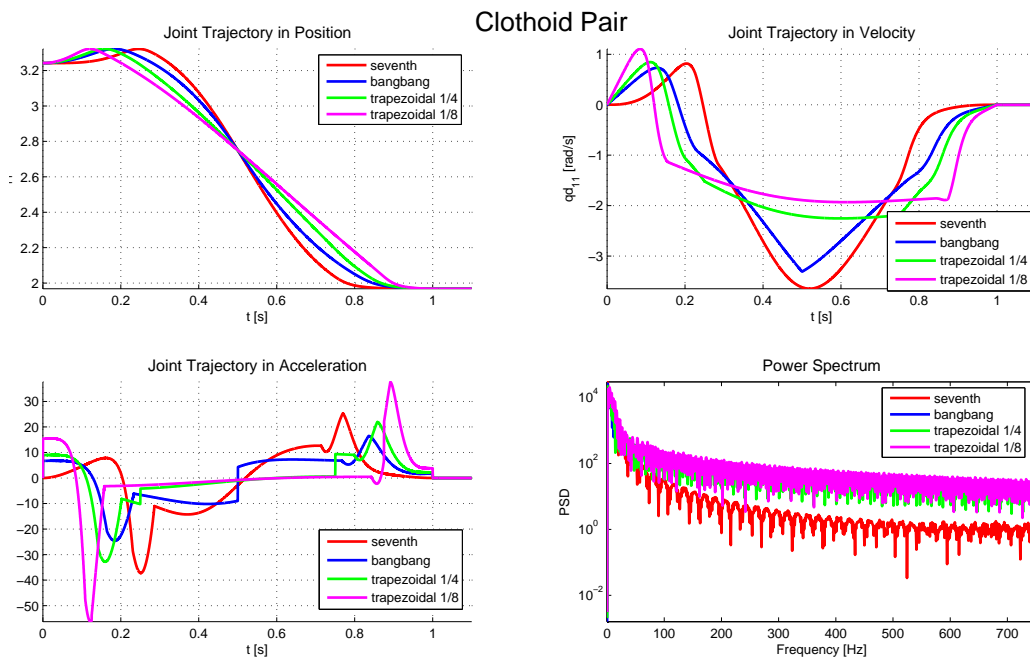


Figure 3.12: Clothoid pair joint space trajectory and spectral content

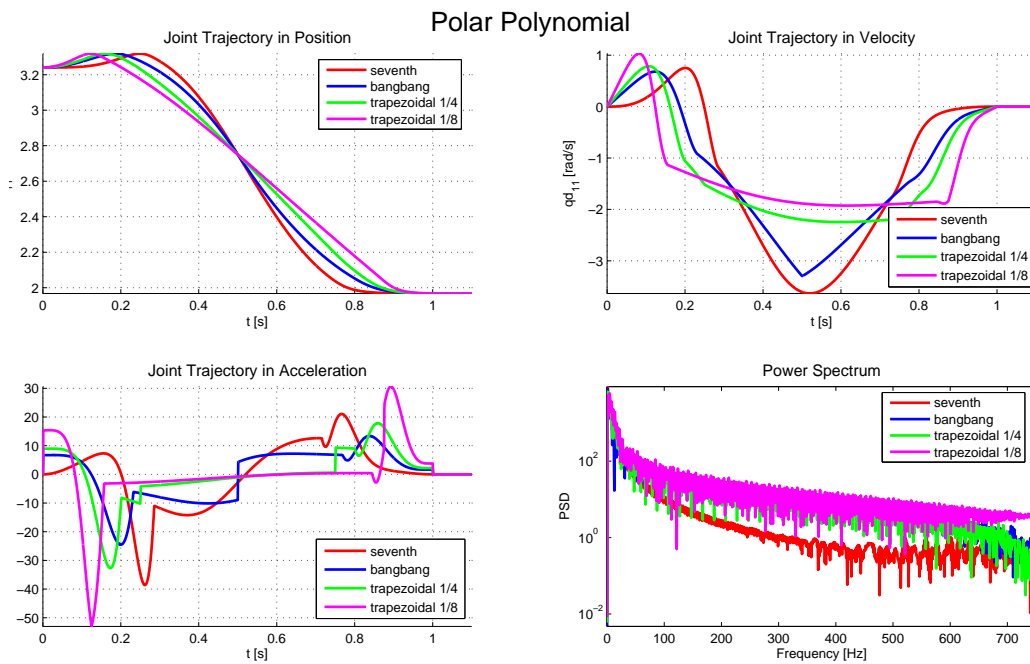


Figure 3.13: Polar polynomial joint space trajectory and spectral content

The general trend of the motion profile-trajectory combination can be observed in figure 3.14. While the difference is not great, it can be seen that Lamé curves correspond to trajectories with lower energy while polar polynomials correspond to higher energies.



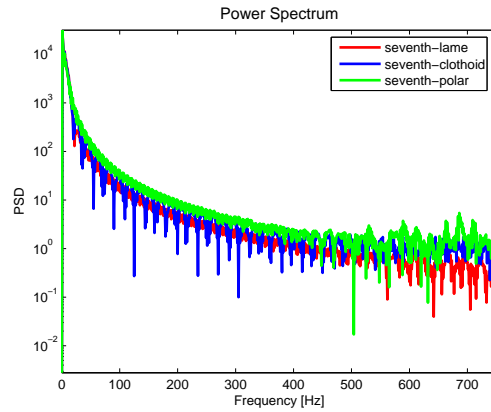


Figure 3.14: Spectral content for the various geometric paths based on a 7<sup>th</sup> order polynomial traversal

Figures 3.15 and 3.16 show the effect of varying the cycle time and the blending length  $d^3$ . As expected, decreasing the cycle time  $t_f$  inflates the energy content at all frequencies. Furthermore, the shorter the blending length, and thus, the sharper the corner, the higher the energy content of the input signal.

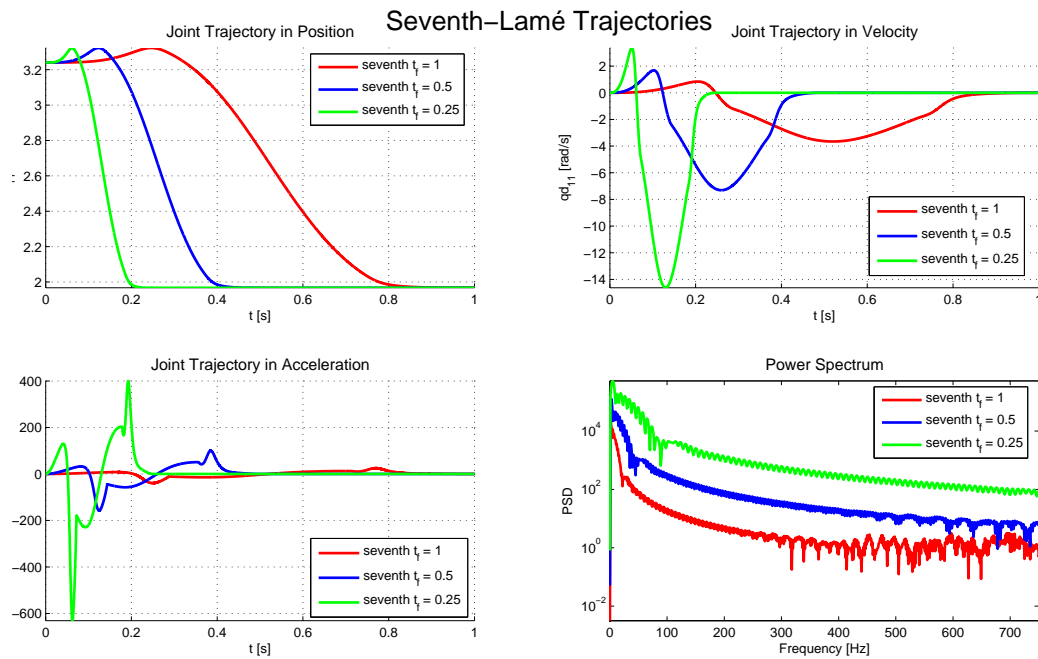


Figure 3.15: Spectral content for seventh-lamé trajectories for cycle times of  $t_f = 1$ ,  $t_f = 0.5$  and  $t_f = 0.25$

<sup>3</sup>the symmetric case is considered, i.e.  $d = e$

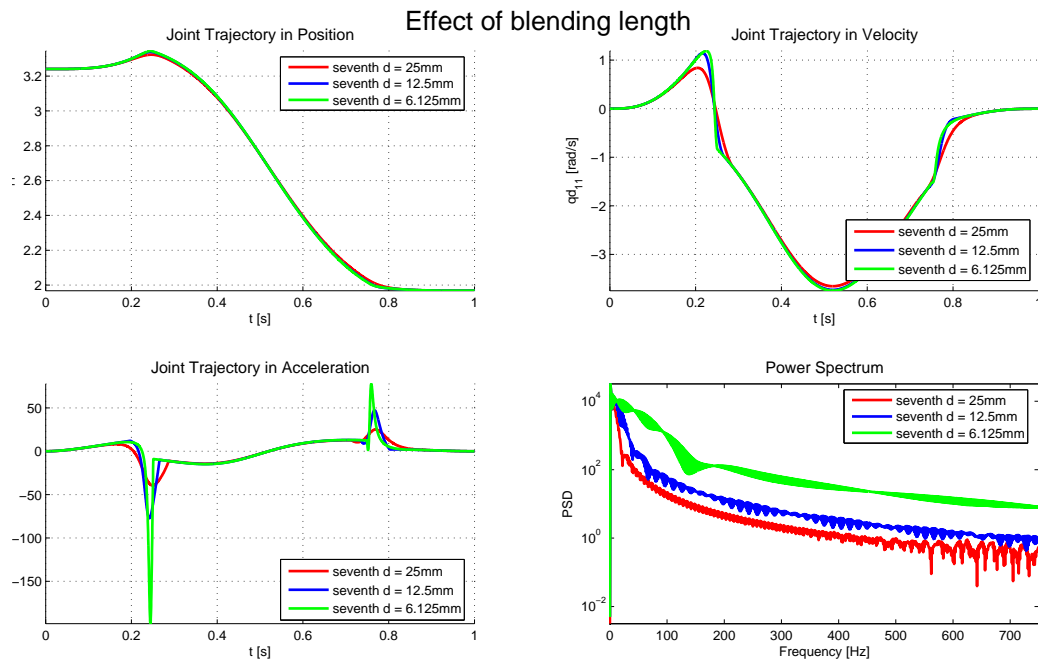


Figure 3.16: Spectral content for seventh-lamé trajectories for symmetric blending lengths of  $d = 25\text{mm}$ ,  $d = 12.5\text{mm}$  and  $d = 6.125\text{mm}$

### Trajectory Discussion

From the analysis done in section 3.3, it is clear that there is a trade-off between the cycle time and the amount of energy distribution in the trajectory signals. The following conclusions may be drawn:

- Shorter curve lengths require lower accelerations
- Lower cycle times require higher accelerations and increase the spectral content of the signal at all frequencies
- Sharper corners increase the spectral content of the signal at all frequencies

In the next section the elastodynamic model of the five bar mechanism will be excited with the trajectories discussed in this section.

# Chapter 4

## Simulation

Adept Technology, Inc. [13], manufacturers of the worlds fastest robot, specify the following cycle-time payload combinations for the standard adept cycle:

Adept Cycle (Std.) - Sustained Standard Cycle: 25/305/25 (mm)	
Payload [kg]	Cycle time $t_f$ [s]
0.1	0.30
1.0	0.36
2.0	0.37
4.0	0.41
6.0	0.43

Table 4.1: Adept cycle times and payloads

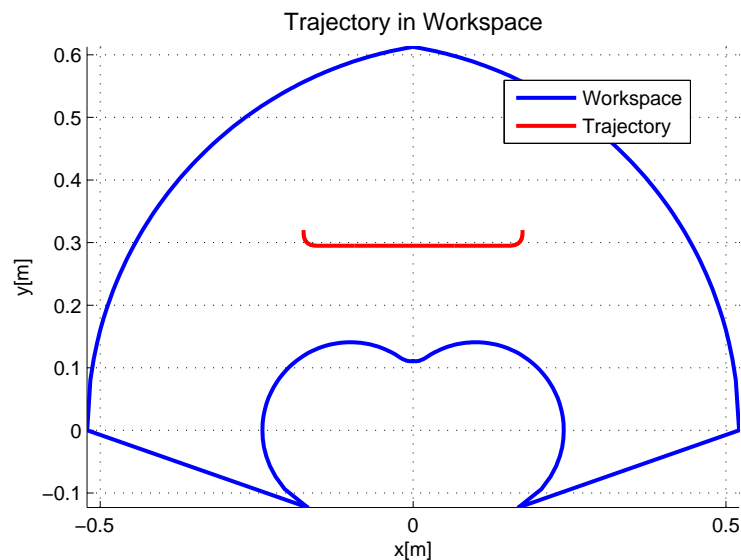


Figure 4.1: Position of the trajectory in the workspace (gravity is taken upwards)

In this section, it is assumed that a perfect controller is available. The inverse dynamic model (section 2.1.9) is used to evaluate the vibratory performance of the five bar mechanism as it traverses the various trajectories (see figure 4.1). The simulations are conducted for the 0.1kg and 6.0kg cases listed in table 4.1. The simulation is run at a sampling frequency of 10MHz. The following results will be presented and discussed:

- Trajectory following in the task space
- Required joint torques
- Excited vibrations
- Spectral content of the vibratory signal

## 4.1 Simulation Set 1: 0.1kg $t_f = 0.3s$

### 4.1.1 Vibrational Domain

The frequency analysis developed in section 2.3.2, may be used to determine the evolution of the system's natural frequency as it follows the adept cycle. Figure 4.2 represents the frequencies present on a cycle with clothoid blending. It can be seen that the first natural frequency varies with  $\pm 2Hz$  about  $126Hz$ , while the margin increases to  $\pm 7.5Hz$  about  $1912Hz$  for the third natural frequency.

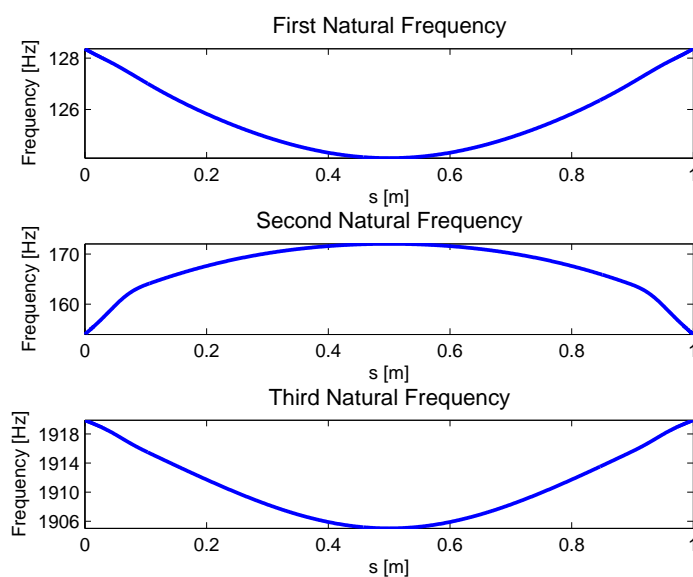


Figure 4.2: *Frequency distribution along Adept Cycle with a 100g payload. Line styles: - Lamé, - - Clothoid, ... Polar*

### 4.1.2 Simulation Results

The simulation results are now presented. In each figure, 12 results are superposed, line colour represents the different motion profiles used. Figure 4.3 shows the velocity and accelerations obtained in the task space with the inclusion of elastic deformation.

#### Task Space

The effect of deformation is most notable in the acceleration plot. The emergent trajectory does not follow the expected trajectory in acceleration. At the end of the cycle time  $t_f$ , the relative position between the actual and expected position, the velocity and the acceleration of the end effector as averaged per motion profile is given in table 4.2. Ideally, the relative position between the actual and desired end effector positions is 0, while the desired velocity and acceleration are 0 in both cases.

From the table it can be observed that the end effector states in position are the best for the bang-bang profile, this due to the fact that the bang-bang profile has the lowest acceleration value. What is interesting to note, is that the 7<sup>th</sup> degree polynomial offers the best performance in velocity and acceleration error, owing to the continuity and smoothness of its acceleration profile at this point.

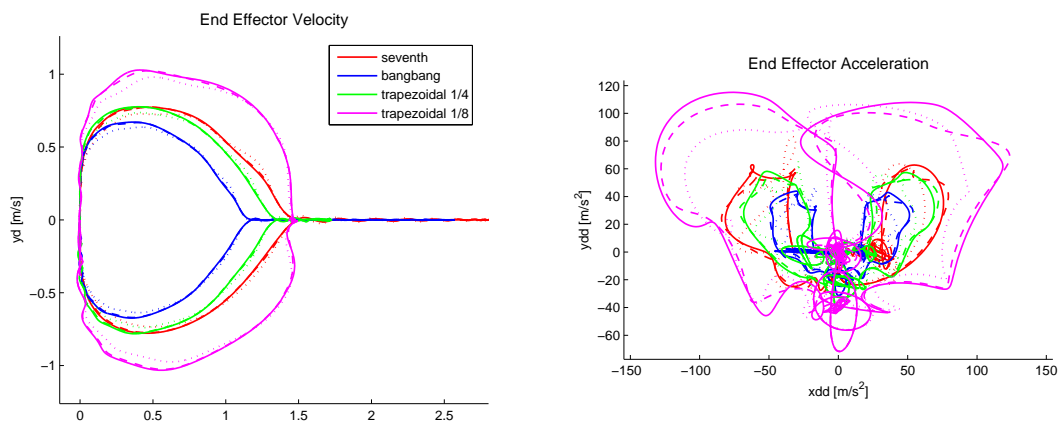


Figure 4.3: Simulation results for a 100g payload in the task space

Motion Profiles	Position [mm]		Velocity [m/s]		Acceleration [m/s <sup>2</sup> ]	
	$x_{rel}$	$y_{rel}$	$\dot{x}$	$\dot{y}$	$\ddot{x}$	$\ddot{y}$
7 <sup>th</sup> order polynomial	-0.00349	-0.01559	0.00074	0.00081	0.4998	0.3127
Bang-bang	0.00068	0.00746	0.00042	0.00589	0.3998	-16.626
$\frac{1}{4}$ Trapezoidal	0.00184	0.01573	-0.00065	0.00647	0.6456	-22.756
$\frac{1}{8}$ Trapezoidal	0.00671	0.04156	-0.00559	0.00698	0.37523	-41.73167

Table 4.2: Terminal end-effector state at  $t_f = 0.3$  for a payload of 100g

Motion Profiles	Velocity [m/s]			Acceleration [m/s <sup>2</sup> ]		
	Lamé	Clothoid	Polar	Lamé	Clothoid	Polar
7 <sup>th</sup> order polynomial	2.8032	2.8010	2.7881	88.652	90.736	89.602
Bang-bang	2.5689	2.5668	2.5549	59.677	61.849	53.019
$\frac{1}{4}$ Trapezoidal	1.7259	1.726	1.714	79.671	83.456	71.594
$\frac{1}{8}$ Trapezoidal	1.5130	1.5028	1.5123	154.65	146.94	128.40

Table 4.3: Maximum task space velocity and acceleration for a payload of 100g and a cycle time of  $t_f = 0.3s$ 

## Joint Torques

The resultant joint torques show the effect of the vibrations on the required torque. The oscillations in the torque signal are more pronounced for signals with discontinuities in vibration. From the behaviour of the signals, it is clear to see that the vibrations are excited at these discontinuities. The bang-bang profile shows excitation at the cycle mid-point while the trapezoidal signals show excitation at  $\frac{t_f}{4}$  and  $\frac{t_f}{8}$ . The maximum torques required for each signal are summarized in table 4.4.

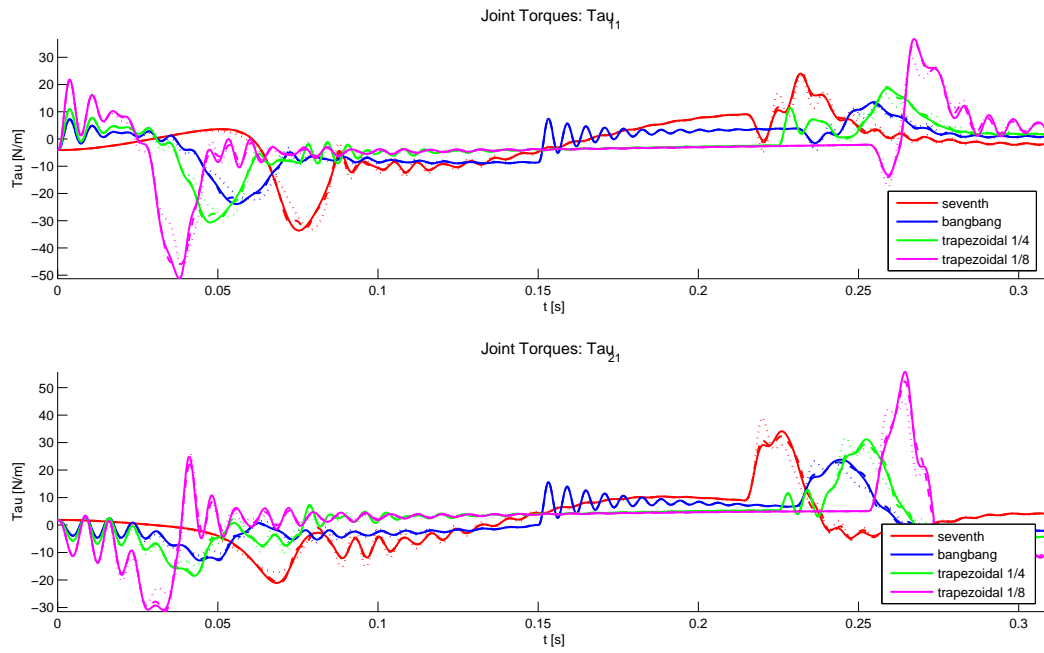


Figure 4.4: Joint torques for a 100g payload. Line styles: - Lamé, - - Clothoid, ... Polar

### Vibrations

The elastic coordinates  $\mathbf{q}_e$  are also obtained through the solution of the inverse dynamic model. The elastic coordinates in bending and in tension-compression are presented in figures 4.5 and 4.6 respectively.

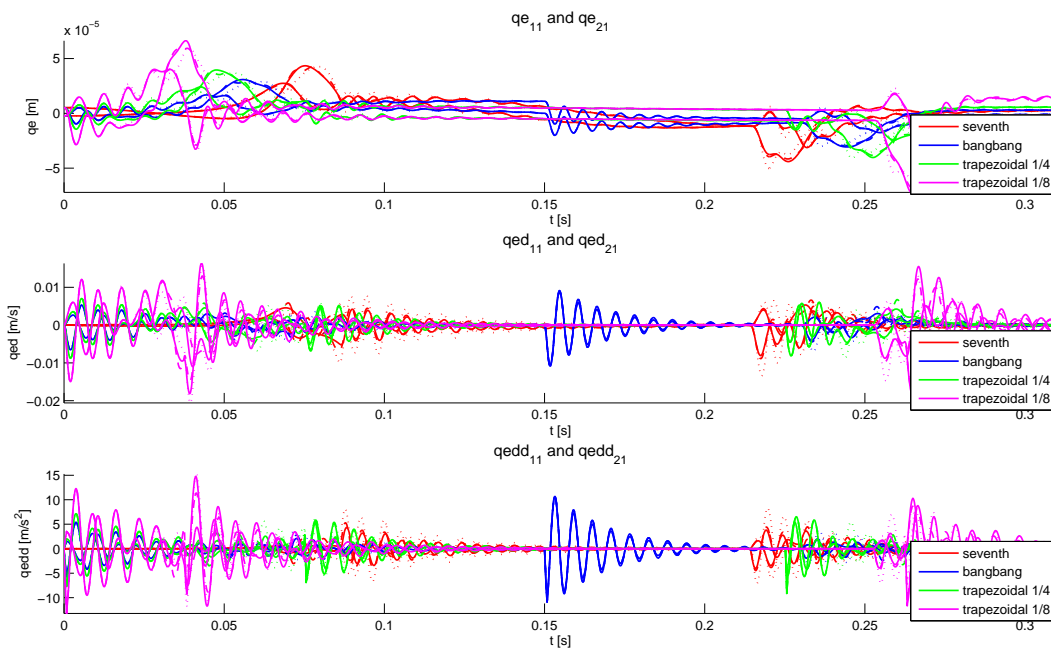


Figure 4.5: Elastic Coordinates in Bending for a 100g payload. Line styles: - Lamé, - - Clothoid, ... Polar

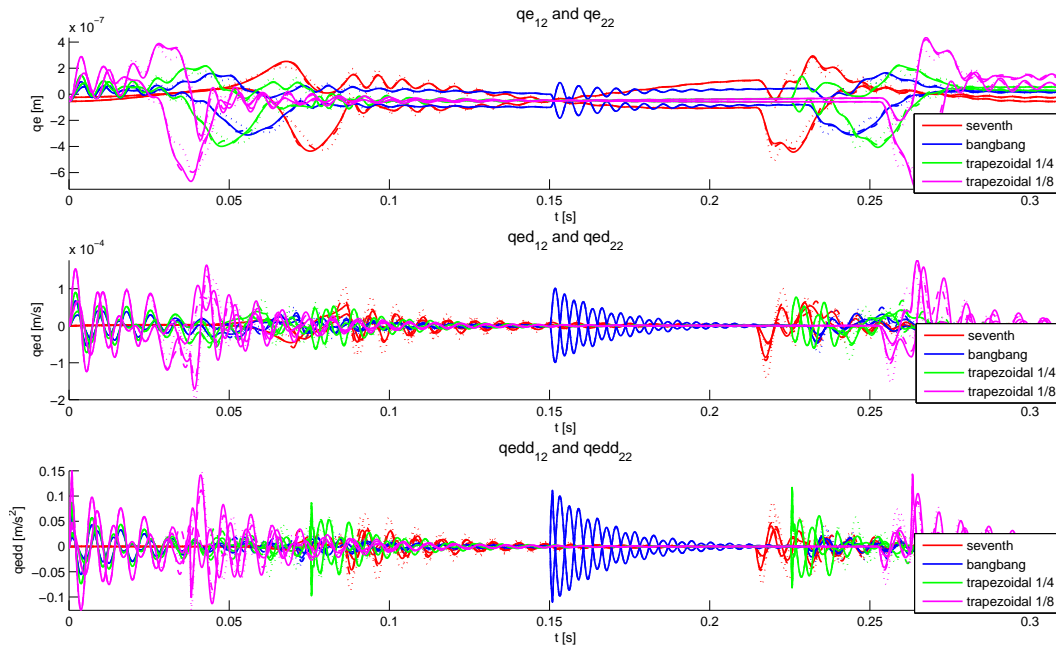


Figure 4.6: *Elastic Coordinates in Tension-Compression for a 100g payload. Line styles: - Lamé, - - Clothoid, ... Polar*

The spectral content of the signals may be analyzed to identify the excited frequencies. The signal is shown between 0 and 700Hz as there is very little activity at higher frequencies. The results show that the frequencies coinciding with the first and second resonances are excited. This is to be expected, referring to figure 3.15, it can be seen that the energy of the input signal attenuates greatly after a frequency of 300Hz.

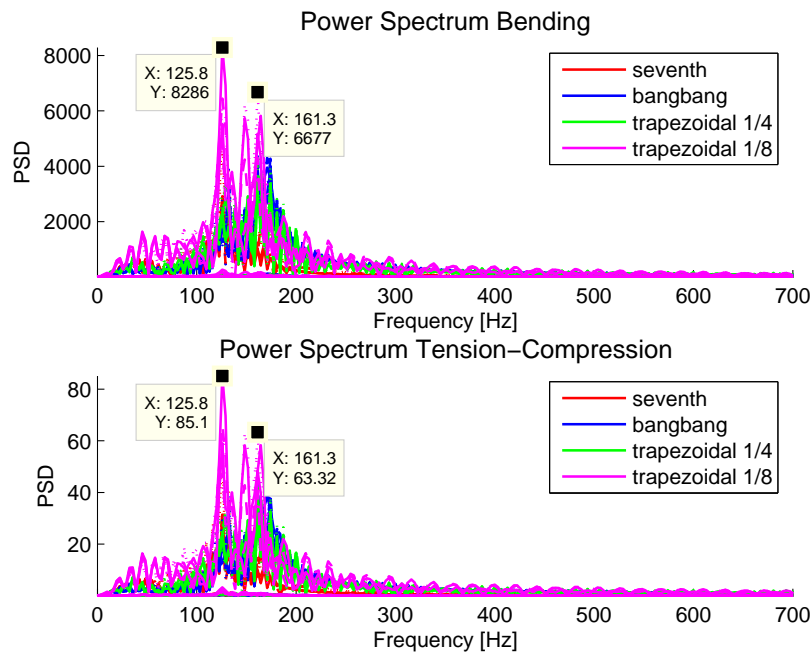


Figure 4.7: *Spectral Distribution for a 100g payload. Line styles: - Lamé, - - Clothoid, ... Polar*

The results of this simulation set is summarized in table 4.4. The table firstly shows the maximum torque required. Secondly the root mean square (RMS) value of the acceleration error is computed using equation 4.1. Lastly, the maximum deflection in the elastic coordinates is noted, this maximum deflection occurs in the links in bending.

$$RMS_{error} = \sqrt{\frac{\sum_1^n (\ddot{X}_{desired} - \ddot{X}_{actual})^2}{n}} \quad (4.1)$$

where  $n$  is the number of data points

	Lamé	Clothoid	Polar
Motion Profiles	Torque [Nm]		
7 <sup>th</sup> order polynomial	33.6384	32.737	33.0867
Bang-bang	23.9012	23.1011	22.3707
$\frac{1}{4}$ Trapezoidal	30.6662	29.4722	28.56
$\frac{1}{8}$ Trapezoidal	51.3054	45.9056	47.4447
Motion Profiles	RMS Acceleration Error [m/s <sup>2</sup> ]		
7 <sup>th</sup> order polynomial	3.3563	3.8525	6.2169
Bang-bang	5.2095	5.3852	5.7002
$\frac{1}{4}$ Trapezoidal	5.2813	5.6053	5.9695
$\frac{1}{8}$ Trapezoidal	9.8592	8.7226	9.5968
Motion Profiles	Max Deflection [mm]		
7 <sup>th</sup> order polynomial	0.04339	0.04223	0.04269
Bang-bang	0.03082	0.02979	0.02885
$\frac{1}{4}$ Trapezoidal	0.03957	0.03802	0.03684
$\frac{1}{8}$ Trapezoidal	0.0663	0.05931	0.06134

Table 4.4: Task space velocity and acceleration comparison of generated trajectories

From the table it can be seen that the worst performance, on all counts, is associated with the  $\frac{1}{8}$  trapezoidal profile as it requires the highest accelerations. The required torque is closely related to the path length, and thus the lowest torques correspond to the polar polynomial trajectories. The best performance in terms of the RMS acceleration error is associated with the smoothest trajectory, the 7<sup>th</sup> degree polynomial-Lamé curve.



## Errors in the Task Space

The norm of the error in the task space is shown in figure 4.8. An understanding of the residual deformations and energies in the signal may be obtained from studying table 4.5. While the smoothness of a curve significantly decreases the residual error, the maximum acceleration achieved along a path plays a dominant role. The trends correspond to those seen in 3.14. The polar polynomial has slightly higher spectral energy at the natural frequencies of the robot and is associated with higher residual errors.

What is clear is that the smooth 7<sup>th</sup> order curve presents the best results in the error norms. At this slower cycle speed of  $t_f = 0.3$  and low payload of 100g, the smoothness of the trajectory is the dominant factor for the level of residual activity in position.

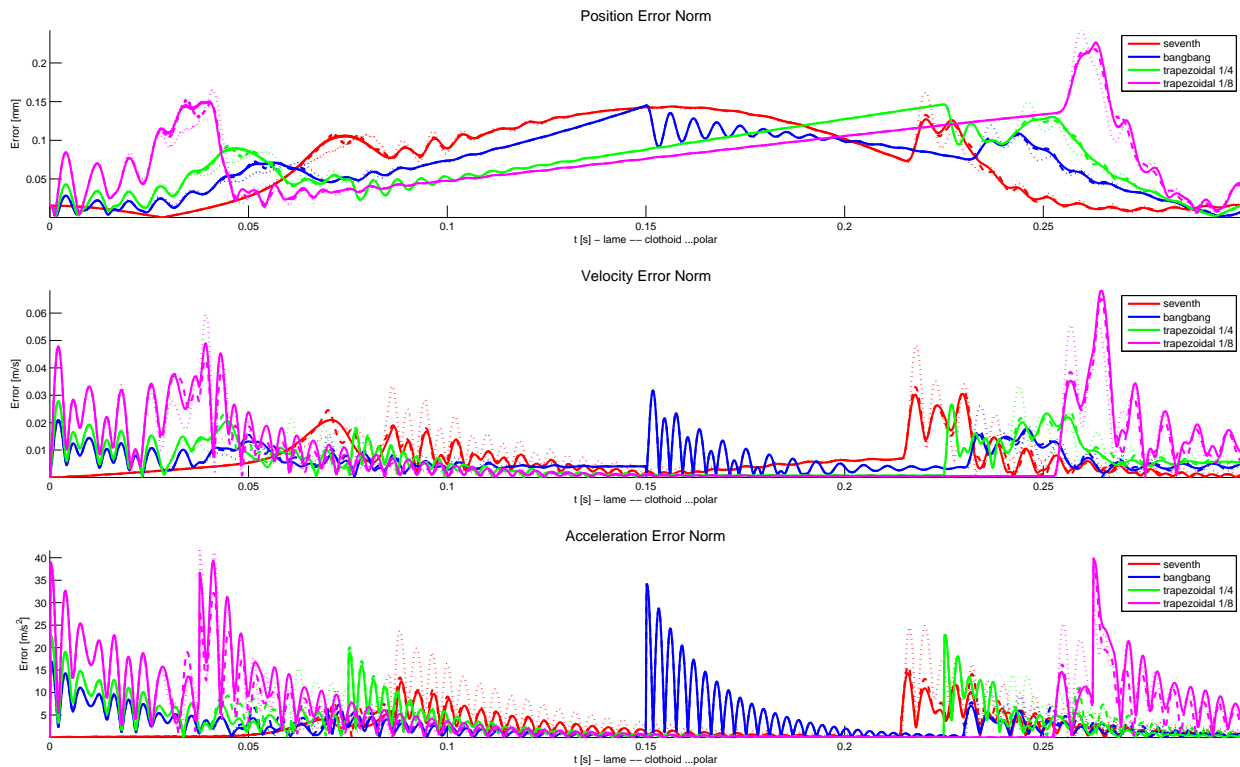


Figure 4.8: *Error norm in the task space with a 100g payload. Line styles: - Lamé, - - Clothoid, ... Polar*

	Lamé	Clothoid	Polar
Motion Profiles	Position [mm]		
7 <sup>th</sup> order polynomial	0.0157	0.0009	0.3109
Bang-bang	0.0078	0.0007	0.5573
$\frac{1}{4}$ Trapezoidal	0.0160	0.0017	0.9366
$\frac{1}{8}$ Trapezoidal	0.0439	0.0049	0.2872
Motion Profiles	Velocity [m/s]		
7 <sup>th</sup> order polynomial	0.0009	0.0053	0.4973
Bang-bang	0.0049	0.0050	1.0716
$\frac{1}{4}$ Trapezoidal	0.0055	0.0055	0.2611
$\frac{1}{8}$ Trapezoidal	0.0087	0.0062	0.8352
Motion Profiles	Acceleration [m/s <sup>2</sup> ]		
7 <sup>th</sup> order polynomial	0.5573	0.0045	1.3193
Bang-bang	0.4973	0.0050	1.0716
$\frac{1}{4}$ Trapezoidal	0.8352	0.0045	1.3193
$\frac{1}{8}$ Trapezoidal	1.8212	0.0083	3.0404

Table 4.5: Residual norms at end effector end points

## 4.2 Simulation Set 2: 6.0kg $tf = 0.43s$

The cycle with the heaviest payload is now investigated (table 4.1). Compared to the simulation done in the previous section (4.1), the payload is increased by a factor of 60 while the cycle time is increased by a factor of 1.43.

### 4.2.1 Vibrational Domain

The heavier payload transforms the frequencies present along the geometric path (compare figures 4.2 and 4.9). The first natural frequency is now located at  $58Hz \pm 1Hz$ , the second at  $80Hz \pm 6Hz$  and finally the third natural frequency at  $1823Hz \pm 13Hz$ .

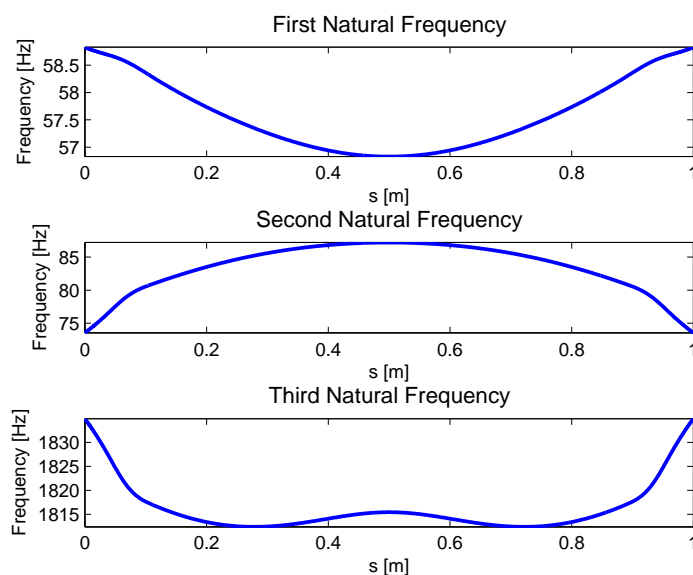


Figure 4.9: Frequency distribution along Adept Cycle with a 6000g payload. Line styles: - Lamé, - - Clothoid, ... Polar

## 4.2.2 Simulation Results

Figure 4.10 shows the velocity and accelerations obtained in the task space with the inclusion of elastic deformation. With the higher payload, oscillations about the desired end position of the end effector become visible. Here the results are averaged according to the various geometric paths so that the general trends may be seen.

### Task Space

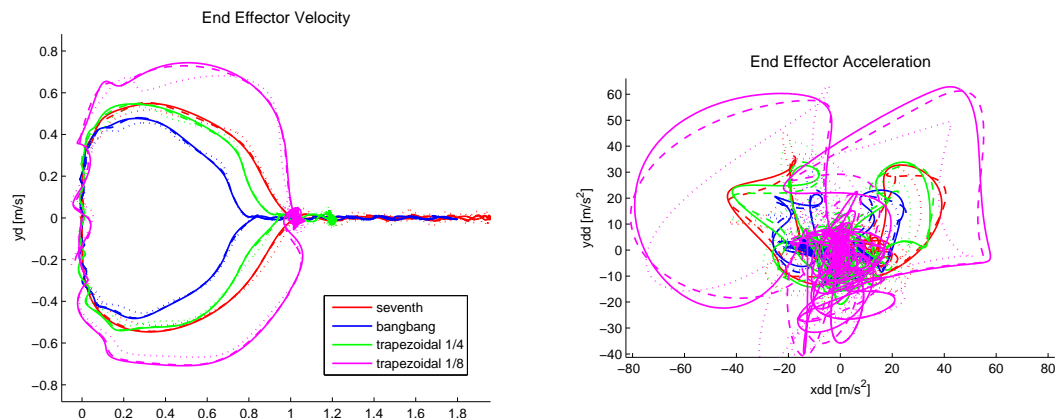


Figure 4.10: Simulation results for a 6kg payload in the task space. Line styles: - Lamé, - - Clothoid, ... Polar

Motion Profiles	Position [mm]		Velocity [m/s]		Acceleration [m/s <sup>2</sup> ]	
	$x_{rel}$	$y_{rel}$	$\dot{x}$	$\dot{y}$	$\ddot{x}$	$\ddot{y}$
7 <sup>th</sup> order polynomial	-0.00299	-0.04231	-0.00256	-0.00102	-1.1090	-2.9313
Bang-bang	-0.00944	-0.02703	0.00801	0.00685	0.6245	-5.7937
$\frac{1}{4}$ Trapezoidal	0.01330	0.01512	0.01400	0.00966	-1.793	-12.188
$\frac{1}{8}$ Trapezoidal	-0.09179	-0.01427	0.01707	0.02793	15.75267	-11.109

Table 4.6: Averaged terminal end-effector state at  $t_f = 0.43$  for a payload of 6000g

Table 4.7 shows the maximum velocities and accelerations occurring in the task space. As before, the highest accelerations are associated with the  $\frac{1}{8}$  trapezoidal-Lamé trajectory.

Motion Profiles	Velocity [m/s]			Acceleration [m/s <sup>2</sup> ]		
	Lamé	Clothoid	Polar	Lamé	Clothoid	Polar
7 <sup>th</sup> order polynomial	1.9581	1.9571	1.9504	48.476	47.094	50.31
Bang-bang	1.7962	1.7943	1.787	32.551	31.308	31.939
$\frac{1}{4}$ Trapezoidal	1.2185	1.2154	1.2256	47.465	46.194	45.352
$\frac{1}{8}$ Trapezoidal	1.0761	1.074	1.076	82.574	82.159	74.896

Table 4.7: Maximum task space velocity and acceleration for a payload of 6kg and a cycle time of  $t_f = 0.43$

## Joint Torques

The maximum torques required for each signal are summarized in table 4.8.

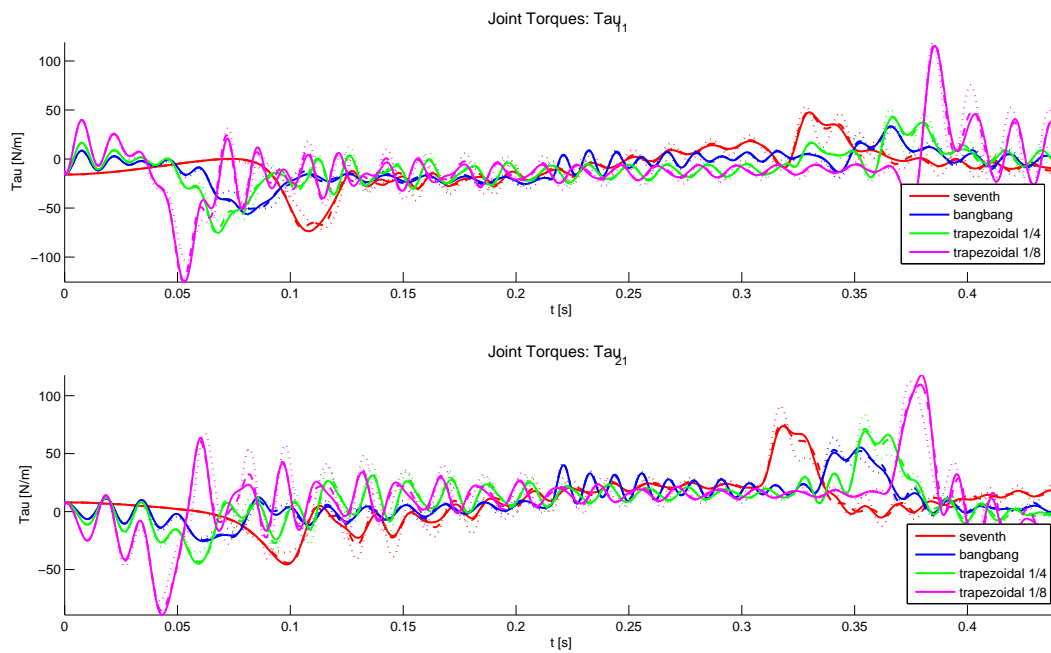


Figure 4.11: Joint torques for a 6000g payload. Line styles: - Lamé, - - Clothoid, ... Polar

## Vibrations

The elastic coordinates  $\mathbf{q}_e$  are also obtained through the solution of the inverse dynamic model. The elastic coordinates in bending and in tension-compression are presented in figures 4.12 and 4.13 respectively.

Figure 4.14 shows the power spectral density of the elastic coordinates  $\mathbf{q}_e$ , the frequencies identified in section 4.2.1 are identifiable as peaks in the figure. Again, the first two modes of vibration are dominant as they are excited by the input trajectories.

The results of this simulation set is summarized in table 4.8. From the table, it can be seen that high input accelerations, and thus high torques, correspond to the highest deflections (i.e.  $\frac{1}{4}$  trapezoidal profile), while the opposite is true for low input accelerations (i.e. bang-bang).

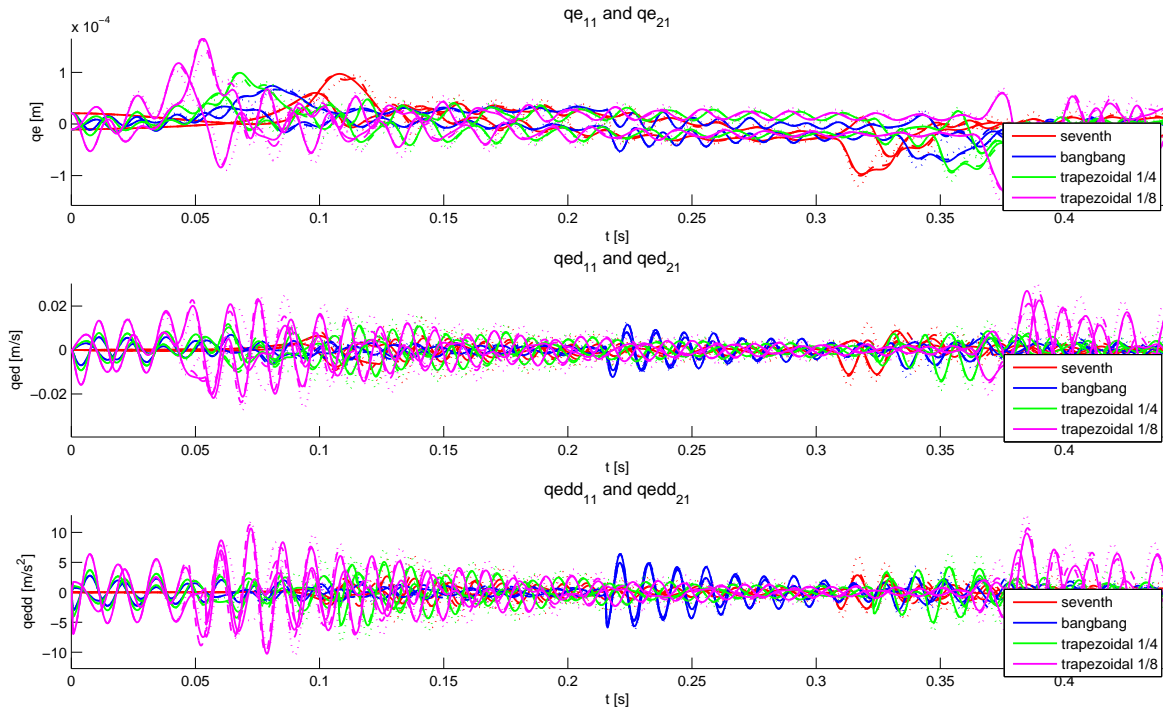


Figure 4.12: Elastic Coordinates in Bending for with a 6kg payload. Line styles: - Lamé, - - Clothoid, ... Polar

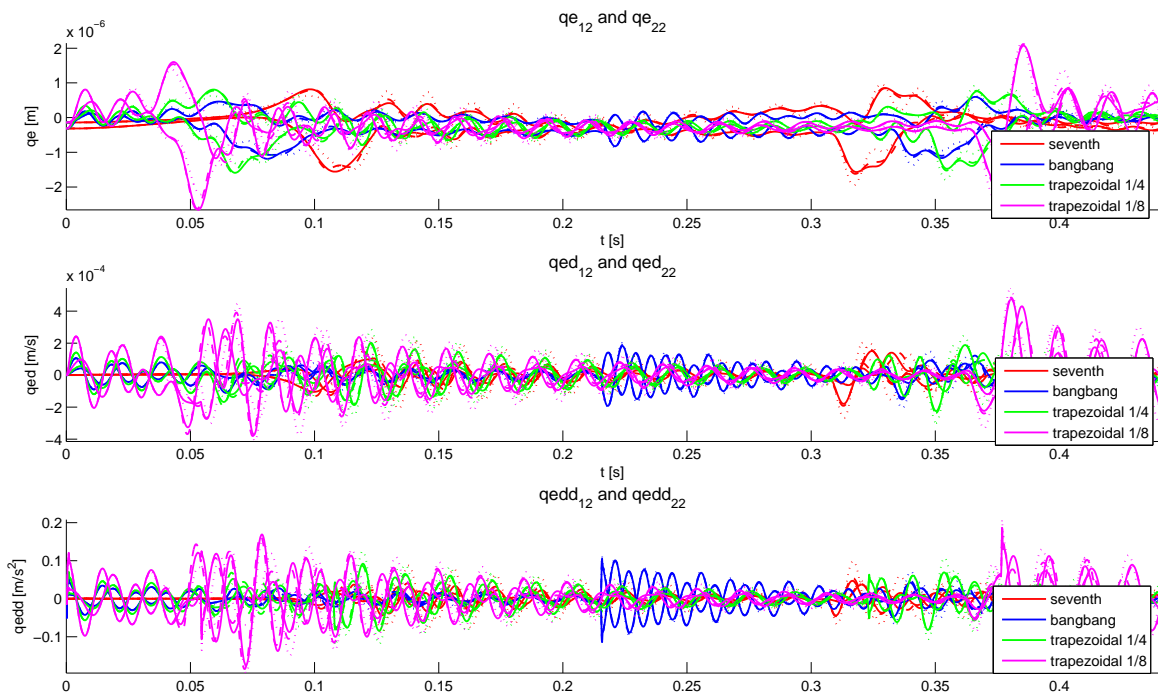


Figure 4.13: Elastic Coordinates in Tension-Compression for a 6000g payload. Line styles: - Lamé, - - Clothoid, ... Polar

From the figures it can be seen that vibratory content of a given signal depends on the smoothness of the trajectory, with less oscillations attributable to the 7<sup>th</sup> degree polynomial.

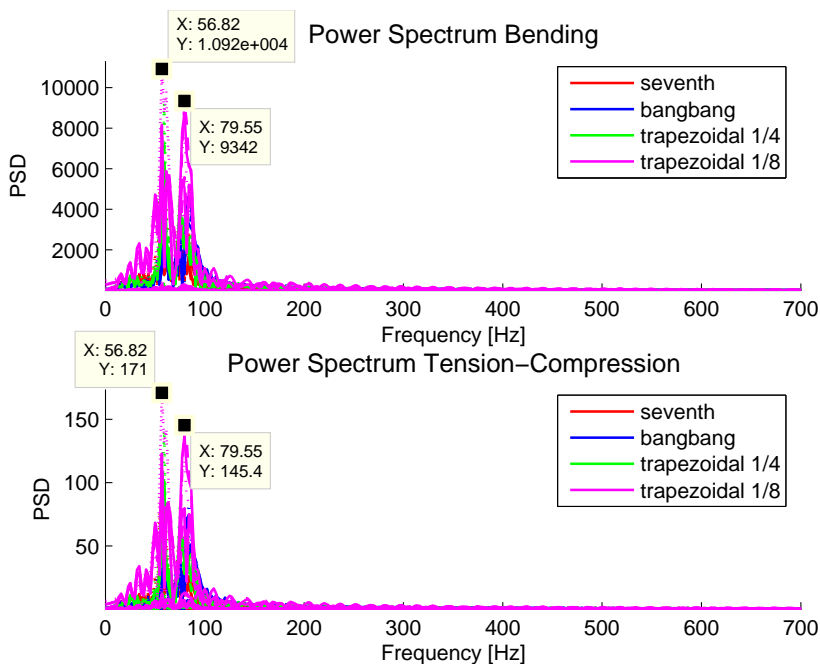


Figure 4.14: Spectral Distribution for a 6kg payload. Line styles: - Lamé, - - Clothoid, ... Polar

	Lamé	Clothoid	Polar
Motion Profiles	Torque [ $Nm$ ]		
7 <sup>th</sup> order polynomial	73.634	70.046	71.298
Bang-bang	56.084	50.848	50.734
$\frac{1}{4}$ Trapezoidal	75.208	74.605	62.496
$\frac{1}{8}$ Trapezoidal	125.45	124.45	119.16
Motion Profiles	RMS Acceleration Error [ $m/s^2$ ]		
7 <sup>th</sup> order polynomial	2.7168	3.3724	6.641
Bang-bang	4.5245	4.7786	5.4098
$\frac{1}{4}$ Trapezoidal	6.0193	6.3989	8.6868
$\frac{1}{8}$ Trapezoidal	10.572	10.731	13.865
Motion Profiles	Max Deflection [ $mm$ ]		
7 <sup>th</sup> order polynomial	0.09700	0.09226	0.09392
Bang-bang	0.07387	0.06696	0.06681
$\frac{1}{4}$ Trapezoidal	0.09911	0.09832	0.08233
$\frac{1}{8}$ Trapezoidal	0.16540	0.16408	0.13813

Table 4.8: Task space velocity and acceleration comparison of generated trajectories

The smoother the trajectory and geometric path, the less oscillatory the signal, this is revealed through the RMS error values. It can be seen that the 7<sup>th</sup> order polynomial-Lamé curve provides the best results to this regard.

## Errors in the Task Space

The norm of the error in the task space for a payload of 6kg and a cycle time of  $t_f = 0.43s$  is shown in figure 4.15. The results are slightly different to those presented in figure 4.8. Although the bang-bang profile yields a lower residual error norm in position than the 7<sup>th</sup> order polynomial, it can be seen that the residual errors in velocity and acceleration are attenuated to greater extent by the 7<sup>th</sup> order polynomial.

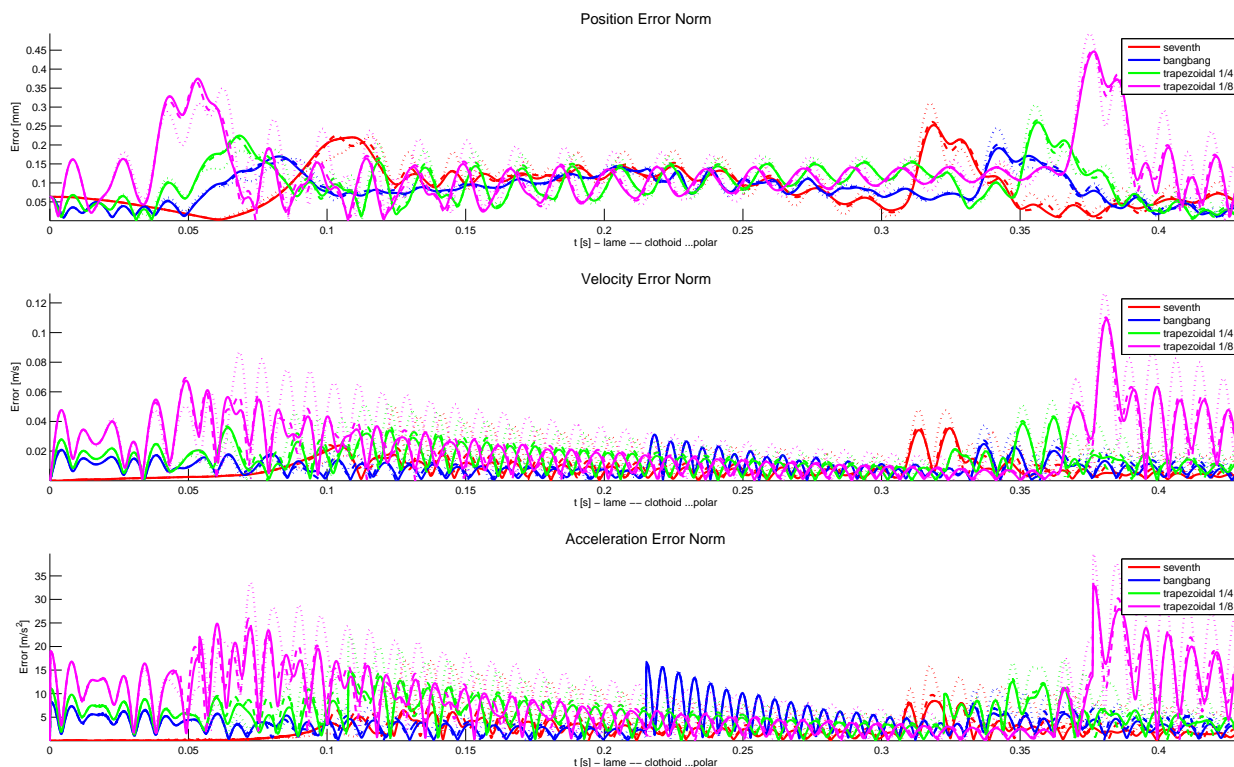


Figure 4.15: Error norm in the task space with a 6kg payload. Line styles: - Lamé, - - Clothoid, ... Polar

	Lamé	Clothoid	Polar
Motion Profiles	Position [mm]		
7 <sup>th</sup> order polynomial	0.9355	0.0009	0.3109
Bang-bang	4.8557	0.0007	0.5573
$\frac{1}{4}$ Trapezoidal	5.5411	0.0017	0.9366
$\frac{1}{8}$ Trapezoidal	8.7118	0.0049	0.2872
Motion Profiles	Velocity [m/s]		
7 <sup>th</sup> order polynomial	0.0009	0.0053	0.4973
Bang-bang	0.0049	0.0050	1.0716
$\frac{1}{4}$ Trapezoidal	0.0055	0.0055	0.2611
$\frac{1}{8}$ Trapezoidal	0.0087	0.0062	0.8352
Motion Profiles	Acceleration [ $m/s^2$ ]		
7 <sup>th</sup> order polynomial	0.5573	0.0045	1.3193
Bang-bang	0.4973	0.0087	3.8472
$\frac{1}{4}$ Trapezoidal	0.8352	0.0056	1.8212
$\frac{1}{8}$ Trapezoidal	1.8212	0.0083	3.0404

Table 4.9: Residual error norms at end effector end points for a payload of 6kg

### 4.3 Simulation Set 3: 6.0kg $t_f = 0.215s$

This section briefly looks the effect of halving the cycle time of the test studied in section 4.2. This study is conducted to observe the effect of the deformations in the task space to a greater extent.

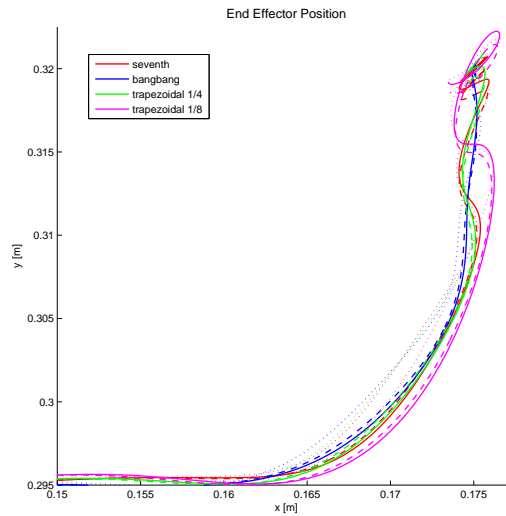


Figure 4.16: Task space position for a payload of 6kg and  $t_f = 0.215ms$  Line styles: - Lamé, - - Clothoid, ... Polar

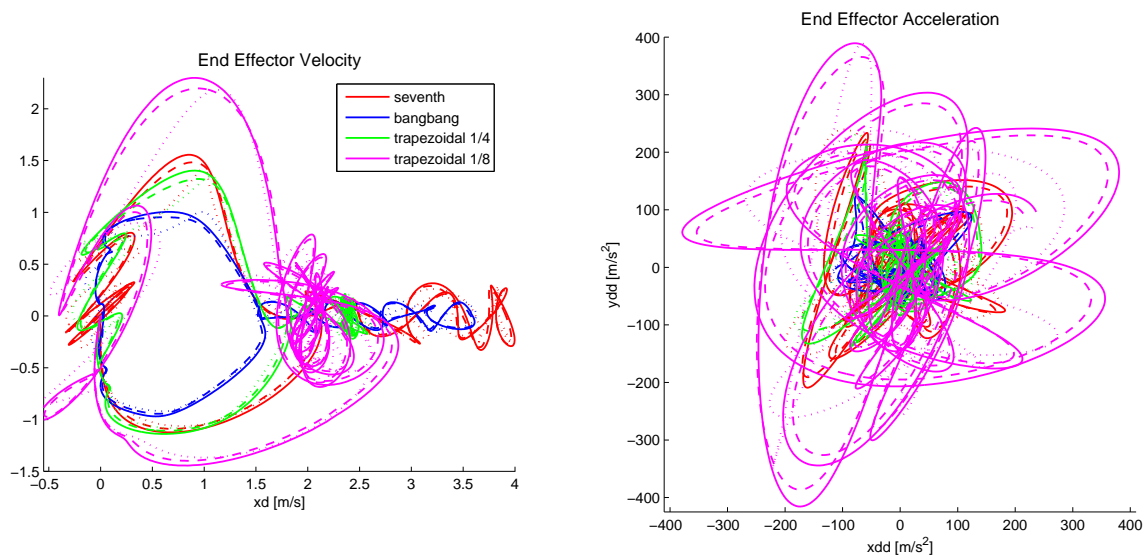


Figure 4.17: Task space velocity and acceleration for a payload of 6kg and  $t_f = 0.215s$  Line styles: - Lamé, - - Clothoid, ... Polar

In figure 4.16, it can be seen that the deformations do indeed become visible. The resultant velocities and accelerations are extremely high due to the short cycle time and the dominant inertial effects (figure 4.17).



	Lamé	Clothoid	Polar
Motion Profiles	Torque [Nm]		
7 <sup>th</sup> order polynomial	422.36	409.52	420.02
Bang-bang	200.69	198.11	210.11
$\frac{1}{4}$ Trapezoidal	366.02	350.89	368.43
$\frac{1}{8}$ Trapezoidal	630.69	613.85	627.44
Motion Profiles	RMS Acceleration Error [ $m/s^2$ ]		
7 <sup>th</sup> order polynomial	84.852	78.239	79.583
Bang-bang	36.81	36.294	44.308
$\frac{1}{4}$ Trapezoidal	58.564	53.32	63.981
$\frac{1}{8}$ Trapezoidal	172.95	161.75	148.51
Motion Profiles	Max Deflection [mm]		
7 <sup>th</sup> order polynomial	0.44778	0.41406	0.41328
Bang-bang	0.26455	0.26118	0.21627
$\frac{1}{4}$ Trapezoidal	0.35171	0.33231	0.32705
$\frac{1}{8}$ Trapezoidal	0.78559	0.73566	0.6854

Table 4.10: Comparison of results for a cycle time of  $t_f = 0.215s$ 

Table 4.10 compares the various trajectories. As before, geometric paths sampled with the  $\frac{1}{8}$  trapezoidal show require the highest torques and are associated with the greatest RMS errors and deflections. The bang-bang profile requires the lowest acceleration for any given path, and shows better performance. Interestingly, it would seem that at these extreme conditions, the smoothness of the 7<sup>th</sup> degree polynomial-Lamé curve trajectory is not an adequate guarantee for a low RMS error.

	Lamé	Clothoid	Polar
Motion Profiles	Position [mm]		
7 <sup>th</sup> order polynomial	1.1	1.6	1
Bang-bang	0.1	0.6	0.4
$\frac{1}{4}$ Trapezoidal	0.6	1.1	0.6
$\frac{1}{8}$ Trapezoidal	2.5	1.7	2.2
Motion Profiles	Velocity [m/s]		
7 <sup>th</sup> order polynomial	0.057	0.0599	0.0339
Bang-bang	0.0894	0.0883	0.1016
$\frac{1}{4}$ Trapezoidal	0.1435	0.1365	0.1104
$\frac{1}{8}$ Trapezoidal	0.4034	0.3958	0.3637
Motion Profiles	Acceleration [ $m/s^2$ ]		
7 <sup>th</sup> order polynomial	148.05	136.74	130.50
Bang-bang	8.635	10.771	42.82
$\frac{1}{4}$ Trapezoidal	107.91	94.561	110.36
$\frac{1}{8}$ Trapezoidal	292.71	268.61	255.20

Table 4.11: Residual error norms at end effector end points for a payload of 6kg

The error norms shown for the extremely high speed simulation in table 4.11 correspond to the findings in table 4.10. At the end of the cycle, the error norm is the best for the bang-bang profile as it invokes the lowest acceleration.

## 4.4 Simulation Set 4: Extended Curve Lengths

This section looks at the effect of varying the blending lengths of the clothoid pairs and the Lamé curve. The blending curves with  $d = e = 25\text{mm}$  are compared with a Lamé curve with  $e = 125\text{mm}$  and a clothoid pair with  $e = 44\text{mm}$  (referred to as *extended* curves). The curves and the associated velocity and frequency behaviour in the task space are shown in figure 4.18.

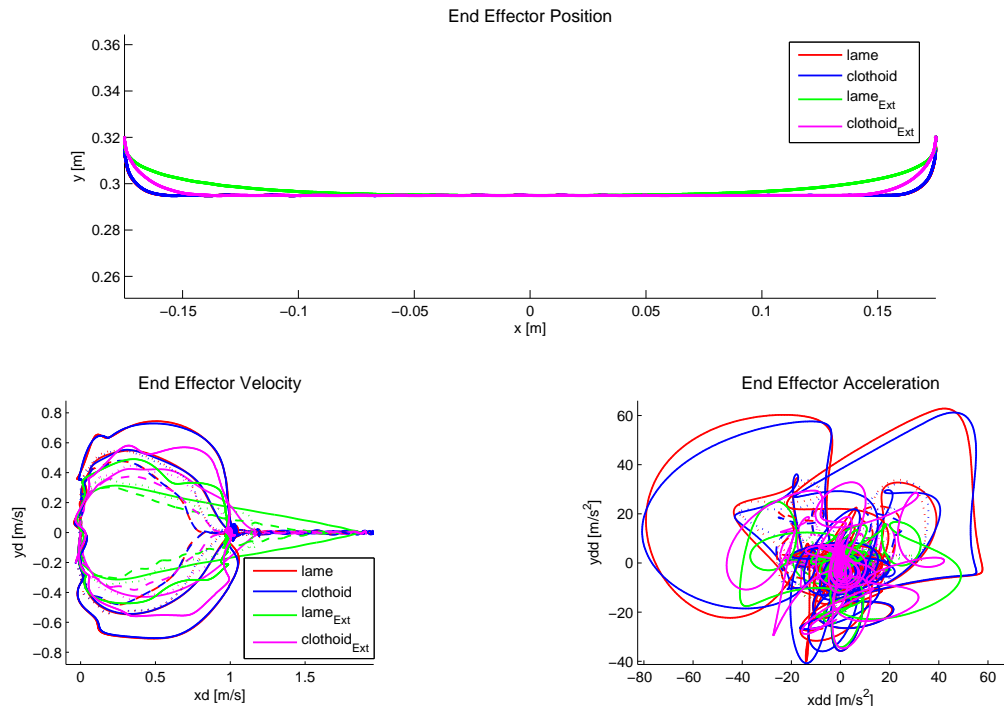


Figure 4.18: Varying blending lengths for a 6000g payload. Line styles: - Lamé, - - Clothoid, ... Polar

	Lamé	Clothoid	Lamé Ext	Clothoid Ext
Motion Profiles	Total Path Length [mm]			
N/A	<b>0.3843</b>	0.3840	<b>0.3687</b>	0.3751
Motion Profiles	Torque [Nm]			
7 <sup>th</sup> order polynomial	73.634	70.046	<b>29.145</b>	46.408
Bang-bang	56.084	50.848	34.596	36.402
$\frac{1}{4}$ Trapezoidal	75.208	74.605	39.28	44.816
$\frac{1}{8}$ Trapezoidal	<b>125.45</b>	124.45	70.937	70.39
Motion Profiles	RMS Acceleration Error [m/s <sup>2</sup> ]			
7 <sup>th</sup> order polynomial	2.7168	3.3724	<b>0.53046</b>	2.3421
Bang-bang	4.5245	4.7786	3.9246	4.0618
$\frac{1}{4}$ Trapezoidal	6.0193	6.3989	4.859	5.2756
$\frac{1}{8}$ Trapezoidal	10.572	<b>10.731</b>	6.5765	8.4488
Motion Profiles	Max Deflection [mm]			
7 <sup>th</sup> order polynomial	0.09700	0.09226	<b>0.03833</b>	0.06106
Bang-bang	0.07387	0.06696	0.04556	0.04791
$\frac{1}{4}$ Trapezoidal	0.09911	0.09832	0.05173	0.05902
$\frac{1}{8}$ Trapezoidal	<b>0.16540</b>	0.16408	0.10245	0.09252

Table 4.12: Comparison of short and extended cycle lengths

From table 4.12, it can be observed that the shortest trajectory, the extended Lamé curve, shows the best performance on all counts. The extended Lamé curve drastically reduces the required torque, the acceleration error and the maximum deflection observed along the path. Table 4.13 shows the error norms in position, velocity and acceleration. In general it can be observed that shorter path lengths yield better results, with the 7<sup>th</sup> order polynomial providing the best results in velocity and in acceleration.

	Lamé	Clothoid	Lamé Ext	Clothoid Ext
Motion Profiles	Total Path Length [mm]			
N/A	<b>0.3843</b>	0.3840	<b>0.3687</b>	0.3751
Motion Profiles	Position [mm]			
7 <sup>th</sup> order polynomial	0.0524	0.0503	0.0606	0.0905
Bang-bang	0.0219	0.0293	<b>0.0125</b>	0.0461
$\frac{1}{4}$ Trapezoidal	0.0158	0.0221	0.0056	0.0320
$\frac{1}{8}$ Trapezoidal	<b>0.0968</b>	0.0919	0.0441	0.0659
Motion Profiles	Velocity [m/s]			
7 <sup>th</sup> order polynomial	0.0014	0.0044	<b>0.0005</b>	0.0058
Bang-bang	0.0085	0.0102	0.0007	0.0039
$\frac{1}{4}$ Trapezoidal	0.0122	0.0130	0.0134	0.0138
$\frac{1}{8}$ Trapezoidal	0.0162	0.0253	0.0081	<b>0.0283</b>
Motion Profiles	Acceleration [m/s <sup>2</sup> ]			
7 <sup>th</sup> order polynomial	1.7121	2.0211	0.3816	<b>0.2521</b>
Bang-bang	1.6179	2.9177	0.2230	0.8533
$\frac{1}{4}$ Trapezoidal	1.6563	2.2635	1.0501	1.2532
$\frac{1}{8}$ Trapezoidal	<b>18.1496</b>	17.4328	8.9629	12.2502

Table 4.13: Comparison of error norms on short and extended cycle lengths

This concludes the chapter on simulation. A summary is made and conclusions are drawn in the final chapter. Future work and perspectives are highlighted.

# Chapter 5

## Conclusion

This master thesis investigated the use of an elastodynamic model to simulate the behaviour of a elastic five bar mechanism performing pick and place tasks. The work covered in this report can be summarized under the following categories:

- Geometric and Kinematic Modeling
- Elastodynamic Modeling
- Trajectory Generation
- Simulation

### Geometric and Kinematic Modeling

A rigid and elastic model of the five bar mechanism was developed. The model is simple as the number of DOF of the task and of each leg are the same. This section developed the kinematic relations relating the dependent coordinates  $\mathbf{q}_d$  to the independent coordinates  $\mathbf{q}_i$ . The elastic model introduces the elastic coordinates  $\mathbf{q}_e$  and increases the complexity. The deformations are incorporated by computing the effective link lengths based on the elastic coordinates.

### Elastodynamic Modeling

The section on elastodynamic modeling gave a detailed development of the inertial and stiffness matrices. The method of assumed modes was chosen, and its accuracy was checked against a CASTEM finite element model. The verification process showed an accuracy of 4% on the natural frequencies and 2.5% on the static deformations. The distribution of natural frequencies in the robot workspace was obtained and evaluated for various payloads.

The dynamic model was derived according to the Lagrangian formulation. Jacobian matrices were used to obtain the closed loop dynamics of the system. The Coriolis and centrifugal efforts were obtained through differentiation of the inertia matrices. The inverse and direct dynamic models were developed in such a way that they could be used for simulation purposes.

## Trajectory Generation

The geometric paths were developed using Lamé curves, clothoid pairs and polar polynomials. A 7<sup>th</sup> degree polynomial, bang-bang profile and two trapezoidal profiles were chosen as motion profiles and used to sample the geometric paths. The motion profiles were constrained according to a certain cycle time  $t_f$ , giving insight into the type of motors required. A total of 12 trajectories could be generated and the following was studied:

- Maximum velocities and accelerations
- Spectral content of joint trajectories
- The effect of varying the cycle time  $t_f$
- The effect of varying the blending lengths of the geometric paths

As expected, it was shown that a bang-bang motion profile requires the lowest acceleration for a given  $t_f$ , whereas a  $\frac{1}{8}$  trapezoidal profile requires the highest. It was found that the spectral content of the joint trajectories would be concentrated on the first two natural frequencies of the five bar mechanism. Decreasing the cycle time  $t_f$  or blending lengths  $d$  and  $e$  showed an inflation in the spectral content of these signals.

## Simulation

The technical specifications given by Adept Technologies Inc. [13] were used to define appropriate simulation tests. Simulations were conducted for the following:

Payload	Cycle Time	Blending Lengths
100g	$t_f = 0.3s$	$d = e = 25mm$
6kg	$t_f = 0.43s$	$d = e = 25mm$
6kg	$t_f = 0.215s$	$d = e = 25mm$
6kg	$t_f = 0.430s$	$d_{Lame} = d_{clothoid} = 25mm, e_{Lame} = 175mm, e_{clothoid} = 44mm$

The simulations were discussed and compared with respect to:

- Terminal state error in position, velocity and acceleration
- Maximum torque, deflection, velocity and acceleration
- RMS error in acceleration

The simulation results showed the following:

1. The pick and place trajectories only excite the first and second natural frequencies of the five bar mechanism
2. The maximum deflection along the path is directly related to the maximum torque required to complete the given trajectory in a given  $t_f$
3. The shorter the path length, the lower the required acceleration and as a result the lower the required torque
4. The terminal state accuracy can be attributed to the smoothness of the trajectory, with 7<sup>th</sup> degree polynomial-Lamé trajectories showing the best results

**Future Work and Perspectives** A substantial platform has been developed on which the following future work is envisioned:

1. **Modeling**
  - The development of a more comprehensive elastodynamic model for the IRSBot2
2. **Optimality**

- Defining appropriate cost functions and optimization parameters to optimize the designed trajectories

### **3. Controllers**

- Design of conventional feedback controllers on the direct dynamic model of the system
- Implementing input shapers for the reduction of residual vibrations. Note that in the absence of feedback controllers, these input shapers can be tested on the inverse dynamic model of the system

# Bibliography

- [1] I. J. Baiges-Valentin. *Dynamic modeling of parallel manipulators*. PhD thesis, Univerisity of Florida, 1996.
- [2] B. C. Bouzgarrou, P. Ray, and G. Gogu. New approach for dynamic modelling of flexible manipulators. *Part K: Journal of Multi-body Dynamics*, 219(3):285–298, 2005.
- [3] S. Briot, A. Pashkevich, and D. Chablat. Reduced elastodynamic modelling of parallel robots for the computation of their natural frequencies. In *World Congress in Mechanism and Machine Science*, 13, June 2011.
- [4] T. R. Chandrupatla and A. D. Belegundu. *Introduction to Finite Elements in Engineering*. Prentice Hall, third edition edition, 2002.
- [5] J. García de Jalón and E. Bayo. *Dynamic Simulation of Multibody Systems - The Real Time Challenge -*. Springer Verlag, 2002.
- [6] S. Kumar Dwivedy and P. Eberhard. Dynamic analysis of flexible manipulators, a literature review. *Mechanism and Machine Theory*, 41(7):749 – 777, 2006.
- [7] Elau. Elau pac2. <http://backoffice.elau.de>, 2007. Datasheet accessed February 2011.
- [8] J.-F. Gauthier, J. Angeles, and S. Nokleby. Optimization of a test trajectory for scara systems. *Advances in Robot Kinemaics: Analysis and Design*, pages 225–234, 2008.
- [9] Germain, S. C., Briot S. Caro, and Wenger P. Irsbot-2 : Un nouveau robot parallèle à deux degrés de liberté pour des applications de manipulation rapide. In *Actes du 20ème Congrès Français de Mécanique, 2011, Besançon, France.*, September 2011.
- [10] C. Germain. Analyse et conception d’un nouveau manipulateur parallèle á deux degrés de liberté pour des applications de pick-and-place. Master’s thesis, Ecole Centrale de Nantes, 2010. Institut de Recherche en Communication et Cybernétique de Nantes.
- [11] C. Germain, S. Briot, V. Glazunov, S. Caro, and P. Wenger. Irsbot-2: A novel two-dof parallel robot for high-speed operations. In *Proceedings of the ASME 2011 International Design Engineering Technical Conferences and Computers and Information in Engineering Conference, Washington DC, USA.*, August 2011.
- [12] P. S. Heyns. *Mechanical Vibration Measurment and Analysis*. University of Pretoria, 2009.
- [13] Adept Technology Inc. [www.adept.com](http://www.adept.com). Webpage accessed February 2011.
- [14] Y. Kanayama and N. Miyake. Trajectory generation for mobile robots. In *International Symposium on Robotics Research*, pages 333 – 340, 1985.
- [15] W. Khalil. *Advanced Modeling of Robots*. Ecole Centrale de Nantes, 2010.
- [16] W. Khalil. *Identification and Control of Robots. Part II: Control*. Ecole Centrale de Nantes, 2010.
- [17] Z. Mohammed and M. O. Tokhi. Command shaping techniques for vibration control of a flexible robot manipulator. *Mechatronics*, 14:69–90, 2004.
- [18] Robotics Online. Pick-and-place applications for robots. [www.robotics.org](http://www.robotics.org), August 2010. Article accessed February 2011.
- [19] Healthcare Packaging. Robotic rx for pharmaceutical packaging. [www.healthcarepackaging.com](http://www.healthcarepackaging.com), March 2008. Article accessed February 2011.

- [20] A. Pashkevich, D. Chablat, and P. Wenger. Stiffness analysis of overconstrained parallel manipulators. *Mechanism and Machine Theory*, 44(5):966 – 982, 2009.
- [21] G. Piras, W. L. Cleghorn, and J. K. Mills. Dynamic finite-element analysis of a planar high-speed, high-precision parallel manipulator with flexible links. *Mechanism and Machine Theory*, 40(7):849 – 862, 2005.
- [22] M. Rognant, E. Courteille, and P. Maurine. A systematic procedure for the elastodynamic modeling and identification of robot manipulators. *IEEE Transactions on Robotics*, 26(6):1085–1093, 2010.
- [23] A. Segovia, M. Rombaut., A. Preciado., and D. Meizel. Comparative study for the different methods of path generation for a mobile robot in a free environment. In *Advanced Robotics, 1991. 'Robots in Unstructured Environments', 91 ICAR., Fifth International Conference on*, pages 1667 – 1670, June 1991.
- [24] A. A. Shabana. Flexible multibody dynamics: Review of past and recent developments. *Multibody System Dynamics*, 1:189–222, 1997. 10.1023/A:1009773505418.
- [25] R. J. Theodore and A. Ghosal. Comparison of the assumed modes and finite element models for flexible multilink manipulators. *The International Journal of Robotics Research*, pages 91–111, 1995.
- [26] Utah State University. <http://mechatronics.ece.usu.edu>. Webpage accessed June 2011.
- [27] D.J. Walton and D.S. Meek. A controlled clothoid spline. *Computers and Graphics*, 29(3):353 – 363, 2005.
- [28] X. Wang and J. K. Mills. Dynamic modeling of a flexible-link planar parallel platform using a substructuring approach. *Mechanism and Machine Theory*, 41(6):671 – 687, 2006.
- [29] E. Wittbrodt, I. Adamiec-Wójcik, and S. Wojciech. *Dynamics of Flexible Multibody Systems*. Springer-Verlag Berlin Heidelberg, 2006.







## Thesis Summary

This master thesis investigated the use of an elastodynamic model to simulate the behaviour of a elastic five bar mechanism performing high speed pick and place tasks. Pick and place tasks are performed at high speed along the adept cycle, which moves an object from one position to another in a workspace.

The master's thesis firstly develops an appropriate elastodynamic model using the method of assumed modes. The elastodynamic modeling involved the development of the inertial and stiffness matrices. Using shape functions in bending for actuated links and shape functions in tension and compression for passive links. The elastic model is accompanied by the necessary geometric and kinematic relationships relating the dependent and independent coordinates in the system. The elastodynamic model is verified against a finite element model and the natural frequencies of the system are identified. The elements of the elastodynamic model are used to develop the closed form direct and inverse geometric relationships according to the Lagrangian formulation.

A further section was devoted to the development of various trajectories. The trajectories define the desired behaviour of the end effector along a pick and place path. The trajectories are constructed by sampling a certain geometric path by a given motion profile. Lamé, clothoid-pair and polar polynomial blends are introduced to smoothen the geometric paths. 7<sup>th</sup> degree polynomials, bang-bang and trapezoidal profiles are used to sample the geometric paths. For a given cycle time, the bang-bang profile has the lowest acceleration. The spectral content of the resultant trajectories in the joint space are identified and discussed. The effect on the spectral content of the signal by varying the cycle times as well as the blending lengths of the geometric curves was studied. It was found that the spectral content of the signals would only coincide with the first and second natural frequencies of the system.

Simulations done in Simulink were used to excite the 5 bar mechanism along the defined trajectories. The simulations were chosen based on cycle times and payloads used in industry. The simulated results reveal the vibrational effect of the deformations arising from the inertial forces. The simulation results are discussed compared. Indeed, spectral analysis of the resultant vibrations showed that only the first and second natural frequencies of the system were excited. It was found that for longer cycle times the residual error norms were improved by the smoothness of the motion profile. At shorter cycle times however, higher accelerations in the smooth profiles deteriorate the performance. The shorter the length of the geometric path, the lower accelerations for a given cycle time are needed.

The thesis work developed a substantial platform from which, in future, elastodynamic models of more complex systems may be constructed. The elastodynamic model can be used to define appropriate cost functions for the optimization of various trajectories. Alternate methods of feedback control and command pre-shaping may also be used to reduce unwanted vibrations.